Mössbauer Diffractometry: Principles, Practice, and an Application to a Study of Chemical Order in $^{57}Fe_3Al$

Thesis by
Jiao Lin

In Partial Fulfillment of the Requirements
for the Degree of
Doctor of Philosophy

California Institute of Technology
Pasadena, California

2004

(Defended May 10)

Acknowledgements

I wish to express my gratitude to my advisor, Brent Fultz. His guidance, encouragement, and advice have made this thesis possible.

I would like to acknowledge my predecessors in this project: Ushma Kriplani and Martin Regehr. They led me to my first understanding of experimental and theoretical issues involved.

I would like to thank my collegues in Keck lab: Ryan Monson, who is now taking over the project, for his helpful discussions; Shu Miao for his help on getting TEM works done; Channing Ahn for his assistance in routine lab issues and helpful discussions in TEM work; Carol Garland for her kind help on TEM works; Alan Yue, Alex Papandrew, JaeDong Lee, Jason Graetz, Nathan Good, Olivier Delaire, Tabitha Swan-Wood, and Tim Kelley, for sharing their thoughts and fun with me. I am also grateful to other folks in Keck, for their kind help: Pam Albertson, Robin Hanan, Elizabeth Welsh, etc.

I would like to thank Fiona Harrison for allowing us to use their CZT/CT detector technology, and to acknowledge her group members including Hubert Chen, Jill Burnham, Rick Cook, ..., for their kind instructions and discussions about CZT/CT detectors.

I am indebted to some students of Materials Science, 1999: Jian Wu, Lan Yang, Qingsong Zhang and Tao Feng. They filled my stay in Caltech with fun and collision of thoughts.

I am very grateful to my parents, Manqing Hu and Yingji Lin, and my younger brother, Rong Lin. Their unconditional support are always there.

My warmest thanks to my wife, Yayun Liu. Without her understanding and support, this endeavor would not be possible.

Mössbauer Diffractometry: Principles, Practice, and an Application to a Study of Chemical Order in ^{57}Fe$_3$Al

by

Jiao Lin

In Partial Fulfillment of the
Requirements for the Degree of
Doctor of Philosophy

Abstract

For the first time, Mössbauer powder diffractometry went beyond the proof-of-principal stage and was used to study unknown periodicities of defect-related chemical environments of Fe atoms in a partially-ordered ^{57}Fe$_3$Al polycrystalline sample.

Mössbauer powder diffractometry is based on two phenomena, the Mössbauer effect and the Bragg diffraction. The Mössbauer effect is sensitive to short-range order whereas diffractometry is sensitive to long-range order. Together, they enable Mössbauer powder diffractometry to provide information on long-range periodicities of target atoms having specific short-range order.

Both experimental and theoretical efforts are necessary for this novel technique to become practial. In this research, hardware and software for Mössbauer powder diffractometry were improved. A kinematical diffraction theory for Mössbauer powder diffractometry incorporating effects of interference between electronic and nuclear resonant scattering was developed. The applicability of the theory was verified by computer calculations that accounted for dynamical diffraction effects. A thorough analysis of polarization effects, including a polycrystalline average of polarization factors, was done systematically using spherical harmonic expansions.

Multiple diffraction patterns were measured at Doppler velocities across all nuclear resonances of ^{57}Fe$_3$Al. On the basis of the theory developed, the superlattice diffractions were analyzed to provide data on the long-range order of Fe atoms having different numbers of Al neighbors. Comparing experimental data to calculations showed that Fe atoms having three Al atoms as first-nearest neighbors (1nn) have partial simple cubic long-range order, similar to that of Fe atoms with four Al 1nn. The simple cubic periodicity of Fe atoms with three Al 1nn was significantly lower than expected for homogeneous antisite disorder, however. Monte–Carlo simulations and transmission electron microscopy suggest that a significant fraction of aperiodic Fe atoms with three Al 1nn are near antiphase domain boundaries.

Contents

List of Figures

List of Tables

Chapter 1

Introduction

1.1 An Intuitive Description of Mössbauer Powder Diffractometry

Mössbauer powder diffraction is a novel technique combining the capability of Mössbauer spectrometry to distinguish the chemical environments (short-range order) around specific target atoms[1] and the capability of diffractometry to measure the long-range order. It enables studies of long-range order of atoms with specific short-range order.

For example, look at the structure of an Fe_3Al sample with perfect $D0_3$ structure in Fig. 1.1. For iron atoms, two chemical environments exist. Fe atoms on the γ-sublattice (red) have no Al first nearest neighbors (1nn). Fe atoms with 4 Al and 4 Fe 1nn (green) occupy two face centered cubic (fcc) sublattices, α and β, and form a simple cubic (sc) long-range order. The δ-sublattice is occupied by Al atoms. As is well known, Mössbauer resonance energies are very sensitive to the chemical environments of the target atoms. Because the resonance energy of a ^{57}Fe nuclei depends on its chemical environment, the absorption and scattering cross section of this iron atom are also strongly dependent on its chemical environments. We can tune the energy of incident γ-ray photons to a specific chemical environment and then the atoms with this chemical environment will contribute strongly to the diffraction pattern. For a more visual presentation, please take a look at Fig. 1.2. Here, Al atoms are small, blue balls while Fe atoms are red, big balls. The size of an atom is used to represent its scattering cross section; the bigger the atom, the stronger its scattering. Three different resonance conditions are presented in this figure. In Fig. 1.2a, the incident γ-ray is not on resonance for any atom, so the scattering cross section of Fe atoms are all the same, and 3 times larger than

---

[1] For this dissertation, Fe atoms.

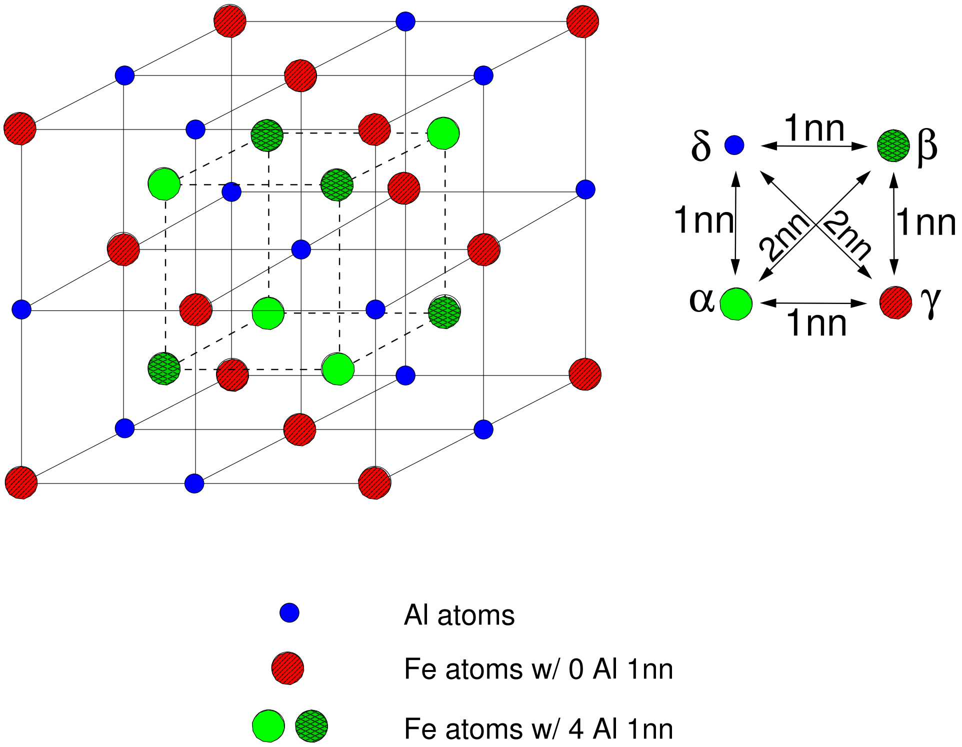

Figure 1.1: Fe_3Al with the perfect $D0_3$ structure. This structure is a superposition of 4 fcc sublattices, α, β, γ and δ. Only the δ-sublattice is occupied by Al atoms while other three sublattices are occupied by Fe atoms.

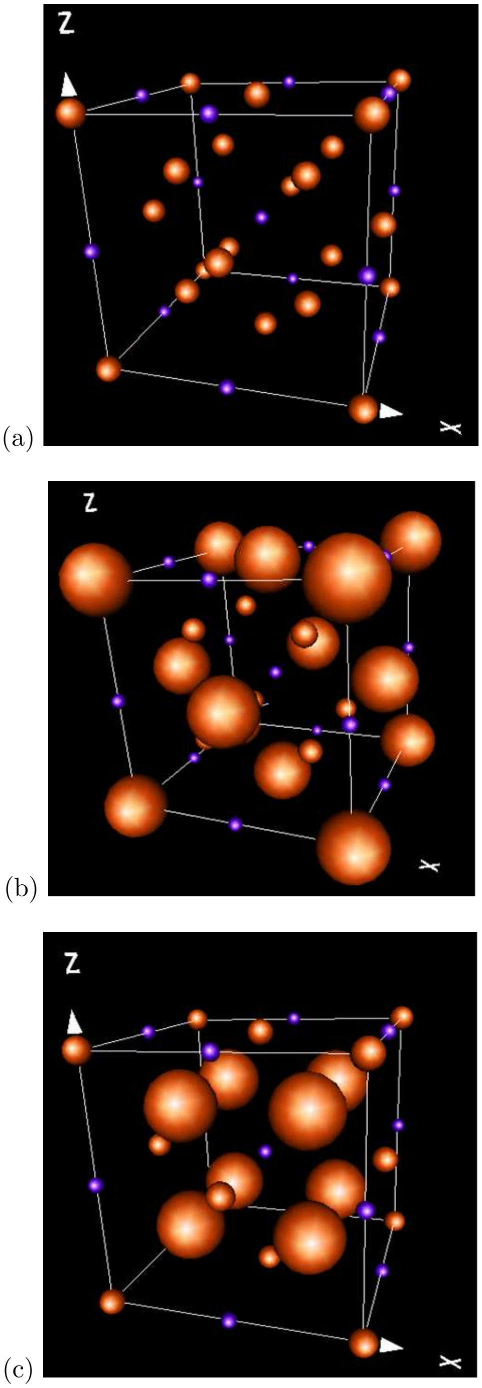

Figure 1.2: Fe_3Al with the $D0_3$ structure in various resonance conditions: (a) off-resonance, (b) Fe atoms with (0) Al 1nn on resonance, (c) Fe atoms with (4) Al 1nn on resonance. The size of the balls indicates their cross section for incident photons.

that of Al atoms[2]. This is in essence an X-ray diffraction experiment. In Fig. 1.2b, we tune the γ-ray to be on resonance for iron atoms with zero Al 1nn, and they are now very strong scatterers. In Fig. 1.2c, iron atoms with 4 Al and 4 Fe 1nn are on resonance and will make the largest contribution to scattered waves. Notice the approximate fcc structure in Fig. 1.2b and the sc structure in Fig. 1.2c, which give different diffraction patterns. As a result, diffraction patterns for these three cases should show differences in intensities of superlattice diffraction orders. It is now very clear that with Mössbauer diffraction, we can "see" the structure of specific chemical environments by tuning the γ-ray energy.

The idea here sounds simple and powerful, but its realization requires both experimental and theoretical developments. In the next Section, a review of these developments is presented.

1.2 Mössbauer Powder Diffractometry

In X-ray diffraction, photons are scattered coherently by electrons. The scattered wave amplitude, ψ, as a function of scattering vector, $\mathbf{k}$, on a detector far from the scattering center, is proportional to the Fourier transform of scattering amplitude as a function of $\mathbf{r}$ inside the crystal. Long-range order (LRO) in the crystal will show itself as peaks in the diffraction pattern. The diffracted intensities can reveal much information about the structure of the crystal under investigation. Mössbauer diffraction involves coherent elastic scattering of γ-ray photons by not only electrons but more importantly by nuclei in a sample containing at least one atomic species capable of nuclear resonant absorption and re-emission. By tuning the energy of the incident γ-ray, a specific chemical environment of the Mössbauer nucleus can be emphasized, as shown in the previous Section, and its LRO can be measured. Despite its promise as another powerful diffraction technique besides X-ray diffractometry, transmission electron microscopy (TEM) and neutron diffractometry[3], Mössbauer diffraction based on kinematical theory [43, 7] was possible only very recently [61, 57, 35, 37], due to low count rates.

The coherence of Mössbauer scattering was first shown in the early 1960s by Black and Moon[10], and the first Mössbauer diffraction measurements were performed a few years later[9]. However, until very recently, most research on Mössbauer diffraction utilized perfect single crystals [9, 53, 62, 52]. Even today there is active development of Mössbauer dynamical diffraction using synchrotron radiation (SR) sources (see, e.g., Ref. [47, 26, 59, 45]), which take advantage of the brightness of SR for single crystal work. Unfortunately, multiple scattering is so strong for perfect single crystals that

---

[2] In this case, the only contribution comes from the electronic scattering, of which the atom scattering factor is approximately proportional to the number of electrons in the atom. Thus, $\frac{\sigma_{\mathrm{Fe}}}{\sigma_{\mathrm{Al}}} \sim (\frac{26}{13})^2 = 4$

[3] A comparison between these diffraction techniques is presented in Section 3.3.

dynamical diffraction theory [33, 28, 29, 32, 30] must be used to interpret the data. This makes it impractical to invert single-crystal diffraction patterns to obtain quantitative information on atomic structure.

Kinematical diffraction theory could be applicable for polycrystalline samples with small-enough crystallites[4]. Polycrystalline diffraction experiments are more difficult than for oriented single crystals, however, due to the low flux. The past decade has seen improvements in both instrumentation and theory for Mössbauer powder diffractometry in the kinematical limit [61, 58, 57, 21, 35, 39, 38, 37]. Tegze and Faigel have built a Mössbauer powder diffractometer capable of gathering diffraction patterns from a cylindrical sample and they have obtained energy spectra from an enriched ferromagnetic ^{57}Fe sample. The following developments were mostly made in the Fultz group at Caltech.

Prior Experiment Stephens and Fultz [57] built the first powder diffractometer using an INEL detector system. With this “first-generation” Mössbauer powder diffractometer, they performed a “proof-of-principle” experiment, showing for the first time that in a ^{57}Fe$_3$Al sample the diffraction patterns of ^{57}Fe atoms with 0 and 4 Al 1nn could be obtained by tuning the energy of the γ-ray photons to resonance energies of these two chemical environments, respectively. Kriplani, Regehr and Fultz adopted a Xe-filled, Bruker X-1000 detector in the “second-generation” Mössbauer powder diffractometer. This area detector has better efficiency to 14.4 keV photons and better capability for detecting photons off the scattering-plane, so the measured diffraction intensities were stronger. Furthermore, this detector is relatively insensitive to high-energy photons, which contribute to background noise. This diffractometer was highly-automated in that the goniometer, the drive system, and the detector system could be controlled by one computer program written in Visual Basic®. With the improved flux of this “second-generation” diffractometer, they were able to measure coherent and incoherent diffracted intensities at various resonance energies from a polycrystalline Fe^{57} sample. The effect of a magnetic field applied perpendicular to the scattering plane was also studied.

Prior Theory In his thesis, Stephens presented formalisms of kinematical diffraction theory based on Patterson functions. Diffraction intensities were calculated using a multislice approach. Kriplani[34] adopted Bara’s formalisms[5] to replace the multislice method and developed systematically a model for Mössbauer diffractive and incoherent scattering processes without considering Rayleigh scattering from electrons. Her formalisms also incorporate the polarizing effects of a mag-

---

[4] To give you a rough idea, for a ^{57}Fe sample of crystallite size$\sim$100 nm, the kinematical theory is sufficient, as pointed out in Ref. [56].

netized sample.

Present Developments In this thesis, I

1. improved the diffractometer developed by Kriplani et al. and used it to measure for the first time a full energy spectrum of complete Mössbauer diffraction patterns from a ^{57}Fe$_3$Al sample;
2. gave a kinematical diffraction theory taking into account both electrionic and nuclear resonant scattering, and improved our understanding of the polarization factor and worked out the averaged polarization factors involved in Mössbauer diffraction by using spherical-harmonic expansions;
3. gave a more intuitive account for the Mössbauer scattering processes on the basis of quantum electrodynamics and a simple account for the speed-up effect in dynamical Mössbauer diffraction;
4. developed simulation programs for calculating diffraction intensities based on kinematical diffraction theory;
5. verified the kinematical diffraction model by carry out simulations using dynamical diffraction theory;
6. using these theoretical understanding and calculational tools, carried out fitting procedures to find out optimal experimental parameters (long-range order parameters for various chemical environments) in a partially-ordered ^{57}Fe$_3$Al;
7. interpreted these fitting results on the long-range order parameters of defect chemical environments, using Monte-Carlo simulations of kinetics of disorder-order transformation in Fe$_3$Al, simulations of homogeneous disorder, and transmission electron microscopy (TEM) studies of anti-phase domains;
8. began the development of a "third generation" Mössbauer diffractometer using CdTe detectors.

The next Section provides more details for the motivation for studying Fe$_3$Al.

1.3 Mössbauer Diffraction Study of Fe$_3$Al

As shown in Section 1.1, Fe$_3$Al with the perfect D0$_3$ structure has two distinct chemical environments for Fe atoms, one with 8 Fe atoms as 1nn, another with 4 Fe and 4 Al atoms as 1nn. These two

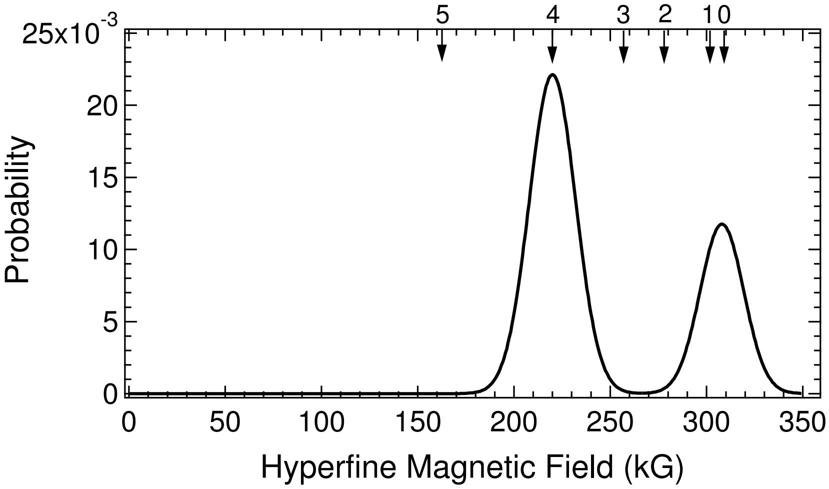

Figure 1.3: Hyperfine magnetic field distribution calculated for a Fe_3Al sample with the perfect $D0_3$ structure.

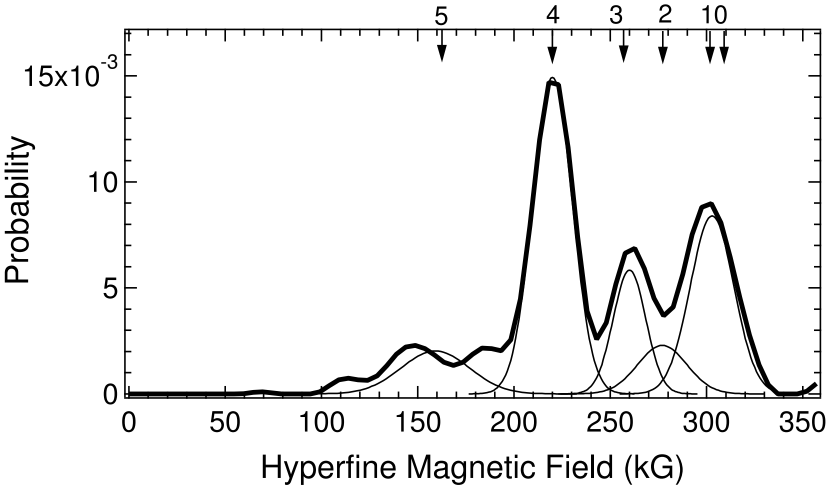

Figure 1.4: Hyperfine magnetic field distribution of a Fe_3Al sample with a partial $D0_3$ order.

chemical environments show themselves as two distinct peaks in the HMF distribution (see Fig. 1.3). This means we can really "turn on and off" the scattering power of Fe atoms of special chemical environments by tuning the Doppler velocity of γ-ray source, as explained in Section 1.1, so Fe_3Al is well-suited for study using Mössbauer diffraction. A first experiment would be to tune the photon energy to be on resonance for Fe atoms of these two chemical environments and measure diffraction patterns that should show different superlattice peaks. This has already been done by Stephens and Fultz [57, 21, 56].

A second experiment could be suggested by Fig. 1.4, the HMF distribution of a real Fe_3Al sample. Notice that this sample shows chemical environments other than the two major chemical environments of the perfect $D0_3$ structure. The additional chemical environments are related to local defects, but their spatial distributions are unknown. By tuning the photon energy to those chemical environments we might be able to obtain information about the spatial periodicities of ^{57}Fe atoms in these defects environments. A study of the evolution of these defects and their spatial distribution along the path of disorder$\longrightarrow$order transition could shed light on the kinetics of this transition in Fe_3Al. As a first step, in this thesis research we have measured the Mössbauer diffraction intensities at Doppler energies through the full Mössbauer spectrum of this $^{57}Fe_3Al$ sample (which was used in the previous "proof-of-principle" experiment done by Stephens and Fultz[56]). These spectra can be used to determine the long-range order of the defect-related Fe atoms. This is a natural development of Mössbauer powder diffractometry: from a proof-of-principle experiment to exploration of unknown properties of materials. In the course of this work, data analysis programs based on kinematical diffraction theories including polarization effects were developed.

Order in Fe_3Al At high temperatures, Fe_3Al has the bcc structure, and develops sc order with the B2 structure at temperatures below 800°C. Below 550°C the equilibrium structure is the $D0_3$ structure, where Al atoms occupy one of four fcc sublattices of the $D0_3$ structure (we denote this Al-rich sublattice as δ as show in Fig. 1.1). After Fe_3Al is quenched rapidly, subsequent annealing at low temperatures shows a number of peculiarities, such as the formation of the B32 structure, which may be a kinetic transient [3, 24, 4], or perhaps driven by magnetic interactions in sub-stoichiometric zones [6]. These ordered structure are shown in Fig. 1.5. In alloys with partial order, it is possible to determine sublattice occupancies by the intensities of superlattice diffractions of x-rays or neutrons, although occupancies become difficult to quantify when the state of order is high and the effects on intensity are small. In many cases including non-equilibrium alloys with small grain sizes, Mössbauer spectrometry is capable of measuring the defect environments in partially ordered Fe_3Al, specifically

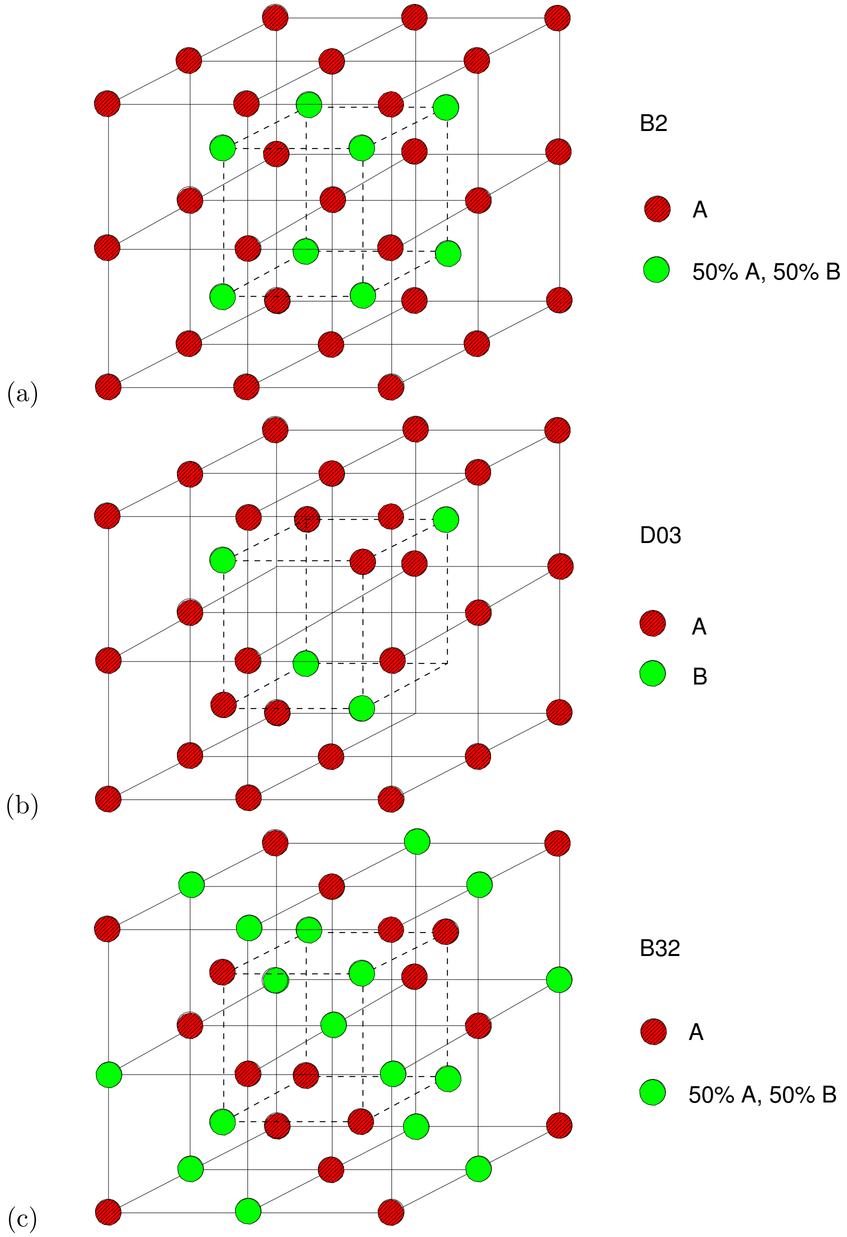

Figure 1.5: B2, D03 and B32 structure

Fe atoms with different numbers of Al first-nearest neighbors[5] [54, 18, 19]. These defect environments may have spatial periodicities of the $D0_3$ structure, although the problem may not be simple owing to expected statistical non-uniformities of composition or if the defect environments interact.

In this thesis research we made the first direct measurements of spatial periodicities of defect environments in a material. Improved instrumentation for the present experiment made it possible to go beyond measurements at resonance peaks of ^{57}Fe atoms in the known chemical environments of the perfect $D0_3$ structure. Mössbauer diffraction patterns were measured over the full Mössbauer energy spectrum of the alloy, making it possible to quantify the unknown spatial periodicity of ^{57}Fe atoms with (3) Al 1nn atoms. It is found that the Fe atoms in this defect environment have some sc periodicity. The data were further analyzed to obtain the occupancies of the four sublattices of the $D0_3$ structure, with no assumptions that would select B2 over B32 chemical order. No evidence for B32 order was found for any chemical environments.

A partial sc order of 0.6 was found for Fe atoms with (3) Al 1nn. It is significantly lower than expected for homogeneous antisite disorder, however. With simulations and TEM study of the alloy structure, it was possible to show that this discrepancy likely originates with a non-random point defect population at antiphase domain boundaries in the crystals.

Chapter 2 presents a fundamental description of the Mössbauer effect and related phenomena. A quantum description of Mössbauer scattering is given in Chapter 3. Chapter 4 presents the kinematical theory of diffraction. Chapter 5 describes our powder diffractometer and general data reduction procedures. The Fe_3Al data are presented and analyzed in Chapter 6. A future generation of Mössbauer diffractometer is described in Chapter 7.

---

[5] Some details could be found in Section 2.4

Chapter 2

Mössbauer Effect

In a conventional Mössbauer transmission spectrometer shown in Fig. 2.1, a γ-ray source is mounted on a Doppler drive, which usually moves back and forth at a speed on the order of 10-100 mm/s. The photons emitted by the source travel through a thin sample containing an appropriate Mössbauer isotope, and the intensity of transmitted photons is measured against the velocity of the source. Nuclear resonance shows up in the spectrum as dips. The extreme sharpness (high Q value) of the nuclear resonance makes this technique useful in many areas of materials research.

An intuitive and naive description of the Mössbauer effect is that, due to the rigidity of a solid, the momentum loss (or change) of a photon scattered by the solid is negligibly small. In the language of quantum mechanics, the energy transfer from the photon to the solid is so small that it may not exceed the energy necessary for creating a phonon, so the possibility of the free recoil of the nucleus is small. Without energy loss to phonons, the extreme sharpness of the resonance is observed. Hyperfine interactions that shift the nuclear resonances are measureable, and these shfits are useful

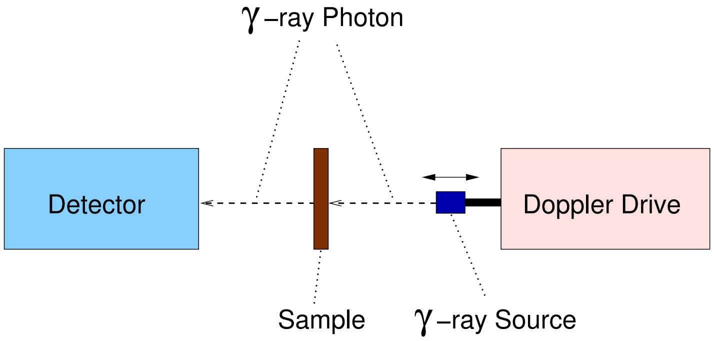

Figure 2.1: A Mössbauer spectrometer.

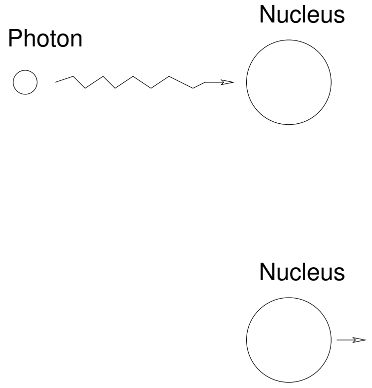

Figure 2.2: Recoil of a free nucleus hit by a photon

to material scientists for identifying the slight variations of chemical environments around Mössbauer atoms. Therefore, we ought to know the conditions that favor this effect and how strong this effect could be. This is the topic of Section 2.1. The energy of the nuclear resonance and various factors that could affect this energy are discussed in Section 2.2. Fe and Fe_3Al are central materials of this thesis research; their Mössbauer spectra are discussed in more detail in Sections 2.3 and 2.4.

2.1 Recoilless Fraction

The recoil of nuclei hit by photons must be suppressed in a Mössbauer transmission experiment. Only if most of the nuclei in the sample do not recoil, will the high Q-value of the nuclear resonance be observed. In this Section the possibility of recoilless absorption of a photon by a Mössbauer nucleus, i.e., the recoilless fraction, is explained.

In Fig. 2.2, a photon with energy E_γ is absorbed by a free nucleus of mass M, which is at rest at $t \leq 0$. The total momentum of the system is E_γ/c. So the velocity of the nucleus at $t > 0$ is E_γ/Mc, and the recoil energy is

$$E_{\mathrm{R,free}} = \frac{E_\gamma^2}{2Mc^2} \tag{2.1}$$

For the case of ^{57}Fe Mössbauer spectroscopy,

$$\begin{aligned} E_\gamma &= 14.41\mathrm{keV} \\ M &= 57 \times 1.66 \times 10^{-27}\mathrm{kg} = 57 \times 931\frac{\mathrm{MeV}}{c^2} \\ E_{\mathrm{R,free}} &= 2\mathrm{meV} \end{aligned}$$

The recoil energy, $E_{\mathrm{R,free}}$, is much larger than the line width of the nuclear resonance of ^{57}Fe, which is $\sim 10^{-9}$eV. Nuclear resonant absorption cannot occur for a free nucleus.

If the nucleus is bound in a solid, in which the movements of atoms are superpositions of quantized vibrational modes, then the recoil energy must be almost as large as the energy of the vibration quanta – phonon, in order to excite a phonon. In the Einstein model of lattice vibrations, there is only one phonon frequency, ω_{E}. Then the condition that the Mössbauer effect can occur is

$$E_{\mathrm{R,free}} \ll \hbar\omega_{\mathrm{E}} = k_{\mathrm{B}}\theta_{\mathrm{E}} \tag{2.2}$$

where k_{B} is the Boltzmann constant, and θ_{E} is the Einstein temperature. In this case the recoil happens to the whole solid, and the recoil energy is $E_{\mathrm{R,free}}/N$, where N is the total number of atoms in the solid. For a solid with 1 mole of atoms, $N \sim 10^{23}$. So the recoil energy is extremely small and nuclear resonant absorption is possible.

The fraction of events in which recoilless absorption or emission occur (recoilless fraction) is

$$f_{\mathrm{ML}} \sim 1 - \frac{E_{\mathrm{R,free}}}{\hbar\omega_{\mathrm{E}}} \sim \exp\left(-\frac{E_{\mathrm{R,free}}}{k_{\mathrm{B}}\theta_{\mathrm{E}}}\right) \tag{2.3}$$

which is also called the Mössbauer-Lamb factor. More accurate calculations[1] using the Debye model show that

$$f_{\mathrm{ML}} = \exp\left[-\frac{3E_{\mathrm{R,free}}}{2k_{\mathrm{B}}\theta_{\mathrm{D}}}\left(1 + \frac{4T^2}{\theta_{\mathrm{D}}^2}\int_0^{\theta_{\mathrm{D}}/T}\frac{x}{e^x - 1}dx\right)\right] \tag{2.4}$$

Approximations can be made for two extreme conditions

$$\begin{aligned} f_{\mathrm{ML}} &= \exp\left[-\frac{E_{\mathrm{R,free}}}{k_{\mathrm{B}}\theta_{\mathrm{D}}}\left(\frac{3}{2} + \left[\frac{\pi T}{\theta_{\mathrm{D}}}\right]^2\right)\right], T \ll \theta_{\mathrm{D}} && (2.5) \\ f_{\mathrm{ML}} &= \exp\left[-\frac{E_{\mathrm{R,free}}}{k_{\mathrm{B}}\theta_{\mathrm{D}}}\frac{6T}{\theta_{\mathrm{D}}}\right], \qquad T \gg \theta_{\mathrm{D}} && (2.6) \end{aligned}$$

For Fe, the Debye temperature $\theta_{\mathrm{D}} = 420$K. At room temperature the recoilless fraction is $f_{\mathrm{ML}} = 78\%$. For $\mathrm{Fe_3Al}$, the Debye temperature $\theta_{\mathrm{D}} = 414$K, and $f_{\mathrm{ML}} = 77\%$.

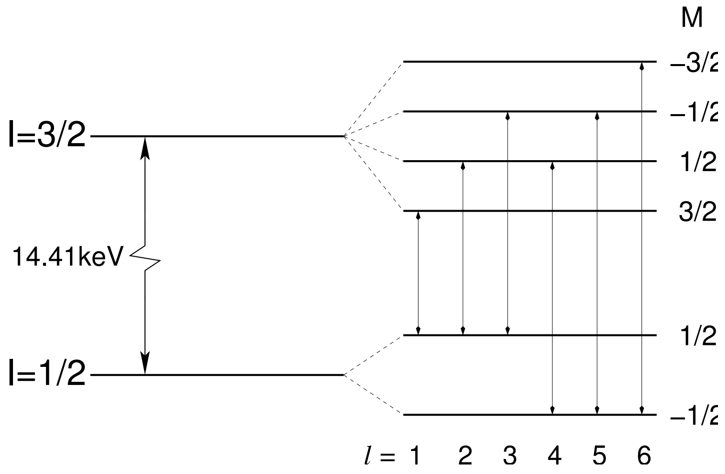

Figure 2.3: Transitions between ground state and 1st excited state of an ^{57}Fe nucleus.

2.2 Nuclear Resonance

We consider further the internal degrees of freedom of the nucleus involved in Mössbauer effect. There are energy levels for a nucleus, just as for an atom. One difference is that the size of a nucleus is much smaller than that of an atom, so the energy associated with a nucleus is much larger than that for an atom. Another unique thing about energy levels of a nucleus is, as we have mentioned before, that the energy widths of nuclear states are small, which indicates longer lifetimes.

Figure 2.3 shows the transitions between the ground state and the 1st-excited state of ^{57}Fe nucleus in a hyperfine magnetic field. The energy of the nuclear states cannot be predicted without knowledge of interaction potentials between nucleons inside the nucleus, which is not the topic of this thesis. Nevertheless, the shifts and splittings of the individual nuclear states caused by the electric or magnetic couplings of the nucleus with electromagnetic fields should be explained because they are important to materials scientists. They can be related to the local atomic environment of the nucleus.

The electromagnetic field at the nucleus caused by electrons nearby can be expanded into components of different parity (electric or magnetic) and different angular momentum (monopole, dipole, or quadrupole, etc.). We now describe some of the most important components.

---

[1] See appendix A.

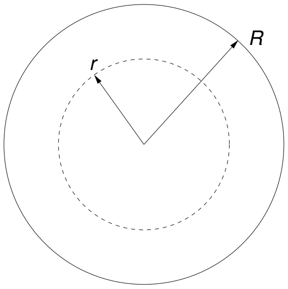

Figure 2.4: A nucleus. It is assumed to have a uniform and spheric charge distribution. The nuclear radius is R.

2.2.1 Isomer Shift

Isomer shifts are caused by an electric monopole interaction, which is the interaction between electrons of the atom and the nucleus. Since the size of the nucleus is much smaller than that of electron orbitals, the wavefunction of an electron in the nucleus can be replaced by $\psi(\mathbf{r}=0)$. Therefore, only s orbital electrons and relativistic p orbital electrons affect the isomer shifts.

Suppose the charge of the nucleus (Ze) is distributed uniformly inside a sphere of size R. The electric field distribution generated by this nucleus is

$$\begin{aligned}\mathbf{E}(\mathbf{r}) &= \frac{Ze}{r^2}\frac{\mathbf{r}}{r}\ (r>R)\\ \mathbf{E}(\mathbf{r}) &= \frac{Ze}{R^2}\frac{r}{R}\frac{\mathbf{r}}{r}\ (r<R)\end{aligned}$$

and the electric potential is

$$\begin{aligned}V(\mathbf{r}) &= \frac{Ze}{r}\ (r>R)\\ V(\mathbf{r}) &= \frac{Ze}{R}(\frac{3}{2}-\frac{r^2}{2R^2})\ (r>R)\end{aligned}$$

The electrostatic energy of the interaction between the charge of the nucleus and the electrons is then

$$\begin{aligned}\Delta E^{0,(e)} &= \int \rho V(\mathbf{r})d\mathbf{r} = \int -e\left|\psi(0)\right|^2 V(\mathbf{r})4\pi r^2 dr\\ &= \frac{2\pi}{5}Ze^2R^2\left|\psi(0)\right|^2\end{aligned}$$

There is usually a difference in the size (R) of the nucleus between the excited states and the ground state, so there is a change of transition energy due to the monopole interaction: $\delta E = \Delta E_1^{0,(e)} - \Delta E_0^{0,(e)}$. Here the subscripts 0 and 1 represents the ground state and the first excited state, respectively. In experiments, we measure the difference of δE between the absorber (subscript A) and the source (subscript S)[2]. This is called the isomer shift

$$\delta = \delta E_{\mathrm{A}} - \delta E_{\mathrm{S}} = \frac{2\pi}{5} Ze^2 (R_1^2 - R_0^2) \left(|\psi_{\mathrm{A}}(0)|^2 - |\psi_{\mathrm{S}}(0)|^2 \right)$$

A measurement of isomer shift provides the information about chemical environments (through $\psi_{\mathrm{A}}(0)$). It is used frequently to identify states of oxidation or spin.

Since a nucleus in a stationary state always has definite parity, it has no electric dipole moment.[3] So the next order of hyperfine interaction is the magnetic dipole interaction.

2.2.2 Magnetic Dipole Hyperfine Interactions

A nucleus with spin will interact with the magnetic field exerted on it and cause splittings of its energy levels. The splittings of the ground state and first-exited state of ^{57}Fe are shown in Fig. 2.3. The energy associated with this interaction is $\Delta E^{1,(m)}$

$$\Delta E^{1,(m)} = -\overrightarrow{\mu} \cdot \mathbf{H} \tag{2.7}$$

A nuclear magnetic dipole is related to its spin by

$$\overrightarrow{\mu}(\mathbf{S}) = g\mu_{\mathrm{N}}\mathbf{S} \tag{2.8}$$

where g is the gyromagnetic ratio, and $\mu_{\mathrm{N}} = \frac{\hbar e}{2m_p}$ is the nuclear magneton. The eigenstates of the Hamiltonian of Eq. 2.7 should be the same eigenstates of operator S_z, where z is the direction of the hyperfine magnetic field $\mathbf{H}_{\mathrm{hf}}$. For a nucleus of total spin I, define

$$\mu = g\mu_{\mathrm{N}} I \tag{2.9}$$

The energy eigenvalues are then

$$\Delta E^{1,(m)}(M) = -g\mu_{\mathrm{N}} H_{\mathrm{hf}} M = -\mu H_{\mathrm{hf}} \frac{M}{I} \tag{2.10}$$

---

[2] The electron wavefunction $\psi(0)$ typically depends on chemical environments. The source and the absorber nuclei likely have different chemical environments.

[3] Please cf., for example, Ref [11], pg 23.

where M is the spin eigenvalue in the z-direction. The possible values for M are $-I, -I+1, \ldots, I$.

More generally, the matrix element of the Hamiltonian for the magnetic dipole interaction in an arbitrarily chosen quantization system is given by

$$\langle IM_1| \mathrm{H}^{1,(m)} |IM_2\rangle = -\mu H_{\mathrm{hf}}(-)^{M_1-M_2} \frac{C(I1I; M_1, M_2-M_1)}{C(I1I; I0)} D^1_{0,M_1-M_2}(0,\theta,\phi) \tag{2.11}$$

where θ, ϕ are spherical coordinates of the hyperfine magnetic field in the chosen quantization system. The Clebsch-Gordan coefficients are denoted by $C(j_1,\, j,\, j_2;\, m_1,\, m)$. The rotation matrices of Rose [46] are denoted by $D^j_{mm'}$.

For ^{57}Fe the ground state of spin $\frac{1}{2}$ splits into 2 sublevels, and the first-excited state of spin $\frac{3}{2}$ splits into 4 sublevels (Fig. 2.3). The two g-factors are

$$g_0 = +0.18121 \tag{2.12}$$

$$g_1 = -0.10348 \tag{2.13}$$

The hyperfine splittings are determined by the hyperfine magnetic fields which, in turn, are determined by the chemical environment of the iron atom. (We will return to this point later.)

2.2.3 Electric Quadrupole Hyperfine Interactions

The shape of a nucleus is not necessarily a sphere. For a non-spherical nucleus, electric quadrupole hyperfine interactions could alter its energy levels if there exists local electric field gradient (EFG). The matrix element of the Hamiltonian for the electric quadrupole interaction in an arbitrarily chosen quantization system is given by

$$\begin{aligned}\langle IM_1| \mathrm{H}^{2,(e)} |IM_2\rangle &= \frac{eqV_{zz}}{2}(-)^{M_1-M_2}\frac{C(I2I; M_1, M_2-M_1)}{2C(I2I; I0)}\big\{D^2_{0,M_1-M_2}(\alpha,\beta,\gamma) \\ &\quad +\eta/6 \times [D^2_{2,M_1-M_2}(\alpha,\beta,\gamma) + D^2_{-2,M_1-M_2}(\alpha,\beta,\gamma)]\big\}\end{aligned} \tag{2.14}$$

where q is the electric quadrupole moment, V_{zz} is the largest eigenvalue of the EFG tensor, and η is the asymmetry parameter of the EFG, α, β, γ denote the Euler angles of the rotation that brings the EFG main axes to the chosen quantization system.

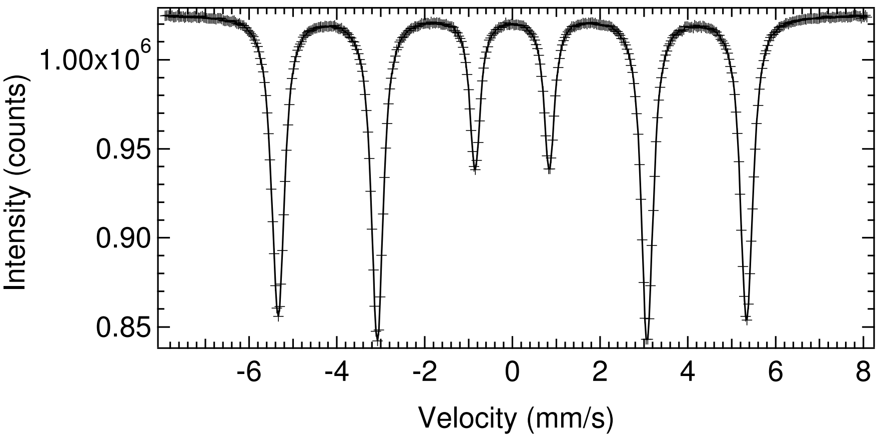

Figure 2.5: A typical Mössbauer spectrum of natural Fe.

2.3 Mössbauer Spectrum of Fe

Pure bcc iron is magnetic at room temperature. There is no electric quadrupole splitting due to symmetry.[4] A typical spectrum of a pure, magnetic iron sample is shown in Fig. 2.5. This spectrum is a sextet (6 nuclear transitions are allowed by the magnetic dipole selection rule). Note that it is symmetric, but its center of symmetry has a offset from $v = 0$ (caused by the isomer shift).

The hyperfine magnetic field of bcc Fe at room temperature is 310kG, and the hyperfine magnetic splitting of nuclear states are as shown in Fig. 2.3. The selection rule for magnetic dipole transitions restricts transitions to $\Delta M = 0, \pm 1$. The energies of six transitions relative to a nucleus in vacuum (no splittings, no isomer shift) are

$$\begin{aligned}
\delta E_1 &= (-\frac{3}{2}\,|g_1| - \frac{1}{2}\,|g_0|)\mu_{\mathrm{N}} H + IS \qquad (2.15)\\
\delta E_2 &= (-\frac{1}{2}\,|g_1| - \frac{1}{2}\,|g_0|)\mu_{\mathrm{N}} H + IS\\
\delta E_3 &= (+\frac{1}{2}\,|g_1| - \frac{1}{2}\,|g_0|)\mu_{\mathrm{N}} H + IS\\
\delta E_4 &= (-\frac{1}{2}\,|g_1| + \frac{1}{2}\,|g_0|)\mu_{\mathrm{N}} H + IS\\
\delta E_5 &= (+\frac{1}{2}\,|g_1| + \frac{1}{2}\,|g_0|)\mu_{\mathrm{N}} H + IS\\
\delta E_6 &= (+\frac{3}{2}\,|g_1| + \frac{1}{2}\,|g_0|)\mu_{\mathrm{N}} H + IS
\end{aligned}$$

---

[4] Actually, a very weak electric quadrupole effect exists because magnetostriction causes a small distortion from cubic symmetry.

The widths of the peaks are determined by both the linewidth of the excited nuclear state and the instrumental broadening. The relative intensities among peaks are determined by the state of the magnetic field in the sample. For a sample of isotropic magnetic field distribution, the relative intensities of the six peaks are

$$I_1 : I_2 : I_3 : I_4 : I_5 : I_6 = 3 : 2 : 1 : 1 : 2 : 3$$

When the direction of the hyperfine magnetic field is parallel to the propagation direction of the γ-ray,

$$I_1 : I_2 : I_3 : I_4 : I_5 : I_6 = 3 : 0 : 1 : 1 : 0 : 3$$

When the direction of the hyperfine magnetic field is perpendicular to the propagation direction of the γ-ray,

$$I_1 : I_2 : I_3 : I_4 : I_5 : I_6 = 3 : 4 : 1 : 1 : 4 : 3$$

2.4 Mössbauer Spectrum of Fe_3Al

2.4.1 Mössbauer Spectrum and HMF Distribution

A typical conversion electron Mössbauer spectrum (CEMS)[5] of highly-ordered Fe_3Al sample is presented in Fig. 2.6. Compared to Fig. 2.5, this spectrum has more features. It is a superposition of sextets with various HMFs[6]. The distribution of ^{57}Fe HMFs can be obtained by processing the experimental spectra with the method of Le Caër and Dubois [36], and an example is presented in Fig. 1.4. In this method a linear dependence of the isomer shift, IS, on the HMF, H, was assumed: $IS = A \times H + B$, where A and B were reported previously to be $A = -1.25 \times 10^{-3}$ mm s^{-1} kG^{-1} and $B = 0.336$ mm s^{-1} [24] .

In the HMF distribution shown in Fig. 1.4, there is a set of independent peaks. These peaks, arranged in order of decreasing HMF, correspond to an increasing number of Al atoms in the first-nearest-neighbors (1nn) shell of the ^{57}Fe atom. The peaks in Fig. 1.4 are labeled by the number (n) of Al first neighbors[7] around the ^{57}Fe atom. The HMF for Fe with (0) Al 1nn is approximately

---

[5] After a Mössbauer nucleus absorbs a photon and jumps to an excited state, it can decay by emitting electrons from the atom. These electrons are called conversion electrons. CEMS measures electron emission, while transmission Mössbauer spectrum measures γ-ray transmission.

[6] We will neglect the effects of EFGs in this work. When an ^{57}Fe atom has Al atoms as nearest neighbors, a weak local EFG is generated. In a polycrystalline sample the orientational distribution of EFG is isotropic and uniform and the net effect is a weak broadening of the absorption lines.

[7] For the purpose of identifying local chemical environments, it is not necessary to modify the interpretations by

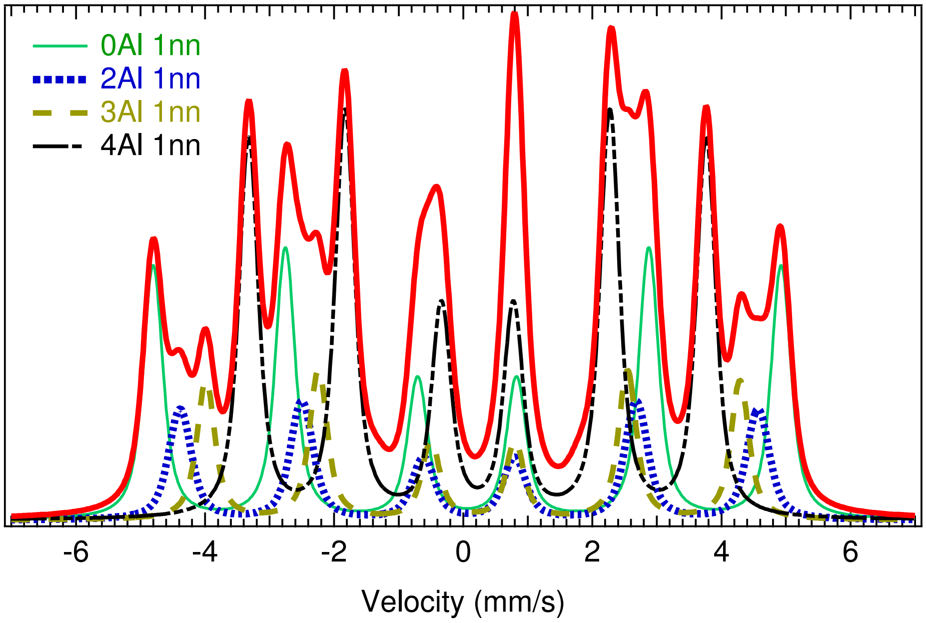

Figure 2.6: CEMS spectrum (thick, solid line) of a partially-ordered Fe3Al sample, and its decomposition into components of various chemical environments (Fe atoms with (0) Al 1nn : thin, solid line; (2) Al 1nn : dotted line; (3) Al 1nn : dashed line; (4) Al 1nn : dash-dot-dot-dot line) .

Table 2.1: First-nearest-neighbor chemical environments in partially-ordered Fe_3Al.

	(0,1) Al	(2) Al	(3) Al	(4)Al	(5) Al
CEMS Spectra	0.290	0.116	0.138	0.388	0.025

310 kG, and that of Fe with (4) Al 1nn is approximately 215 kG. Since the $D0_3$ LRO in our sample is not perfect, there are other environments in the HMF distribution; the most prominent one is the (3) Al 1nn environment, for which the HMF is approximately 255 kG.

To obtain quantitative information from this HMF distribution in Fig. 1.4, we fit it to a set of seven Gaussian functions. The centers and widths of these Gaussians were constrained, but their heights were free to fit the experimental data. The normalized areas of these Gaussians are our experimental probabilities of the different ^{57}Fe 1nn environments, denoted by the number of 1nn Al atoms, (n). Unfortunately, the (0) and (1) Al 1nn environments are nearly indistinguishable in the HMF distribution. Our results for the (0) environment include a partial contribution from the (1) Al 1nn environment. The normalized intensities of peaks in the HMF distribution are nearly equal to the fractions of Fe atoms in each chemical environment. These results are presented in Table 2.1.

2.4.2 Magnetic Polarization Model

As shown in the previous Section, in Fe_3Al different HMFs exist owing to different chemical environments. This phenomenon can be described by the additive perturbation model [23], in which the HMF in an FeX alloy [8] is given by

$$H = H_0 + \Delta H \tag{2.16}$$

$$\Delta H = n_1 \Delta H_1^X + n_2 \Delta H_2^X + \kappa c \tag{2.17}$$

where H_0 is -330 kG at room temperature for an ^{57}Fe nucleus, n_1 and n_2 are the numbers of 1nn and 2nn solute atoms, ΔH_1^X and ΔH_2^X are the HMF perturbations caused by each 1nn and 2nn solute atom, κ is the HMF perturbation caused by 3nn and more distant solute atoms, c is the solute concentration. This model is justified by the magnetic polarization model [23], which describes the origin of the HMF perturbations.

---

effects of 2nn Al atoms [55, 2, 12]. These and more distant neighbors serve only to broaden the 1nn peaks in the HMF distribution [19].

[8] X is the solute, in this case Al.

The HMF originates from the spin-polarization of s-like electrons, which have a non-zero probability of penetrating the ^{57}Fe nucleus. The magnetic polarization model claims that there are two contributions (local and nonlocal) to the HMF perturbation ΔH,

$$\Delta H = \Delta H_{\mathrm{L}} + \Delta H_{\mathrm{NL}} \tag{2.18}$$

The term ΔH_{L} is caused by the unpaired local *3d* electrons, which polarize all of the local s-like electrons near the ^{57}Fe nucleus (*1s*, *2s*, *3s*). Spin polarization of the s-like electrons is caused by the exchange interaction between the unpaired local *3d* electrons and the local s-like electrons, causing differences in the spin-up and spin-down wavefunctions of s-like electrons at the ^{57}Fe nucleus. This contribution can be expressed as

$$\Delta H_{\mathrm{L}} = \alpha \Delta\mu(0) \tag{2.19}$$

where α is a constant parameter, and $\Delta\mu(0)$ is the change of the local atomic magnetic moment[9] of the magnetic *3d* electrons of the ^{57}Fe atom. For FeAl alloys the Al atoms have little effect on the magnetic moment of neighboring Fe atoms, so $\Delta\mu(0) = 0$ and $\Delta H_{\mathrm{L}} = 0$.

The nonlocal contribution, ΔH_{NL}, results from the change of the polarization of nonlocal *4s* electrons in response to the change in magnetic moments at the neighboring atoms. Two mechanisms contribute to ΔH_{NL}: a direct nonlocal term ΔH_{DNL}, which arises from neighboring solute atoms, and an indirect nonlocal term ΔH_{INL}, which arises from neighboring iron atoms whose magnetic moments are perturbed by their neighboring solute atoms. Again, since $\Delta\mu_{\mathrm{Fe}}(0) = 0$, we have $\Delta H_{\mathrm{INL}} = 0$. The only contribution for Al solutes is from ΔH_{DNL}. Therefore,

$$\Delta H = \Delta H_{\mathrm{DNL}} = -\alpha_{\mathrm{CEP}} \sum_{\mathrm{Al\,neighbors}} f(r)\mu_{\mathrm{Fe}}(0) \tag{2.20}$$

where $\mu_{\mathrm{Fe}}(0)$ is the magnetic moment of an iron atom in pure iron, $f(r)$ is the fraction of conduction electron polarization at the ^{57}Fe nucleus produced by a change in the magnetic moment at r, and α_{CEP} is the constant of proportionality for the conduction electron polarization mechanisms. The summation is over all Al neighbors which are crystal sites that have lost their magnetic moment (hence the $-\mu_{\mathrm{Fe}}$ in Eq. 2.20). So for FeAl alloys, the magnetic polarization model reduces to the additive perturbation model and

$$\Delta H_1^{\mathrm{Al}} = -\alpha_{\mathrm{CEP}} f(r_1)\mu_{\mathrm{Fe}}(0) \tag{2.21}$$

---

[9] which is a result of the unpaired local *3d* electrons.

where r_1 is the distance between the first nearest neighbors and the central ^{57}Fe atom.

Chapter 3

Quantum Theory of Mössbauer Absorption and Scattering

In this Section we present the quantum theory describing interaction between a γ-ray photon and a Fe nucleus fixed in the solid. This is a topic of quantum electrodynamics (QED) that is described in many textbooks[1].

In the 1960s there were two major contributions to the theory of Mössbauer optics. Afanas'ev and Kagan developed the dynamical theory of Mössbauer diffraction using mostly classical electrodynamics [1, 31]. Hannon and Trammell developed rigorously a dynamical diffraction theory of coherent elastic scattering in case of sharp nuclear resonances and their formalisms were fully QED[28, 29]. There are publications about the kinematical theory of Mössbauer diffraction[43, 7, 8], but they do not provide a detailed description of the Mössbauer scattering process.

In Hannon and Trammel's paper, the Mössbauer scattering phenomenon was described in detail by QED. However, as a tour de force by experts on QED, few claim to understand this paper. It is a big stretch for an experimentalist to understand this paper. Furthermore, their approach of derivations is rigorous and formal, but lacks an intuitive explanation of the scattering process.

This chapter was written to describe the nuclear resonant scattering processes in a way that helps us experimentalists understand the physics behind those mysterious formalisms, and appreciate the factors affecting the strength of nuclear scattering. It also shows that we are justified in calculating our diffraction intensities with the kinematical theory of Mössbauer diffraction presented in this dissertation. Inevitably we use the QED, for which I will explain the essentials. The mathematical tools necessary for calculating the scattering amplitudes are also presented.

---

[1] There are many textbooks for Quantum Electrodynamics; the one that I read for this work is that of Landau and Lifshitz.

The centerpiece of the formulas presented here is the scattering form factor (Eq. 3.68). It is obtained by first investigating the nature of the photon-nucleus interaction and then calculating amplitudes (and probabilities) of nuclear transition and nuclear resonant scattering processes. We will also find out how those physical quantities depend on the spin of nuclear ground state and the first excited state, the hyperfine fields, and the polarizations of photons (Section 3.1.3). We then obtain the nuclear absorption cross section (Section 3.1.4) and nuclear scattering cross section (Section 3.1.3). The scattering from one ^{57}Fe atom is discussed in Section 3.2.

For simplicity, atomic unit ($\hbar = 1$, $c = 1$) is used. Only the final results will be presented with SI units.

3.1 Interaction of a Photon and a Nucleus

3.1.1 Transition Probability

Consider an isolated nucleus. The rotation symmetry of space requires that the angular momentum is a good quantum number, and any physical process involving this nucleus should conserve the angular momentum. A nucleus has charges, which generate electro-magnetic fields, so it interacts with photons. Consider a process in which a nucleus emits or absorbs a photon (Fig. 3.1). The photon must have definite angular momentum (namely, the eigenstates of angular momentum j and its z component j_z). Such photons can be described with vector spherical harmonic functions, each of which is a field of vectors representing a spatial distribution of amplitudes of vector potential, $\mathbf{A}$, of the electromagnetic field (An example of vector spherical harmonic function is found in Section 3.1.3). We seek to understand how such a photon interacts with a nucleus.

The physics involved here is treated properly by quantum electrodynamics, in which the S-matrix plays the central role. The evolution of a system can be described by its S-matrix. Calculation techniques for the S-matrix of QED, including Feynman diagrams, were developed early in 1940s and 50s[15, 16, 17, 49, 50, 51, 13, 14]. An S-matrix can be expanded into a series of terms of different order[2], in which terms of higher order are of lower amplitudes if the interaction is weak. A term in the series can be expressed by a Feynman diagram, which usually gives a clear physics picture of the term.

The S matrix element of the process shown in Fig. 3.1 (a nuclear transition from state l to state

---

[2] Order means number of interactions involved.

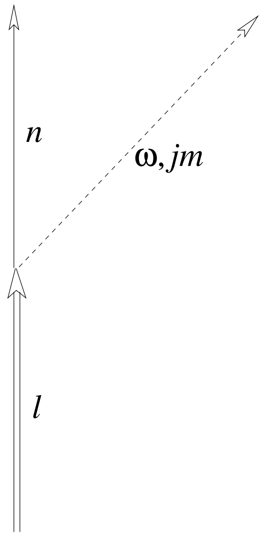

Figure 3.1: Feynman diagram of a first order S-matrix. Time flows forward in the upwards direction. A nucleus is de-excited from state l to state n by emitting a photon of energy $\hbar\omega$ and angular momentum jm.

n with the emission of a photon) is [3]

$$S^{(1)} = -i \langle \omega jm | \langle n | T \left[\int V dt \right] | l \rangle \tag{3.1}$$

where n, l are indexes of the quantum system of the nucleus. The time-ordering operator is denoted by T.[4] The angular momentum of the photon and its z component are j and m. The interaction between a charged particle and a photon is [5]

$$V = \int e j^{\mu} A_{\mu} d^3 x \tag{3.2}$$

where repetition of superscript and subscript indexes means summation. Here, j^{μ} is the current 4-vector for the nucleus, which could be written as a bilinear term composed of the field operator of

---

[3] Actually, if one looks at a S-matrix element, e.g., the one in Eq. 3.1, one can find that it looks very much like a transition matrix element $\langle f | \widehat{O} | i \rangle$, where i denotes the initial state and f the final state, $\widehat{O}$ is a operator consisting of interaction potential.

[4] The time ordering operator greatly simplifies the formalisms in quantum field theories.

[5] One can convince oneself that this is reasonable by looking at the first term: $\int e j^0 A_0 d^3x = \int e\rho\phi \, d^3x$ =static electric energy. Here ϕ is the scalar potential.

the particle

$$j^\mu = \psi^\dagger \gamma^\mu \psi \tag{3.3}$$

$$\psi = \sum c_n \phi_n \tag{3.4}$$

The eigenstates of the Hamiltonian of the nucleus are $\{\phi_n\}$. So we have

$$j^\mu = \sum_{nm} j^\mu_{nm} c^\dagger_n c_m \tag{3.5}$$

where

$$j^\mu_{nm} = \phi^*_n \gamma^\mu \phi_m \tag{3.6}$$

The photon field operator [6], A, which can be seen as the "wavefunction" of a photon, should be expanded with photon "wavefunctions" of definite angular momentum, jm,

$$A = \int d\omega \, \sum_{jm} \left(a_{\omega jm} \chi_{\omega jm} + a^\dagger_{\omega jm} \chi^*_{\omega jm} \right) \tag{3.7}$$

A photon eigenstate of specific angular momentum, $\chi_{\omega jm}$, is easier to write in **k**-space,

$$\chi_{\omega jm}(\mathbf{k}) = \frac{4\pi^2}{\omega^{3/2}} \delta(|\mathbf{k}| - \omega) \mathbf{Y}_{jm}(\mathbf{n}) \tag{3.8}$$

which is basically the vector spherical harmonic function with proper normalization[7]. Its Fourier transform defines the field in real space:

$$\chi_{\omega jm}(\mathbf{x}) = \int \chi_{\omega jm}(\mathbf{k}) \exp{(i\mathbf{k} \cdot \mathbf{x})} \, \frac{d^3k}{(2\pi)^3} \tag{3.9}$$

The orthogonality gives

$$\frac{1}{2\pi} \int \chi^*_{\omega' j' m'}(\mathbf{x}) \chi_{\omega jm}(\mathbf{x}) \omega' \omega d^3x = \omega \delta(\omega' - \omega) \delta_{jj'} \delta_{mm'} \tag{3.10}$$

---

[6] A few more words about quantum electrodynamics: quantum electrodynamics is a quantum field theory, in which the field is quantized. We make the transition from classical mechanics to quantum mechanics by the quantization of physical quantities like position, momentum, Hamiltonian (so they are operators). A second quantization happens when we make the transition to quantum field theory, in which the wavefunctions become field operators.

[7] It is normalized so that the total energy of the electromagnetic field is $\hbar\omega$. See Eq. 3.10.

After substituting Eqs. 3.2, 3.5 and 3.7 into Eq. 3.1, we found

$$\begin{aligned} S^{(1)} &= -i\int d^3x \int dt \int d\omega' \sum_{j'm'}\sum_{n'l'} \Big\langle\Big| a_{\omega jm} c_n c^\dagger_{n'} c_{l'} e^{i(E_{n'}-E_{l'})t} \Big(a_{\omega' j' m'} \chi_{\omega' j' m'}(\mathbf{x}) e^{-i\omega' t} \\ &\quad + a^\dagger_{\omega' j' m'} \chi^*_{\omega' j' m'}(\mathbf{x}) e^{i\omega' t}\Big) j_{n'l'}(\mathbf{x}) c^\dagger_l \Big|\Big\rangle \end{aligned} \tag{3.11}$$

in which we have explicitly written down the time evolution.

To further simplify this expression, recall

$$\langle|\, a_{\omega jm} a^\dagger_{\omega' j' m'} \,|\rangle = \delta(\omega-\omega')\delta_{jj'}\delta_{mm'} \tag{3.12}$$

$$\langle|\, c_n c^\dagger_{n'} \,|\rangle = \delta_{nn'} \tag{3.13}$$

Thus,

$$\begin{aligned} S^{(1)} &= -i\int dt e^{i(E_n-E_l)t} e^{i\omega t} \times \int d^3x\ e\ j_{nl}(\mathbf{x}) \chi^*_{\omega jm}(\mathbf{x}) \qquad (3.14) \\ &= -2\pi i \delta(E_n+\omega-E_l) V_{nl;\omega jm} \qquad (3.15) \end{aligned}$$

where

$$V_{nl;\omega jm} = \int d^3x\ e\ j_{nl}(\mathbf{x}) \chi^*_{\omega jm}(\mathbf{x}) \tag{3.16}$$

The delta function signifies conservation of energy. The transition probability per unit time for such a process is then [8]

$$\frac{dw}{dt} = 2\pi\delta(E_n+\omega-E_l)\left|V_{nl;\omega jm}\right|^2 d\omega \tag{3.17}$$

The result is natural since the transition probability increases as the interaction becomes stronger. Integration over energy gives the transition probability per unit time accompanied by emission of photons

$$\frac{dw}{dt} = 2\pi\left|V_{nl;\omega jm}\right|^2, where\ \omega = E_l - E_n \tag{3.18}$$

which is just Fermi's Golden Rule.

3.1.2 Interaction Matrix Element of Magnetic Transition

The interaction matrix element in Eq. 3.16 is the key to our problem. For ^{57}Fe Mössbauer experiments, only the transition to the first excited state is important. This transition is of pure magnetic

---

[8] The mathematics can be found in, for example, Landau and Lifshitz, Quantum Mechanics, 3rd edition, pg 152.

dipole character. If we concern ourselves exclusively with magnetic transitions, the interaction potential (cf. Landau and Lifshitz, QED, 2nd Edition, Pergamon Press, pg 171)

$$V_{nl;\omega jm} = (-)^m i^j \sqrt{\frac{(2j+1)(j+1)}{\pi j}} \frac{\omega^{j+\frac{1}{2}}}{(2j+1)!!} \langle n| Q^{(m)}_{j,-m} |l\rangle , \tag{3.19}$$

where

$$\langle n| Q^{(m)}_{j,-m} |l\rangle = e\frac{1}{j+1}\sqrt{\frac{4\pi}{2j+1}} \int \mathbf{r}\times\mathbf{j}_{nl}\cdot\nabla(r^j Y_{jm})d^3x \tag{3.20}$$

is called the 2^j-pole magnetic transition moment. We cannot obtain the value of this term without detailed knowledge of the nucleus. For our isolated nucleus, however, the angular momentum is a good quantum number, and we have

$$|l\rangle = |N\rangle\,|IM\rangle \tag{3.21}$$

where N denotes all quantum numbers except those of angular momentum, I and M are angular momentum and its z component, respectively. Then with Wigner-Eckardt theorem[9], one has

$$\langle n_2 I_2 M_2| Q^{(m)}_{j,-m} |n_1 I_1 M_1\rangle = i^j (-)^{I_{max}-M_2} \begin{pmatrix} I_2 & j & I_1 \\ -M_2 & -m & M_1 \end{pmatrix} \left\langle n_2 I_2 \left\| Q^{(m)}_j \right\| n_1 I_1 \right\rangle \tag{3.22}$$

where $\left\langle n_2 I_2 \left\| Q^{(m)}_j \right\| n_1 I_1 \right\rangle$ is the "reduced" transition matrix element, and $\begin{pmatrix} j_2 & j & j_1 \\ -m_2 & -m & m_1 \end{pmatrix}$ is the *3j* symbol. If we define a "reduced" interaction potential

$$V_{n_2 I_2 \leftarrow n_1 I_1;\omega j} = (-)^m i^j \sqrt{\frac{(2j+1)(j+1)}{\pi j}} \frac{\omega^{j+\frac{1}{2}}}{(2j+1)!!} \left\langle n_2 I_2 \left\| Q^{(m)}_j \right\| n_1 I_1 \right\rangle \tag{3.23}$$

then we have

$$V_{n_2 I_2 M_2 \leftarrow n_1 I_1 M_1;\omega jm} = i^j (-)^{I_{max}-M_2} \begin{pmatrix} I_2 & j & I_1 \\ -M_2 & -m & M_1 \end{pmatrix} V_{n_2 I_2 \leftarrow n_1 I_1;\omega j} \tag{3.24}$$

The transition rate of an excited state is the sum of those of all possible transitions

$$\Gamma_{N,\gamma} \;=\; 2\pi \sum_{M_0} \left|V_{0 I_0 M_0 \leftarrow N I_N M_N;\omega jm}\right|^2 \tag{3.25}$$

---

[9] This theorem concerns the addition of two angular momenta. The result of this theorem is that the matrix element of a spherical tensor can be split into two parts; one depends only on the angular momenta, while the other (expressed by a Clebsch-Gordan coefficient) depends also on their z-components.

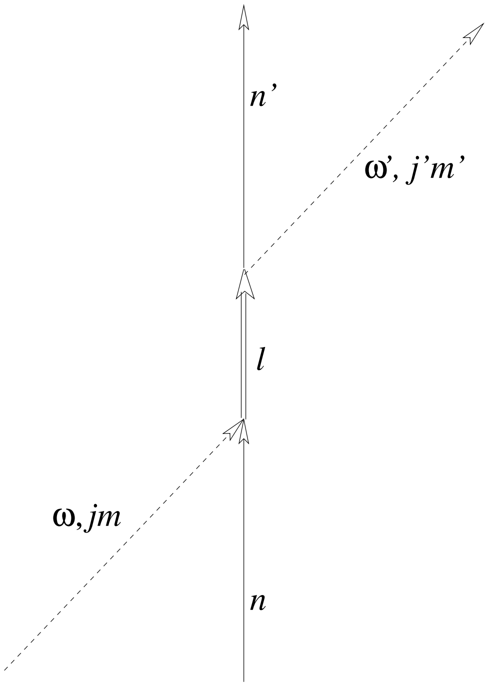

Figure 3.2: Feynman diagram of a second-order S-matrix. Time flows forward in the upwards direction. A nucleus of state $|n\rangle$ combines with a photon $|\omega jm\rangle$ and forms a nucleus of state $|l\rangle$; it then de-excites to state $|n'\rangle$ by emitting a photon $|\omega' j' m'\rangle$.

$$= \frac{2\pi}{2I_N+1}\left|V_{0I_0 \leftarrow LI_N;\omega jm}\right|^2 \tag{3.26}$$

where $\omega = E_N - E_0,\ j = I_N - I_0,\ m = M_N - M_0$. Here, we use the subscript γ to indicate that this line-width of excited state is due to the electromagnetic radiation. Equation 3.26 relates the transition rate of nuclear excited state resulted from radiation to the reduced interaction potential defined in Eq. 3.23.

3.1.3 Scattering

Scattering of a Photon with Definite Angular Momentum

Consider the scattering of a photon by a fixed nucleus. The process can be regarded as three steps (Fig. 3.2): 1. the nucleus gets excited from $|n\rangle$ to $|l\rangle$ by absorbing a photon; 2. the nucleus stays in state $|l\rangle$ for a while; 3. a photon is emitted while the nucleus jumps to state $|n'\rangle$. The amplitude of such a process could be calculated from the second-order S matrix shown in Fig. 3.2.

Using techniques similar to those in the previous Section, we obtain

$$\begin{aligned}
\langle \omega jm | \langle n | S^{(2)} | n' \rangle | \omega' j' m' \rangle &= \frac{(-i)^2}{2} \langle \omega jm | \langle n | T \left[\int V(t_1) dt_1 \int V(t_2) dt_2 \right] | n' \rangle | \omega' j' m' \rangle \qquad (3.27) \\
&= -\frac{1}{2} \left\langle \middle| a_{\omega jm} c_n T \left\{ \int dt_1 \int dt_2 \int d^3x_1 \int d^3x_2 \right.\right. \\
&\quad \sum_{n_1 l_1} j_{n_1 l_1}(\mathbf{x}_1) c^\dagger_{n_1}(t_1) c_{l_1}(t_1) \int d\omega_1 \sum_{j_1 m_1} \\
&\qquad \Big(a_{\omega_1 j_1 m_1}(t_1) \chi_{\omega_1 j_1 m_1}(\mathbf{x}_1) + a^\dagger_{\omega_1 j_1 m_1}(t_1) \chi^*_{\omega_1 j_1 m_1}(\mathbf{x}_1) \Big) \\
&\quad \sum_{n_2 l_2} j_{n_2 l_2}(\mathbf{x}_2) c^\dagger_{n_2}(t_2) c_{l_2}(t_2) \int d\omega_2 \sum_{j_2 m_2} \\
&\qquad \left. \Big(a_{j_2 m_2}(t_2) \chi_{\omega_2 j_2 m_2}(\mathbf{x}_2) + a^\dagger_{\omega_2 j_2 m_2}(t_2) \chi^*_{\omega_2 j_2 m_2}(\mathbf{x}_2) \Big) \right\} \\
&\quad \left. c^\dagger_{n'} a^\dagger_{\omega' j' m'} \middle| \right\rangle \qquad (3.28)
\end{aligned}$$

Considering the commutation relations, the normalization conditions, and the unperturbed Green's function[10] for the nucleus

$$G^{(0)}(l, t - t') = -i \, {}_0\left\langle \middle| T C_l(t) C^\dagger_l(t') \middle| \right\rangle_0 , \qquad (3.29)$$

we have

$$\begin{aligned}
\langle \omega jm | \langle n | S^{(2)} | n' \rangle | \omega' j' m' \rangle &= -\int_{-\infty}^{\infty} dt_1 \int_{-\infty}^{\infty} dt_2 \sum_l V_{nl;\omega jm} V_{ln';\omega' j' m'} e^{iE_n t_1} e^{i\omega t_1} \\
&\quad \times i G^{(0)}(l, t_1 - t_2) e^{-i\omega' t_2} e^{-iE_{n'} t_2} \qquad (3.30) \\
&= -i \int_{-\infty}^{\infty} dt_1 \int_{-\infty}^{\infty} dt_2 \sum_l V_{nl;\omega jm} V_{ln';\omega' j' m'} e^{i(E_n + \omega) t_1} \\
&\quad \times \int dE \frac{1}{2\pi} G^{(0)}(l, E) e^{-iE(t_1 - t_2)} e^{-i(E_{n'} + \omega') t_2} \\
&= -i \sum_l \int dE \frac{1}{2\pi} G^{(0)}(l, E) 2\pi \delta(E_n + \omega - E) \\
&\quad \times 2\pi \delta(E_{n'} + \omega' - E) V_{nl;\omega jm} V_{ln';\omega' j' m'} \\
&= -2\pi i \delta(E_n + \omega - E_{n'} - \omega') \times \sum_l G^{(0)}(l, E_n + \omega) V_{nl;\omega jm} V_{ln';\omega' j' m'} \qquad (3.31)
\end{aligned}$$

---

[10] For the Green's function, I used the conventions in Mahan's textbook "Many-Particle Physics". For example, $|\rangle$ denotes the ground state of Hamiltonian with interaction, while $|\rangle_0$ denotes the ground state of Hamiltonian without interaction.

Here, l indicates the energy state of the nucleus

$$|l\rangle = |N\rangle\,|IM\rangle \tag{3.32}$$

So

$$\sum_l = \sum_{NIM} \tag{3.33}$$

The sum over N can reduce to just one term if the energy levels of the nucleus are well-separated, compared to the energy line-width of the state. In our case, this is always true; the energy levels are far apart, whereas the sublevels of an energy state are degenerate (e.g. Fe nucleus without an external field), or very close to each other (e.g. hyperfine splittings of an Fe nucleus in an external magnetic field). Thus, the sum over l reduces to a sum over sublevels of one excited state that is on resonance with the incident γ-ray. At room temperature, essentially all nuclei are in their ground states, so $N = N' = 0$ (The quantum number M_0 and M_0' could differ)

$$\begin{aligned}\langle \omega jm|\,\langle 0I_0M_0|\,S^{(2)}\,|0I_0M_0'\rangle\,|\omega' j' m'\rangle &= -2\pi i\delta(E_{0I_0M_0} + \omega - E_{0I_0M_0'} - \omega')\sum_{M_N} \\ &\quad V_{NI_NM_N\leftarrow 0I_0M_0;\omega jm} G^{(0)}(NI_NM_N, E_{0I_0M_0} + \omega) \\ &\quad \times V_{0I_0M_0'\leftarrow NI_NM_N;\omega' jm'}\end{aligned} \tag{3.34}$$

here N is the only energy level that is on resonance with the gamma ray energy, i.e., $(E_N - E_0) \sim \omega \sim \omega'$.

For elastic scattering, $\omega = \omega'$. For coherent elastic scattering, "spin-flip"-like phenomenon[11] does not contribute. Thus, for coherent elastic scattering, we need to evaluate

$$\begin{aligned}\langle \omega jm|\,\langle 0I_0M_0|\,S^{(2)}\,|0I_0M_0\rangle\,|\omega jm\rangle &= -2\pi i\sum_{M_N} |V_{NI_NM_N\leftarrow 0I_0M_0;\omega jm}|^2\, G^{(0)}(NI_NM_N, E_{0I_0M_0} + \omega) \\ &= -2\pi i\sum_{M_N}\left|\begin{pmatrix} I_0 & j & I_N \\ -M_0 & -m & M_N\end{pmatrix} V_{0I_0\leftarrow NI_N;\omega j}\right|^2 \\ &\quad \times G^{(0)}(NI_NM_N, E_{0I_0M_0} + \omega) \qquad (3.35) \\ &= -i\sum_{M_N} \Gamma_{N,\gamma}\,|C(I_0jI_N; M_0, m)|^2\,\delta_{M_N, M_0+m}\end{aligned}$$

---

[11] For ^{57}Fe nucleus, the ground state is a spin $\frac{1}{2}$ state. The original state could be spin-up or spin-down. After scattering this ^{57}Fe nucleus could go back to the original spin state or the state with opposite spin. The latter phenomenon is named "spin-flip". It will be clear in section 3.1.3 that such processes are not coherent.

$$\times G^{(0)}(NI_NM_N, E_{0I_0M_0}+\omega) \tag{3.36}$$

In the last step, Eq. 3.26 was used. The amplitude of scattering process shown in Fig. 3.2 is related to the line-width of nuclear excited state due to emmission of γ-ray and the Green function of this state.

Beyond Second-Order Perturbation Theory

The previous derivations were only up to the second order in a perturbation expansion ($S^{(2)}$). More precise results can be obtained from QED: helping to justify this approach. With Feynman diagrams we can see that higher order terms serve only to change the energy and the half-width of the excited state of the nucleus. Actually the unperturbed Green's function in, for example, Eq. 3.36 must be replaced with the normal Green's function

$$G(l,t-t') = -i\left\langle \middle| TC_l(t)C_l^\dagger(t') \middle| \right\rangle . \tag{3.37}$$

One example of high-order S-matrix is shown in Fig. 3.3.

More precisely, when all high-order S-matrixes are considered, both Eq. 3.18 and 3.35 need revision. However, the net effect to Eq. 3.36 is only the replacement of $G^{(0)}$ by G.[12]

Scattering Form Factor

Here we develop the scattering form factor. In formal scattering theory, the incident wave is treated as a plane wave:

$$\psi^{in} = e^{i\mathbf{k}\cdot\mathbf{r}} \tag{3.38}$$

At a distance, $\mathbf{r}$, far from the scattering center, the scattered wave is

$$\psi^{sc} = f(\theta)\frac{e^{i\mathbf{k}\cdot\mathbf{r}}}{r} \tag{3.39}$$

which is like a spherical wave, but with an angular dependency factor, $f(\theta)$, called the scattering amplitude. The scattering amplitude of a nuclear resonant scattering process is also called the form factor for nuclear resonant scattering.

We need to evaluate how a plane wave photon (i.e., a photon with definite momentum) is scattered

---

[12] This is true also because diagrams like the one shown in Fig. 3.4 with disconnected radiative parts give igonorable radiative corrections to the graound-state energy[28].

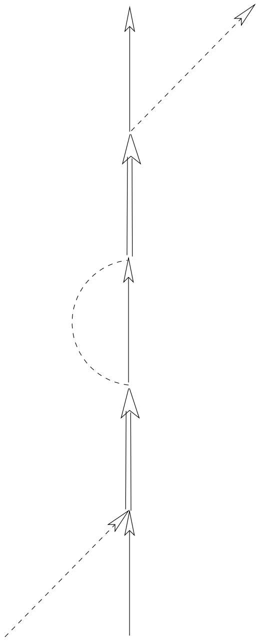

Figure 3.3: An example of high-order S-matrix representing scattering process.

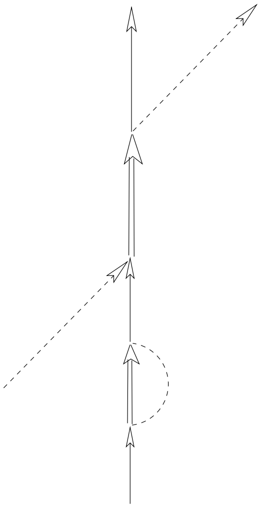

Figure 3.4: A diagram with an ignorable correction to nuclear ground-state energy.

by a nucleus. The vector potential of such a photon could be described by $|\mathbf{k}\alpha\rangle$

$$\langle \mathbf{x}|\mathbf{k}\alpha\rangle = A_{\mathbf{k}\alpha}(\mathbf{x}) = \sqrt{4\pi}\frac{\mathbf{e}^{(\alpha)}}{\sqrt{2\omega}}e^{i\mathbf{k}\cdot\mathbf{x}} \tag{3.40}$$

The amplitude of a process in which a photon with definite momentum is scattered by a nucleus into a photon with definite angular momentum is then given by the S-matrix

$$\left\langle \omega'j'm'\right|\left\langle 0I_0M_0\right| S \left|0I_0M_0\right\rangle\left|\mathbf{k}\alpha\right\rangle = \int d\omega_1 \sum_{j_1m_1}\left\langle \omega'j'm'\right|\left\langle 0I_0M_0\right| S \left|0I_0M_0\right\rangle\left|\omega_1j_1m_1\right\rangle\left\langle \omega_1j_1m_1\right|\mathbf{k}\alpha\rangle \tag{3.41}$$

For coherent elastic scattering,

$$\begin{aligned}\left\langle \omega'j'm'\right|\left\langle 0I_0M_0\right| S \left|0I_0M_0\right\rangle\left|\mathbf{k}\alpha\right\rangle_{\mathrm{coh,el}} &= \left\langle \omega'j'm'\right|\left\langle 0I_0M_0\right| S \left|0I_0M_0\right\rangle\left|\omega'j'm'\right\rangle\left\langle \omega'j'm'\right|\mathbf{k}\alpha\rangle \\ &= -i\sum_{M_L}\Gamma_{N,\gamma}\left|C(I_0j'I_N;M_0,m')\right|^2\delta_{M_N,M_0+m} \\ &\quad \times G(NI_NM_N,E_{0I_0M_0}+\omega')\left\langle \omega'j'm'|\mathbf{k}\alpha\right\rangle \end{aligned} \tag{3.42}$$

The problem now is to evaluate the projection coefficient between the photon state of definite angular momentum and the photon states of definite momentum, $\langle\omega'j'm'|\mathbf{k}\alpha\rangle$. First we note that using the normalization condition of $|\omega jm\rangle$, we can show that if a photon wavefunction $A(x)$ can be expanded as

$$A(\mathbf{x}) = \sum_{jm}\int a_{jm}(\omega)A_{\omega jm}(\mathbf{x})d\omega \tag{3.43}$$

then we have

$$\int A^*_{\omega'j'm'}(\mathbf{x})A(\mathbf{x})d^3x = \frac{2\pi}{\omega'}a_{j'm'}(\omega') \tag{3.44}$$

So

$$\langle\omega'j'm'|\mathbf{k}\alpha\rangle = \frac{\omega'}{2\pi}\int A^*_{\omega'j'm'}(\mathbf{x})A_{\mathbf{k}\alpha}(\mathbf{x})d^3x \tag{3.45}$$

$$\begin{aligned}\int A^*_{\omega'j'm'}(\mathbf{x})A_{\mathbf{k}\alpha}(\mathbf{x})d^3x &= \frac{(2\pi)^{5/2}}{\omega'^2}\int d^3k'/(2\pi)^3\delta(|\mathbf{k}'|-\omega')(\mathbf{e}^{(\alpha)}\cdot\mathbf{Y}^*_{j'm'}(\mathbf{n}'))\int d^3xe^{i\mathbf{k}\cdot\mathbf{x}}e^{-i\mathbf{k}'\cdot\mathbf{x}} \\ &= \frac{(2\pi)^{5/2}}{\omega'^2}\delta(|\mathbf{k}|-\omega')\left[\mathbf{e}^{(\alpha)}\cdot\mathbf{Y}^*_{j'm'}(\mathbf{n})\right] \end{aligned} \tag{3.46}$$

$$\langle\omega'j'm'|\mathbf{k}\alpha\rangle = \frac{(2\pi)^{3/2}}{\omega'}\delta(|\mathbf{k}|-\omega')\left[\mathbf{e}^{(\alpha)}\cdot\mathbf{Y}^*_{j'm'}(\mathbf{n})\right] \tag{3.47}$$

Thus for an incident plane wave, the scattered wave takes the form

$$\begin{aligned}
|\mathbf{k}\alpha\rangle \rightarrow Scattered &\rightarrow A^{sc}(\mathbf{x}) \\
&= \int d\omega' \sum_{j'm'} |\omega' j' m'\rangle \langle \omega' j' m' | \langle 0 I_0 M_0 | \, S \, | 0 I_0 M_0 \rangle | \, \mathbf{k}\alpha\rangle \qquad (3.48) \\
&= -i \sum_m \Gamma_{N,\gamma} \left| C(I_0 j I_N; M_0, m) \right|^2 G(L I_N M_N, E_{0 I_0 M_0} + \omega) \\
&\quad \times \frac{(2\pi)^{3/2}}{\omega} \left[\mathbf{e}^{(\alpha)} \cdot \mathbf{Y}^{*}_{jm}(\mathbf{n}) \right] |\omega j m\rangle \\
&= \sqrt{\frac{2\pi}{\omega}} C \, |\omega j m\rangle \qquad (3.49)
\end{aligned}$$

where

$$C = -i \sum_m \Gamma_{N,\gamma} \left| C(I_0 j I_N; M_0, m) \right|^2 G(N I_N M_N, E_{0 I_0 M_0} + \omega) \frac{(2\pi)}{\sqrt{\omega}} \left[\mathbf{e}^{(\alpha)} \cdot \mathbf{Y}^{*}_{jm}(\mathbf{n}) \right] \qquad (3.50)$$

Here N denotes the single energy level that is on resonance with the gamma ray energy, i.e., $(E_N - E_0) \sim \omega \sim \omega'$. $j = I_N - I_0$. The photon energy $\omega = |\mathbf{k}|$, direction $\mathbf{n} = \frac{\mathbf{k}}{k}$. Equation 3.49 shows that the scattered wave is a photon state with definite angular momentum. To find the scattering form factor, we need to express the scattered wave as a spherical wave $f(\theta)\frac{exp(i\mathbf{k}\cdot\mathbf{r})}{r}$, because, in formal scattering theory, the total wavefunction is the sum of Eq. 3.38 and 3.39

$$\begin{aligned}
\psi &= \psi^{in} + \psi^{sc} \qquad (3.51) \\
&= e^{i\mathbf{k}\cdot\mathbf{x}} + f(\mathbf{k}) \frac{e^{ikr}}{r} \qquad (3.52)
\end{aligned}$$

For the nuclear resonant scattering, the total photon wavefunction is

$$\begin{aligned}
A(\mathbf{x}) &= S \, A^{in}(\mathbf{x}) = (S^{(0)} + S^{(2)}) \, A^{in}(\mathbf{x}) \\
&= \sqrt{4\pi} \frac{\mathbf{e}^{(\alpha)}}{\sqrt{2\omega}} e^{i\mathbf{k}\cdot\mathbf{x}} + \sqrt{\frac{2\pi}{\omega}} C \, A_{\omega jm}(\mathbf{x}) \qquad (3.53) \\
&= \sqrt{\frac{4\pi}{2\omega}} \mathbf{e}^{(\alpha)} \left\{ e^{i\mathbf{k}\cdot\mathbf{x}} + C \, A_{\omega jm}(\mathbf{x}) \right\} \qquad (3.54)
\end{aligned}$$

Now we want to know how $A_{\omega jm}$ behaves when $kr \gg 1$ (distance that is far away from the scattering center). Recall the well-know formula

$$e^{i\mathbf{k}\cdot\mathbf{r}} = \sum_{lm} g_l(kr) Y_{lm}(\frac{\mathbf{k}}{k}) Y_{lm}(\frac{\mathbf{r}}{r}) \qquad (3.55)$$

and

$$g_l(z) \approx 4\pi \frac{i^l}{z} \sin(z - \frac{\pi}{2} l) = -2\pi i \frac{e^{iz} - (-)^l e^{-iz}}{z} \text{ if } z \gg 1 \tag{3.56}$$

Only the outgoing wave is relevant, so we have

$$\begin{aligned} \left[e^{i\mathbf{k}\cdot\mathbf{r}}\right]^{out} &\approx -2\pi i \frac{e^{ikr}}{kr} \sum_{lm} Y_{lm}(\frac{\mathbf{k}}{k}) Y_{lm}(\frac{\mathbf{r}}{r}) & (3.57) \\ &= -2\pi i \frac{e^{ikr}}{kr} \delta(\mathbf{n} - \frac{\mathbf{r}}{r}) & (3.58) \end{aligned}$$

In the second step the completeness of spherical harmonic functions is used. Thus,

$$\begin{aligned} A^{out}_{\omega jm}(\mathbf{r}) &\approx -i \int \frac{1}{\omega^{3/2}} \delta(|\mathbf{k}| - \omega) \mathbf{Y}_{jm}(\mathbf{n}) \frac{e^{ikr}}{kr} \delta(\mathbf{n} - \frac{\mathbf{r}}{r}) k^2 dk d\Omega & (3.59) \\ &= -\frac{i}{\sqrt{\omega}} \mathbf{Y}_{jm}(\frac{\mathbf{r}}{r}) \frac{e^{i\omega r}}{r} & (3.60) \end{aligned}$$

After substituting Eq. 3.60 into Eq. 3.53 and compare it to Eq. 3.51, we obtained the form factor

$$\begin{aligned} f(\mathbf{k}_i, \mathbf{e}_i \to \mathbf{k}_f, \mathbf{e}_f) &= -\frac{i}{\sqrt{\omega}} C \left[\mathbf{e}^{(f)*} \cdot \mathbf{Y}_{jm}(\mathbf{n}_f)\right] & (3.61) \\ &= -\frac{(2\pi)}{\omega} \sum_m \Gamma_{N,\gamma} G(N I_N M_N, E_{0 I_0 M_0} + \omega) \\ &\quad \times \left[\mathbf{e}^{(i)} \cdot \mathbf{Y}^*_{jm}(\mathbf{n}_i)\right] \left[\mathbf{e}^{(f)*} \cdot \mathbf{Y}_{jm}(\mathbf{n}_f)\right] |C(I_0 j I_N; M_0, m)|^2 & (3.62) \end{aligned}$$

The Green's function of a nucleus takes the form

$$G(l, E) = \frac{1}{E - (E_l - E_0) + i\Gamma_l/2}\,. \tag{3.63}$$

Here, the line-width Γ_l includes not only the contribution from radiation, but also contributions from other transition channels, for example, the internal conversion, in which an inner shell electron of an atom is emitted by the energy of nuclear transition. This means we must extend our analysis from an isolated nucleus to a nucleus in an atom. Therefore, we have

$$\begin{aligned} f(\mathbf{k}_i, \mathbf{e}_i \to \mathbf{k}_f, \mathbf{e}_f) &= -\frac{(2\pi)}{\omega} \sum_m \frac{\Gamma_{N,\gamma}}{E_{0 I_0 M_0} + \omega - E_{N I_N M_N} + i\frac{\Gamma_N}{2}} \\ &\quad \times \left[\mathbf{e}^{(i)} \cdot \mathbf{Y}^*_{jm}(\mathbf{n}_i)\right] \left[\mathbf{e}^{(f)*} \cdot \mathbf{Y}_{jm}(\mathbf{n}_f)\right] |C(I_0 j I_N; M_0, m)|^2 & (3.64) \\ &= \frac{4\pi}{\omega} \sum_m \frac{1}{1 + \alpha_{\text{IC}}} \frac{1}{z_{N,M_N;0,M_0}(\omega) - i} \end{aligned}$$

$$\times \left[\mathbf{e}^{(i)} \cdot \mathbf{Y}^*_{jm}(\mathbf{n}_i)\right] \left[\mathbf{e}^{(f)*} \cdot \mathbf{Y}_{jm}(\mathbf{n}_f)\right] \left|C(I_0 j I_N; M_0, m)\right|^2 \qquad (3.65)$$

where the normalized energy shift is

$$z_{N,M_N;0,M_0}(\omega) = \frac{2}{\Gamma_N}(E_{NI_NM_N} - E_{0I_0M_0} - \hbar\omega)\,. \qquad (3.66)$$

The internal conversion factor, α_{IC}, is defined as

$$\alpha_{\mathrm{IC}} = \frac{\Gamma_N - \Gamma_{N,\gamma}}{\Gamma_{N,\gamma}} \qquad (3.67)$$

In the SI units, we have[13]

$$\begin{aligned} f_{\mathrm{nuc}}(\mathbf{k}_i, \mathbf{e}_i \quad &\rightarrow \quad \mathbf{k}_f, \mathbf{e}_f) = \frac{4\pi}{k} \sum_m \frac{1}{1+\alpha_{\mathrm{IC}}} \frac{1}{z_{N,M_N;0,M_0}(\omega) - i} \\ &\times \left[\mathbf{e}^{(i)} \cdot \mathbf{Y}^*_{jm}(\mathbf{n}_i)\right] \left[\mathbf{e}^{(f)*} \cdot \mathbf{Y}_{jm}(\mathbf{n}_f)\right] \left|C(I_0 j I_N; M_0, m)\right|^2 \qquad (3.68) \end{aligned}$$

The subscript *nuc* is used to indicate that it is the nuclear scattering form factor.

Since this formula is the starting point of the simulation of diffraction intensities using kinematical diffraction theory, it deserves a little more explanation. First note that the form factor has the unit of length owing to the wavelength of the photon, $\frac{2\pi}{k}$, as a prefactor. The internal conversion coefficient, α, enters this formula because the interaction with electromagnetic field is not the only way for a nucleus to de-excite. A close examination of the term $\frac{1}{z_{L,M_L;0,M_0}(\omega)-i}$ reveals that its absolute square is just a Lorentzian function, which shows the typical behavior of a resonance system. Clebsch-Gorden coefficients come from the multipole transition matrix element. The terms of form $\left[\mathbf{e} \cdot \mathbf{Y}^*_{jm}(\mathbf{n})\right]$ are polarization factors, which are discussed more later in this Section.

Spin Flip

In Eq. 3.68, the spin flip phenomenon is not included. When the spin-flip phenomenon is considered, the polarization factors $\left[\mathbf{e}^{(i)} \cdot \mathbf{Y}^*_{jm}(\mathbf{n}_i)\right] \left[\mathbf{e}^{(f)*} \cdot \mathbf{Y}_{jm}(\mathbf{n}_f)\right]$ should be changed to

$$p = \left[\mathbf{e}^{(i)} \cdot \mathbf{Y}^*_{jm_i}(\mathbf{n}_i)\right] \left[\mathbf{e}^{(f)*} \cdot \mathbf{Y}_{jm_f}(\mathbf{n}_f)\right]\,, \qquad (3.69)$$

---

[13] We only need to put the photon speed, c, back into the formula to give the scattering amplitude the units of length.

which shows that the scattered photon might have a different angular-momentum quantum-number than the incident photon. If we intentionally evaluate Eq. 3.69 with a spin-flip process, i.e., m_i differing from m_f , it can be shown that the scattering amplitude has a phase factor that depends on the choice of the coordinate system, i.e., the phase factor is not well-defined. Scattering from a nucleus without a well-defined phase cannot be coherent with scattering from other nuclei, so spin-flip processes are incoherent.

Scattering Cross Section

The nuclear scattering differential cross section is obtained by

$$\frac{d\sigma_{\mathrm{nuc}}}{d\Omega} = |f_{\mathrm{nuc}}|^2 \tag{3.70}$$

Polarization Factor for Magnetic Dipole Transition

For ^{57}Fe, the transition from the first excited state to the ground state is a magnetic dipole transition. Equation 3.68 can be rewritten as

$$f_{\mathrm{nuc}} = \frac{3}{2k(1+\alpha_{\mathrm{IC}})} \sum_m \frac{\left(\sqrt{\frac{8\pi}{3}}\mathbf{e}_i^* \cdot \mathbf{Y}_{1m}^{(m)}(\mathbf{n}_i)\right)^* \left(\sqrt{\frac{8\pi}{3}}\mathbf{e}_f^* \cdot \mathbf{Y}_{1m}^{(m)}(\mathbf{n}_f)\right)}{z_{1M_1;0M_0}(\omega) - i} C(\frac{1}{2}1\frac{3}{2}; M_0 m)^2 \tag{3.71}$$

A polarization factor, as used in literature, could be defined as [14]

$$\begin{aligned} p_l &= -i\sqrt{\frac{8\pi}{3}}[\mathbf{e}^* \cdot \mathbf{Y}_{1m}^{(m)}(\mathbf{n})] && (3.72) \\ &= (\mathbf{h} \cdot \mathbf{u}_l) && (3.73) \end{aligned}$$

Here, $\mathbf{Y}_{1m}^{(m)}(\mathbf{n})$ is a spheric harmonic vector, which describes the wavefunction of a magnetic dipole photon with z-direction angular momentum m in the momentum representation. The direction of the momentum of the photon, **p,** is specified by $\mathbf{n} = \frac{\mathbf{p}}{p}$. The unit vector of the electric field of the plane wave for the incident or outgoing photon is **e**, while **h** is the unit vector of the magnetic field. Spherical vectors, $\{\mathbf{u}\}$, are defined as

---

[14] Please cf, for example, reference [63]

$$
\begin{aligned}
\mathbf{u}_l &= \mathbf{u}_z \;\; if\, m = 0 && (3.74)\\
&= \mp\frac{1}{\sqrt{2}}(\mathbf{u}_x \pm i\mathbf{u}_y) \;\; if\, m = \pm 1 && (3.75)
\end{aligned}
$$

where $\mathbf{u}_x, \mathbf{u}_y, \mathbf{u}_z$ span a coordinate system, with $\mathbf{u}_z$ pointing to the direction of the quantization direction of the nucleus. In our case, $\mathbf{u}_z$ is usually parallel to the direction of hyperfine magnetic field.[15]

To illustrate the angular dependence (see Fig. 3.5) of the polarization factor (Eq. 3.72), we start with the equations

$$
\begin{aligned}
\mathbf{Y}^{(e)}_{jm} &= \frac{1}{\sqrt{j(j+1)}}\overrightarrow{\bigtriangledown} Y_{jm} && (3.76)\\
\mathbf{Y}^{(m)}_{jm} &= \mathbf{n} \times \mathbf{Y}^{(e)}_{jm} && (3.77)
\end{aligned}
$$

where the superscript (e) denotes electric field and (m) the magnetic. Take the example of $j = 1$, $m = 0$, where $Y_{10} \propto \cos\theta = z$. From Eqs. 3.76 and 3.77 we obtain $\mathbf{Y}^{(e)}_{jm} \propto \hat{z}$ and $\mathbf{Y}^{(m)}_{jm} \propto \mathbf{n} \times \hat{z}$. So

$$
\mathbf{e}^* \cdot \mathbf{Y}^{(m)}_{10}(\mathbf{n}) \propto \mathbf{e}^* \cdot \mathbf{n} \times \hat{z} = \mathbf{e}^* \times \mathbf{n} \cdot \hat{z} = \mathbf{h}^* \cdot \hat{z}
$$

This confirms equation 3.73. For photons of $h \parallel n \times z$, $p_l = 0$. For photons of $h \perp n \times z$, $p_l = \sin\theta$, in which θ is the angle between the $\mathbf{n}$ and $\hat{z}$. As shown in Fig. 3.5, in transitions of $m = 0$, the emitted (or absorbed) photons must satisfies $h \perp n \times z$. For such photons of $m = 0$, those moving in direction perpendicular to $\hat{z}$ have the strongest amplitude, while those parallel to $\hat{z}$ have zero probability.

3.1.4 Nuclear Absorption Cross Section

The nuclear absorption cross section for one nucleus can be obtained from optical theorem

$$
\begin{aligned}
\mu_{\text{nuc}} &= \frac{4\pi}{k}\text{Im}\left[f_{nuc}\left(\mathbf{k}_f = \mathbf{k}_i\right)\right] && (3.78)\\
&= \frac{4\pi}{k}\frac{3}{2k(1+\alpha_{\text{IC}})}\text{Im}\left[\frac{1}{z_{10}(\omega) - i}\right] C(\frac{1}{2}1\frac{3}{2}; M_0 m_i)^2 \left|\mathbf{h}\cdot\mathbf{u}_l\right|^2 && (3.79)
\end{aligned}
$$

---

[15] In all formulas involving vector spherical harmonics, the z direction must be chosen to be the quantization direction of the nucleus. By using Eq. 3.73 instead of Eq. 3.72 for the polarization factor, we are free to choose any direction to be the z axis.

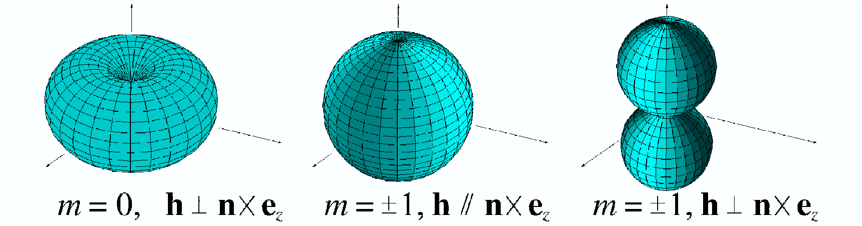

Figure 3.5: Polarization factor in M1 radiation. Each point on the surface represents a propagation direction of the photon, **n**. The distance from the point to the origin represents the amplitude of polarization factor. The change in color indicates the change in the phase of the polarization factor.

Table 3.1: Facts about 6 transitions

l	Transition	C-G Coefficient C_l	ΔM	Polarization Factor p_l	Relative Transition Energy ϵ_l
1	$\frac{1}{2} \to \frac{3}{2}$	1	1	$-\frac{1}{\sqrt{2}}\mathbf{h} \cdot (\mathbf{u}_x + i\mathbf{u}_y)$	$(-\frac{3}{2}\lvert g_1 \rvert - \frac{1}{2}\lvert g_0 \rvert)\mu_N H + IS$
2	$\frac{1}{2} \to \frac{1}{2}$	$\sqrt{\frac{2}{3}}$	0	$\mathbf{h} \cdot \mathbf{u}_z$	$(-\frac{1}{2}\lvert g_1 \rvert - \frac{1}{2}\lvert g_0 \rvert)\mu_N H + IS$
3	$\frac{1}{2} \to -\frac{1}{2}$	$\sqrt{\frac{1}{3}}$	-1	$\frac{1}{\sqrt{2}}\mathbf{h} \cdot (\mathbf{u}_x - i\mathbf{u}_y)$	$(+\frac{1}{2}\lvert g_1 \rvert - \frac{1}{2}\lvert g_0 \rvert)\mu_N H + IS$
4	$-\frac{1}{2} \to \frac{1}{2}$	$\sqrt{\frac{1}{3}}$	1	$-\frac{1}{\sqrt{2}}\mathbf{h} \cdot (\mathbf{u}_x + i\mathbf{u}_y)$	$(-\frac{1}{2}\lvert g_1 \rvert + \frac{1}{2}\lvert g_0 \rvert)\mu_N H + IS$
5	$-\frac{1}{2} \to -\frac{1}{2}$	$\sqrt{\frac{2}{3}}$	0	$\mathbf{h} \cdot \mathbf{u}_z$	$(+\frac{1}{2}\lvert g_1 \rvert + \frac{1}{2}\lvert g_0 \rvert)\mu_N H + IS$
6	$-\frac{1}{2} \to -\frac{3}{2}$	1	-1	$\frac{1}{\sqrt{2}}\mathbf{h} \cdot (\mathbf{u}_x - i\mathbf{u}_y)$	$(+\frac{3}{2}\lvert g_1 \rvert + \frac{1}{2}\lvert g_0 \rvert)\mu_N H + IS$

$$\mu_{\text{nuc}} = \frac{3}{2\pi(1+\alpha_{\text{IC}})} \frac{1}{[z_{10}(\omega)]^2 + 1} C(\frac{1}{2} 1 \frac{3}{2}; M_0 m_i)^2 \left|\mathbf{h} \cdot \mathbf{u}_l\right|^2 \lambda^2 \tag{3.80}$$

In this formula, first we see the absorption cross section is proportional to the square of the wave length of the incident γ-ray. Second, it includes a Lorentz function, which is the line shape of peaks in Mössbauer spectrum. The Clebsch-Gordan coefficients $C(\frac{1}{2}1\frac{3}{2}; M_0 m_i)^2$ and the polarization factor $\left|\mathbf{h} \cdot \mathbf{u}_l\right|^2$ govern the relative strengths of the 6 transitions. Combinations of these two factors give different ratios in a sextet of a Mössbauer spectrum, as shown in Section 2.3 and Table 3.1.

3.2 Scattering Property of a Single Mössbauer Atom

For the electron cloud, the elastic Rayleigh scattering amplitude is

$$f_{\text{ele}} = -r_e f_e [\mathbf{e}_i . \mathbf{e}_f] \tag{3.81}$$

where r_e is the classical electron radius, f_e is a function of scattering angle and is tabulated for each element, and can be found in some books (cf., for example, [20]). The scattering amplitude of an atom is then

$$f = f_{\text{ele}} + f_{\text{nuc}} \tag{3.82}$$

The total differential cross section of scattering is

$$\frac{d\sigma}{d\Omega} = |f|^2 \tag{3.83}$$

3.3 Summary

In summary, Mössbauer diffraction is quite a complex phenomenon, compared to, for example, conventional X-ray diffraction. The Mössbauer scattering amplitude depends not only on the scattering wave vector $\Delta\mathbf{k} = \mathbf{k}_f - \mathbf{k}_i$, and the polarizations of the incident and outgoing photons, but also the magnitude and direction of hyperfine interaction fields on nuclei, the nuclear state sublevels, and the velocity of the Doppler drive (fine-tuning $\hbar\omega$, the photon energy). The complexity could enable various experimental techniques [16] but also make the data reduction difficult.

Different microscopic mechanisms for scattering give rise to different functionalities for X-ray, neutron, electron, and Mössbauer diffractometry, as summarized in Table 3.2. The complementarity of scattering methods has led to the need for the three techniques of X-ray, neutron, and electron diffractometries. Perhaps Mössbauer diffractometry could become a powerful supplementary technique to traditional diffraction techniques.

---

[16] For example, one can study the magnetic structure of iron atoms in a particular chemical environment.

Table 3.2: Comparison of diffraction techniques

X-ray	The oldest but most convenient technique. Most crystal structures are determined by this technique.
Neutron	Usually it is used only when X-ray diffractometry does not work or does not work well. For example, for samples with both heavy and light atoms, X-ray scattering amplitude of low z atoms are so weak that they are unable to be "seen" by the diffractometer, while neutron diffractometry is still usable because it relies on different scattering mechanisms. Actually, neutron scattering cross section of the lightest atom, hydrogen, is very high, and neutron scattering from deuterium is coherent. Neutron magnetic diffraction can also be used to study magnetic long-range order, for example, antiferromagnetism.
Electron	It is very powerful because electron optics are much more practical than for X-rays and neutrons. Electrons can be focused using magnetic lenses. This enables scientists to obtain images of defects: for example, dislocations, interfaces, and even anti-phase boundaries.
Mössbauer	The scattering amplitude is affected by factors such as magnetization directions and chemical environments of Mössbauer atoms. It can study, for example, 1) long-range order of Mössbauer atoms in specific chemical environments and 2) magnetic structures of Mössbauer atoms in specific chemical environments.

Chapter 4

Kinematical Theory of Mössbauer Diffraction

In this chapter we develop the kinematical theory of Mössbauer diffraction. First we find out the scattering property of a Mössbauer atom in a thin, single-crystal sample, in which we take into account averaging of scattering intensities owing to isotope enrichment, thermal fluctuation, and distribution of hyperfine interactions. Next we go further by investigating the scattering property of a thin layer of a polycrystalline sample, which is the only kind of sample we are studying now. Average due to orientational distribution of hyperfine magnetic field among crystallites is worked out. Then we deduce the diffraction intensity from a polycrystalline sample. A prototype application of the formalisms developed in this chapter is presented with diffraction data of a polycrystalline ^{57}Fe sample.

Dynamical theory of diffraction is generally needed for Mössbauer optics. An outline of dynamical Mössbauer diffraction theory is presented in Section 4.6. A method to justify the applicablity of kinematical theory in the Mössbauer diffraction of polycrystalline sample is presented in Section 4.7.

It is convenient to define the geometry of scattering here in Fig. 4.1.

4.1 Scattering Property of A Mössbauer Atom in a Thin Single-Crystal Sample

Only for a very thin sample, the single-scattering approximation can be used for Mössbauer diffraction[1]. In such an approximation, the scattering amplitude of a collection of atoms would be the superposition of the scattering amplitudes of all atoms. In the previous chapter, we see that the scattering amplitude from a Mössbauer nucleus depends on not only the photon energy, but the

---

[1] Otherwise the dynamical diffraction will be too strong.

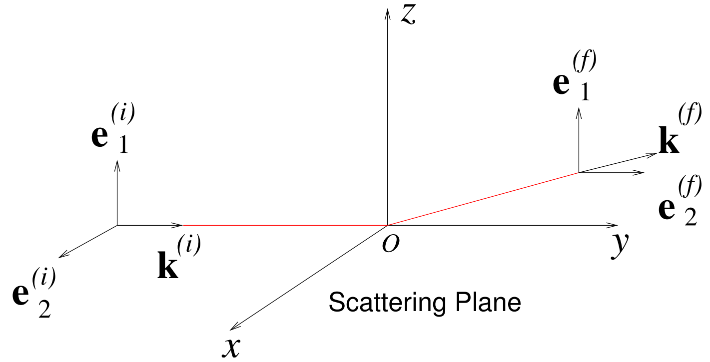

Figure 4.1: Scattering geometry. The indexes i and f indicate the incident and outgoing photons, respectively. Scattering is assumed to happen in the xy plane. The incident wave propagates in the y direction. The polarization of index 1 is always parallel to the z direction, while that of index 2 is always perpendicular to the z direction.

photon polarization, and the electromagnetic field exerted on the nucleus. The scattering amplitude for an atom is therefore

$$f = f(\mathbf{r}, \omega, \nu, \psi(0), \mathbf{H}_{\text{hf}}, \nabla\mathbf{E}_{hf}, \ldots) \tag{4.1}$$

where $\mathbf{r}$ is its position, ω is the incident γ-ray energy, ν indicates the polarization state of the photon, $\psi(0)$ is the electron wavefunction at the nucleus, $\mathbf{H}_{\text{hf}}$ is the hyperfine magnetic field, $\nabla\mathbf{E}_{\text{hf}}$ is the gradient of the hyperfine electric field. For simplicity, we just drop all parameters except $\mathbf{r}$ (we will put them back whenever necessary):

$$f = f(\mathbf{r}) \tag{4.2}$$

The total differential cross section of scattering from a sample composed of many atoms is then

$$\frac{d\sigma}{d\Omega} = \left| \sum_i f(\mathbf{r}_i) e^{i\mathbf{k}\cdot\mathbf{r}_i} \right|^2 \tag{4.3}$$

This looks quite familiar. Actually every kinematical diffraction theory would have a formalism like this one. Similar to the nomenclature used in neutron diffraction[2], we can define coherent and incoherent scattering cross sections. For a thin sample of a Bravais lattice of N atoms of same

---

[2] Please cf, for example, reference [40].

species, we have

$$\left[\frac{d\sigma}{d\Omega}\right]_{\text{coh}} = \frac{N(2\pi)^3}{V}\left|\overline{f}\right|^2 \sum_{\mathbf{G}} \delta(\mathbf{k}-\mathbf{G}) \tag{4.4}$$

$$\left[\frac{d\sigma}{d\Omega}\right]_{\text{incoh}} = N\left(\overline{|f^2|} - \left|\overline{f}\right|^2\right) \tag{4.5}$$

where V is the volume of the crystal. The reciprocal lattice vector is $\mathbf{G}$, and the scattering wave vector is $\mathbf{k} = \mathbf{k}_f - \mathbf{k}_i$. The Dirac delta function, $\delta(\mathbf{k}-\mathbf{G})$, signifies the Bragg diffraction condition.[3] The averaging of scattering amplitude, $\bar{f}$, should be taken over all variables that apply for the system we are investigating[4].

For this dissertation, we are focused on the coherent scattering. We need to first calculate the averaged nuclear scattering amplitude of a Mössbauer nucleus, by taking into account thermal fluctuation and isotope enrichment,

$$\bar{f}_{\text{nuc}} = \eta f_{\text{ML}} f_{\text{nuc}} \tag{4.6}$$

The enrichment of Mössbauer nucleus is η , and the thermal fluctuation of atom positions is taken into account by including the Mössbauer-Lamb factor, f_{ML}.

Another average may occur due to distribution of hyperfine interactions

$$\bar{f}_{\text{nuc}} = \eta f_{\text{ML}} \left\langle f_{\text{nuc}} \right\rangle_{\text{HI}} \tag{4.7}$$

where $\langle\rangle_{\text{HI}}$ denotes the average over distribution of hyperfine interactions. This average depends on the nature of the hyperfine interactions. In the next Section, we will focus on how hyperfine magnetic field distribution can affect the scattering amplitudes of ^{57}Fe atoms.

---

[3] Since

$$\frac{N(2\pi)^3}{V}\sum_{\mathbf{G}} \delta(\mathbf{k}-\mathbf{G})$$

in Eq. 4.4 is a common factor, it will be ignored from now on. Remember to put it back when necessary!

[4] For example, in a sample composed of $(1-\eta)$ ^{56}Fe atoms and η ^{57}Fe atoms, only ^{57}Fe nuclei contribute to the nuclear resonant scattering. One can easily obtain the average nuclear resonant scattering amplitude as: $\bar{f}_{\text{nuc}} = \eta f_{\text{nuc}} + (1-\eta) \times 0 = \eta f_{\text{nuc}}$.

4.2 Effects of Hyperfine Magnetic Field Distribution on Scattering Amplitudes of ^{57}Fe Atoms

For ^{57}Fe, the nuclear scattering amplitude is

$$\bar{f}_{\mathrm{nuc}} = \frac{3\eta f_{\mathrm{ML}}}{4k(1+\alpha_{\mathrm{IC}})} \sum_l \frac{p^*_{l;i} p_{l;f}}{z_l(v) - i} C_l^2 \tag{4.8}$$

where

$$z_l(v) = \frac{2}{c\Gamma_1/E_{10}} (\epsilon_l - v) \,. \tag{4.9}$$

The scattering amplitude $\bar{f}_{\mathrm{nuc}}$ implicitly depends on the magnitude and direction of hyperfine fields through factors $z_l(v)$ and $p^*_{l;i} p_{l;f}$. This formula is obtained from Eq. 3.71. However, one must notice that the sum over m, the photon angular momentum, in Eq. 3.71 is changed to the sum over l, the index of all possible transitions here. As a result, a factor $\frac{1}{2I_0+1} = \frac{1}{2}$ is inserted. This factor of $\frac{1}{2I_0+1}$ arises from the even distribution of the nuclear states in $(2I_0 + 1)$ sublevels of the ground state of a nucleus, which, in turn, is due to the fact that the energy differences of these hyperfine sublevels are much smaller than thermal energy kT in room temperature.

Equation 4.9 gives the normalized energy shift in a form different from Eq. 3.66. Here ϵ_l is the relative transition energy with the unit of velocity, v is the Doppler drive velocity, c is the speed of light in vacuum, and $E_{10} = E_1 - E_0$ is the energy difference between first excited state and ground state (for ^{57}Fe, $E_{10} = 14.4$ keV).

The values of the Clebsch-Gordan coefficients C_l, the polarization factor p_l, and the relative transition energy ϵ_l can be found in Table 3.1.

The nuclear scattering amplitude of ^{57}Fe atoms in a sample with a HMF distribution in both the magnitudes and the orientations is then

$$\bar{f}_{\mathrm{nuc}} = \frac{3\eta f_{\mathrm{ML}}}{4k(1+\alpha_{\mathrm{IC}})} \sum_l C_l^2 \left\langle \frac{p^*_{l;i} p_{l;f}}{z_l(\omega) - i} \right\rangle_{\mathrm{HMF}} \tag{4.10}$$

where $\langle\rangle_{\mathrm{HMF}}$ denotes the average over distribution of hyperfine magnetic fields.

The electronic part of scattering amplitude is independent of the hyperfine distributions,

$$\bar{f}_{\mathrm{ele}} = f_{\mathrm{ele}} \tag{4.11}$$

And the total scattering form factor of an atom is then

$$\bar{f} = \bar{f}_{\text{ele}} + \bar{f}_{\text{nuc}} \tag{4.12}$$

Let us now look at two relatively simple examples, one for pure magnitude distribution of HMF, another for pure orientational distribution of HMF.

4.2.1 Example 1: Distribution of Magnitudes of HMF

Suppose a pure ^{57}Fe sample is put into an external magnetic field to make sure hyperfine magnetic fields of all nuclei are aligned to one direction. Only the magnitude of the HMF has a Gaussian distribution centered in 330kG. Then the coherent scattering cross section is

$$\begin{aligned} \left|\bar{f}\right|^2 &= \left|f_{\text{ele}} + \int dH \rho(H) \bar{f}_{\text{nuc}}(H)\right|^2 \\ \rho(H) &= g\left(\frac{H - H_0}{\Delta H}\right) \end{aligned}$$

where $g(x)$ is the normalized Gaussian function

$$g(x) = \frac{1}{\sqrt{\pi}} \exp(-x^2)\,,$$

H is the magnitude of the hyperfine magnetic field, $H_0 = 330\text{kG}$, and $\bar{f}_{\text{nuc}}(H)$ is given by Eq. 4.8. This might be the simplest scenario we can think of.

4.2.2 Example 2: Orientational Distribution of HMF

Another interesting example is the case where the magnitude of the hyperfine magnitude is all the same, but there is a distribution of direction hyperfine magnetic fields in the crystal.

It is convenient to separate out the polarization factor by defining

$$\bar{f}^0_{\text{nuc};l} = \frac{3\eta f_{\text{ML}}}{4k(1+\alpha_{\text{IC}})} \frac{1}{z_l(\omega) - i} C_l^2 \tag{4.13}$$

$$P_{l;f\leftarrow i} = p^*_{l;i} p_{l;f} \tag{4.14}$$

Then we have

$$\bar{f}_{\text{nuc}} = \sum_l \bar{f}^0_{\text{nuc};l} P_{l;f\leftarrow i} \tag{4.15}$$

The coherent scattering cross section

$$\left|\overline{f}\right|^2 = \left|f_{\text{ele}} + \int d\Omega \rho(\mathbf{n}) \bar{f}_{\text{nuc}}(\mathbf{n})\right|^2$$

where $\rho(\mathbf{n})$ is the orientational distribution function of HMF. The integral will be evaluated in Appendix B. Here we only present results. If we expand $\rho(\mathbf{n})$ as

$$\rho(\mathbf{n}) = \sum_{\lambda\mu} a^{\lambda\mu} Y_{\lambda\mu}(\mathbf{n}) \tag{4.16}$$

then

$$\left[\frac{d\sigma}{d\Omega}\right]_{\text{coh}}^{n_i n_f} = \left|f_{\text{ele}} + \sum_l \bar{f}^0_{\text{nuc};l} \sum_{\lambda\mu} a^{\lambda\mu} \overline{P}^{n_i n_f M_l}_{\lambda\mu;\text{nuc}}\right|^2$$

where $\overline{P}^{n_i n_f M_l}_{\lambda\mu;\text{nuc}}$ is an average polarization factor (Eq. 4.29), and can be easily calculated by a Mathematica code presented in appendix B.5. The polarizations of incident and outgoing photons are denoted by n_i and n_f, respectively.

A special case: spherical distribution of HMF

In this case $\lambda = 0$, where λ is the spherical harmonic expansion order in Eq. 4.16. So

$$\overline{P}^{n_i n_f M}_{00;\text{nuc}} = \frac{1}{3}\delta_{n_i,n_f}(\delta_{n_i,1}\cos(2\theta) + \delta_{n_i,2}) \tag{4.17}$$

In this case, if the scattering angle $2\theta = \pi/2$, photons with polarization perpendicular to the scattering plane are not scattered by ^{57}Fe nuclei. The coherent cross section would be

$$\left[\frac{d\sigma}{d\Omega}\right]_{\text{coh}}^{n_i n_f} = \left|f_{\text{ele}} + \sum_l \bar{f}^0_{\text{nuc};l} \overline{P}^{n_i n_f M_l}_{00;\text{nuc}}\right|^2 .$$

Our samples (up to now) are usually ferromagnetic, however. This means that the magnetization of atoms in one crystallite are all aligned. Nevertheless, there could be some cases in which the hyperfine magnetic fields are not all parallel to each other. Here we take the Invar alloy as an example.

4.2.3 Possible Application for Studying Invar

Let us focus on a special type of measurement.[5] Suppose we tune the incident photon energy to the resonant energy of some ^{57}Fe nuclei. Then for a first-order approximation, we can ignore the contributions from all other nuclei that are not on resonance, and also those from electrons, and the only contribution is from those nuclei on resonance. The scattering cross section for these nuclei is

$$\bar{f}_{\text{nuc}} = \sum_l \bar{f}^0_{\text{nuc};l} P_{l;f\leftarrow i}$$

where $\bar{f}^0_{\text{nuc};l}$ is a constant, and the polarization factor takes the usual form

$$\begin{aligned} P_{l;f\leftarrow i} &= p^*_{l;i} p_{l;f} \\ p_l &= (\mathbf{h}\cdot\mathbf{u}_l) \end{aligned} \tag{4.18}$$

For transitions $l = 2$ and 5 (for which $M = 0$, $\mathbf{u}_l = \mathbf{u}_z$), a nucleus with HMF$\|$ z (i.e. $\mathbf{u}_z = \mathbf{z}$) cannot scatter photons with polarization $\mathbf{h} \perp \mathbf{z}$ (because $p_l = \mathbf{h}\cdot\mathbf{u}_z = 0$). However, a nucleus with a HMF that has components in the xy plane (i.e., $\mathbf{u}_z \cdot (\mathbf{u}_x \pm i\mathbf{u}_y) \neq 0$) can scatter photons with polarization $h \perp z$. Therefore, a polarized beam of incident photons could be used to detect the orientational distribution of the magnetic moments of Fe atoms, because the direction of the HMF at its nucleus is directly related to the direction of the magnetic moment of an Fe atom.

Controversy about Invar INVAR was discovered in late 19th century[27]. For general reading about INVAR, please refer to, e.g., [48]. The controversy is about the origin of the zero expansion coefficients. A famous model proposed by Weiss[65] assumes that there are two competing magnetic states for Fe atoms in the alloy: one with high magnetic moment (HS) and bigger volume, another with low magnetic moment (LS) and smaller volume (2γ-state model). When the alloy is heated, the LS become more stable and dominant, which could result in a "shrinking" of the material. This contraction could compensate the normal thermal expansion and explain the "INVAR" effect. However, there are several experimental results contradictory to the 2γ-state model.[6] Recent advances in calculation techniques have renewed interests in theories of Invar alloys. Schilfgaarde and colleagues[64] proposed that the magnetic transition in Invar alloy is a continuous transition from

---

[5] This Section could be in the chapter for Future Works. However, since it needs a little more development of the kinematical diffraction theory, I found it appropriate to put it here.

[6] For example, the transition from the HS state to the LS state as a function of concentration should be of first order, but experiments show that it is a second-order transition.

a collinear, low-temperature magnetic state to a more-or-less uniform distributed (non-collinear), high-temperature magnetic state. If we assign z-axis to the direction of the collinear magnetization, then a non-collinear magnetic state associates itself with the presence of magnetic moments with components in xy plane. Thus, as already pointed out previously, this transformation of magnetic states could be determined by Mössbauer diffraction, if only we can polarize the incident photons.

To show why Mössbauer diffraction is a powerful technique to study magnetic structure, we can compare it to neutron diffraction. The neutron scattering amplitude of a single nucleus is

$$\widehat{b} = A + B\widehat{\sigma} \cdot \widehat{S} \tag{4.19}$$

where $\widehat{\sigma}$, $\widehat{S}$ is the spin of the neutron and the atom, respectively, and A and B are constants. Compare this equation to Eq. 4.18, we find that: while in Eq. 4.19 $\widehat{\sigma}$ carries the information about the polarization of the incident neutron and $\widehat{S}$ carries the information about the orientation of the atomic spin, in Eq. 4.18 $\mathbf{h}$ is the polarization of the incident photon and $\mathbf{u}_z$ is the direction of the HMF (which is anti-parallel to the atomic magnetic moment). Therefore, we should be able to study magnetic structure by using Mössbauer diffractometry. Furthermore, Mössbauer diffraction has one more degree of freedom: it can discern Fe atoms with different magnitude of magnetic moment by fine-tuning the energy of incident photons. For the problem of INVAR, if there exist two magnetic states, we can study them separately by tuning the Doppler velocity.

4.2.4 Summary

There are even more complex scenarios. For example, both the magnitude and the orientation of HMF have variations within the crystal. In those cases, a brute-force approach (assume a form of HMF distribution and do numerical integration using Eq. 4.10) might be necessary.

4.3 Diffraction Intensity of a Polycrystalline Sample: Effects of Orientational Distribution of Hyperfine Magnetic Fields among Crystallites

A polycrystalline sample is composed of many small crystallites. Inside each crystallite, photons are scattered by nuclei and electrons, and the scattering amplitudes and cross sections can be readily evaluated by using formalisms developed in the previous Sections. The scattering properties of a polycrystalline sample should be obtained by appropriate summation of contributions from all crystallites[7]. The sum is incoherent because the random distribution of crystallites results in a loss of phase information. Thus, the scattering cross section of a thin layer of a polycrystalline sample is

$$\left[\frac{d\sigma}{d\Omega}\right]_{\text{poly}} = \left\langle \left[\frac{d\sigma}{d\Omega}\right]_{\text{crys}} \right\rangle$$

while the average is over all crystallites in the layer, and $\left[\frac{d\sigma}{d\Omega}\right]_{\text{crys}}$ is given by Eq. 4.7.

A complexity of the polycrystalline average is that each crystallite has its own magnetization direction. This means that magnetic moments in each crystallite are collinear, but the magnetization directions of different crystallites are not necessarily parallel to each other. The overall cross section for a polycrystalline sample must take this into account, as is done in the present Section.

4.3.1 Scattering Cross Section

If we have a polycrystalline sample that is not magnetized in a certain direction, we may suppose that there is an orientation distribution of the hyperfine magnetic fields in the sample, described by function $\rho(\mathbf{u}_z)$. Then the averaged cross section is

$$\begin{aligned}
\frac{d\sigma}{d\Omega} &= \int d\mathbf{R}\rho(\mathbf{R}\mathbf{u}_z^o)\mathbf{P}_R\,|f|^2 \\
&= \int d\mathbf{R}\rho(\mathbf{R}\mathbf{u}_z^o)\mathbf{P}_R\,|f_{\text{nuc}} + f_{\text{ele}}|^2 \\
&= \int d\mathbf{R}\rho(\mathbf{R}\mathbf{u}_z^o)\mathbf{P}_R\left\{\ |f_{\text{nuc}}|^2 + |f_{\text{ele}}|^2 + f_{\text{nuc}}^* f_{\text{ele}} + f_{\text{nuc}} f_{\text{ele}}^*\ \right\} \\
&= \left[\frac{d\sigma}{d\Omega}\right]_{\text{nuc}} + \left[\frac{d\sigma}{d\Omega}\right]_{\text{ele}} + \left[\frac{d\sigma}{d\Omega}\right]_{\text{int}} \qquad (4.20)
\end{aligned}$$

where $\rho(\mathbf{u}_z)$ is the orientational distribution function of the hyperfine magnetic field, $\mathbf{u}_z$ is the unit vector in the direction of the hyperfine magnetic field. $\rho(\mathbf{u}_z)d\Omega_{\mathbf{u}_z}$ is the probability that the direction of the hyperfine magnetic field is in the solid angle $d\Omega_{\mathbf{u}_z}$. The original direction of the HMF is $\mathbf{u}_z^o$.[8]

It should be pointed out here that the orientational distribution of HMF here is different from the one in Section 4.2.2. The distribution here exists among crystallites, while the distribution in Section 4.2.2 exists inside a crystallite. Therefore, the average scattering cross section will take a different form from that in Section 4.2.2.

---

[7] more precisely, all crystallites that are in Bragg condition and that deviate from Bragg condition slightly. See for example, Section 1.5.1 in Ref. [20].

[8] It can be selected arbitrarily, but one direction must be chosen as the original direction, and then a rotation can bring this original unit vector to any direction inside the whole 4π solid-angle. If a different direction is chosen as the original direction, the function $\rho(\mathbf{u}_z)$ will also transform to a new form.

To evaluate the averaged cross section, again, we could expand the distribution function with spherical harmonics

$$\rho(\mathbf{u}_z) = \sum_{\lambda\mu} a^{\lambda\mu} Y_{\lambda\mu}(\mathbf{u}_z)\,. \tag{4.21}$$

It is found that only spherical harmonics of order $l \leq 4$ have contributions, and the results are as follows[9]:

The differential cross section for pure nuclear scattering is

$$\left[\frac{d\sigma}{d\Omega}\right]^{n_i n_f}_{\text{nuc}} = \sum_{m,M,m',M'} f^0_{\text{nuc}}(m,M)\left[f^0_{\text{nuc}}(m',M')\right]^* \overline{P^2}^{n_i n_f MM'}_{\text{nuc}} \tag{4.22}$$

where

$$\overline{P^2}^{n_i n_f MM'}_{\text{nuc}} = \sum_{\lambda\mu} a^{\lambda\mu} \overline{P^2}^{n_i n_f MM'}_{\lambda\mu;\text{nuc}} \tag{4.23}$$

$$\begin{aligned}\overline{P^2}^{n_i n_f MM'}_{\lambda\mu;\text{nuc}} = {} & \frac{1}{4}\sqrt{\frac{2\lambda+1}{4\pi}} \sum_{m_i,m_i',m_f,m_f'} J^\lambda_\mu(m_i,m_f,m_i',m_f',M,M') \\ & \times \left[\delta_{1m_i} + (-1)^{n_i-1}\delta_{-1,m_i}\right]\left[\delta_{1m_i'} + (-1)^{n_i-1}\delta_{-1,m_i'}\right] \\ & \times \left[D^1_{1m_f}(\frac{\pi}{2},2\theta,-\frac{\pi}{2}) + (-1)^{n_f-1}D^1_{-1,m_f}(\frac{\pi}{2},2\theta,-\frac{\pi}{2})\right] \\ & \times \left[D^1_{1m_f'}(\frac{\pi}{2},2\theta,-\frac{\pi}{2}) + (-1)^{n_f-1}D^1_{-1,m_f'}(\frac{\pi}{2},2\theta,-\frac{\pi}{2})\right]^*\end{aligned} \tag{4.24}$$

Here, the rotation matrices $D^l_{m'm}$ are those defined by Rose [46] and J^λ_μ is defined in Eq. B.10. The photon polarizations are indexed by n_i and n_f.

With formalisms here, we can easily obtain the averaged polarization factors and then the coherent scattering cross sections, if we have the expansion coefficients, $a^{\lambda\mu}$.

The differential cross section for pure electronic scattering is

$$\left[\frac{d\sigma}{d\Omega}\right]_{\text{ele}} = \left|f^0_{\text{ele}} P_{\text{ele}}\right|^2 \tag{4.25}$$

where

$$P_{\text{ele}} = -\delta_{n_i,n_f}(\delta_{n_i,1} + \delta_{n_i,2}\cos(2\theta)) \tag{4.26}$$

---

[9] Detailed derivations are presented in Appendix B.

The differential cross section for the interference between nuclear and electronic scattering is

$$\left[\frac{d\sigma}{d\Omega}\right]^{n_i n_f}_{\text{int}} = 2\text{Re}\left[\sum_{m,M}\left(f^0_{\text{ele}}\right)^* P^*_{\text{ele}} f^0_{\text{nuc}} \overline{P}^{n_i n_f M}_{\text{nuc}}\right] \tag{4.27}$$

where

$$\overline{P}^{n_i n_f M}_{\text{nuc}} = \sum_{\lambda\mu} a^{\lambda\mu} \overline{P}^{n_i n_f M}_{\lambda\mu;\text{nuc}} \tag{4.28}$$

$$\begin{aligned}\overline{P}^{n_i n_f M}_{\lambda\mu;\text{nuc}} &= \frac{1}{6}\sqrt{\frac{2\lambda+1}{4\pi}} \sum_{m_i,m_f} C^{1,\lambda,1}_{m_f,\mu,m_i} C^{1,\lambda,1}_{M,0,M} [\delta_{1m_i} + (-1)^{n_i-1}\delta_{-1,m_i}] \\ &\times \left[D^1_{1m_f}(\frac{\pi}{2}, 2\theta, -\frac{\pi}{2}) + (-1)^{n_f-1} D^1_{-1m_f}(\frac{\pi}{2}, 2\theta, -\frac{\pi}{2})\right]^*\end{aligned} \tag{4.29}$$

4.3.2 Absorption Cross Section

The optical theorem gives the relation between the absorption cross section and the imaginary part of the scattering amplitude

$$\mu = \frac{4\pi}{k}\text{Im} f(\mathbf{k}_f = \mathbf{k}_i) \tag{4.30}$$

Nuclear Cross Section The averaged nuclear absorption cross section is then[10]

$$\begin{aligned}\bar{\mu}^{n_i}_{\text{nuc}} &= \frac{4\pi}{k}\text{Im} f^{n_i}_{\text{nuc}}(\mathbf{k}_f = \mathbf{k}_i) \\ &= \frac{4\pi}{k}\text{Im}\left[\sum_{l,n_f} f^0_{\text{nuc}}(\mathbf{k}_f = \mathbf{k}_i) \overline{P}^{n_i n_f M_l}_{\text{nuc}}(\mathbf{k}_f = \mathbf{k}_i)\right] \qquad (4.31) \\ &= \sum_{l,n_f} \frac{3\pi}{k^2(1+\alpha_{\text{IC}})} \eta f_{\text{ML}} C^2_l \frac{1}{1+z_l(\omega)^2} \overline{P}^{n_i n_f M_l}_{\text{nuc}}(\mathbf{k}_f = \mathbf{k}_i) \qquad (4.32)\end{aligned}$$

This derivation used the fact that the averaged polarization factor for forward scattering, $\overline{P}^{n_i n_f M_l}_{\text{nuc}}(\mathbf{k}_f = \mathbf{k}_i)$, is always real.

Define

$$\begin{aligned}\mu^l_{\text{nuc}} &= \frac{4\pi}{k}\text{Im} f^0_{\text{nuc}}(\mathbf{k}_f = \mathbf{k}_i) \qquad (4.33) \\ &= \frac{3\pi}{k^2(1+\alpha_{\text{IC}})} \eta f_{\text{ML}} C^2_l \frac{1}{1+z_l(\omega)^2} \qquad (4.34)\end{aligned}$$

---

[10] As expected, the average nuclear absorption cross section due to orientational distribution of HMF takes the same form for both the case here (orientational distribution exists among crystallites) and the case in Section 4.2.2 (orientational distribution exists inside each crystallite).

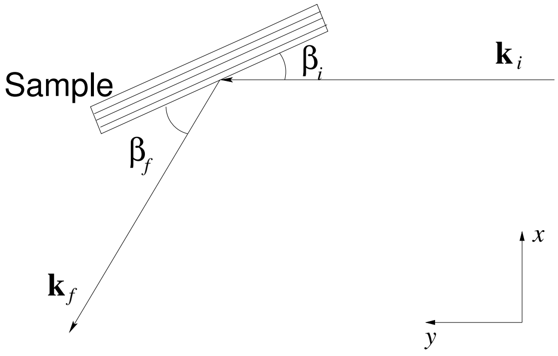

Figure 4.2: Scattering from a polycrystalline sample

Then

$$\bar{\mu}_{\text{nuc}}^{n_i} = \sum_{l,n_f} \overline{P}_{\text{nuc}}^{n_i n_f M_l} \mu_{\text{nuc}}^{l} \tag{4.35}$$

The major contribution to the electronic cross section, μ_{ele} is from the photoelectronic process:

$$\mu_{\text{ele}} = \mu_{\text{pe}}$$

The total cross section, $\bar{\mu}^{n_i}$, is the sum of the nuclear and the electronic parts:

$$\bar{\mu}^{n_i} = \bar{\mu}_{\text{nuc}}^{n_i} + \mu_{\text{ele}} \tag{4.36}$$

4.3.3 Samples with More Than One Atom in a Unit Cell

The previous discussion concerned samples with only one atom per unit cell. Nevertheless, it is easy to extend the theory outlined above to include more general cases. In a crystalline sample with multiple atoms per unit cell, the scattering amplitude $f(\mathbf{r}_i)$ in Eq. 4.3 should be replaced by the scattering amplitude of a unit cell

$$f_{\text{uc}} = \sum_{\nu} f^{\nu} \exp(i\mathbf{k} \cdot \mathbf{r}^{\nu}) \tag{4.37}$$

where $\mathbf{r}^{\nu}$ is the relative position of atom ν in the unit cell and f^{ν} its scattering amplitude.

4.4 Diffraction Intensity from a Polycrystalline Sample

The notation of Bara, developed for conventional backscatter Mössbauer spectra,[5] can be extended conveniently for the present case of diffraction. Some geometrical variables are defined in Fig. 4.2. For diffraction we consider Bara's term for coherent elastic scattering:

$$I^{n_f}(\mathbf{k}_i, \mathbf{k}_f, E, x) = \xi_D \int_0^t dx R^{n_f}(\mathbf{k}_i, \mathbf{k}_f, E, x), \tag{4.38}$$

where

$$\begin{aligned} R^{n_f}(\mathbf{k}_i, \mathbf{k}_f, E, x) \quad &= \quad \sum_{n_i} U^{n_i}(E) \exp\left\{-x\bar{\mu}^{n_i}(\mathbf{k}_i, E) \csc\beta_i\right\} \\ &\times \left[\frac{d\bar{\sigma}}{d\Omega}\right]^{n_i n_f}_{\text{coh}} (\mathbf{k}_i, \mathbf{k}_f, E) \exp\left\{-x\bar{\mu}^{n_f}(\mathbf{k}_f, E) \csc\beta_f\right\}. \end{aligned} \tag{4.39}$$

Equation (4.39) includes factors for the spectrum of incident photons, $U(E)$, for the attenuation by recoilless and non-recoilless scattering as the photons penetrate into the sample to depth x, $\exp\{-x\bar{\mu}_i \csc\beta_i\}$, the elastic scattering cross section, $\left[\frac{d\bar{\sigma}}{d\Omega}\right]^{n_i n_f}_{\text{coh}}$, and a second exponential factor for attenuation as the scattered photons traverse the sample on the way out. Note that the the scattering cross section $\left[\frac{d\bar{\sigma}}{d\Omega}\right]^{n_i n_f}_{\text{coh}}$ depends on the incident and outgoing wavevectors, $\mathbf{k}_i$ and $\mathbf{k}_f$, whereas the absorption cross section $\bar{\mu}^n$, depends on only one of them. Here n specifies the polarization state of the photon. The sample thickness is denoted by t. A constant, ξ_D, accounts for all other factors being left out, such as the detector efficiency for 14.4 keV photons.

4.5 Application to a ^{57}Fe Polycrystalline Sample

A detailed description of this experiment can be found in [39, 35]. An outline will be given here. This experiment and its analysis show

1. how we can obtain diffraction intensities from the formalisms developed in this chapter;
2. the important roles of the polarization factors;
3. the effects of wave interference between nuclear and electronic scattering.

Mössbauer diffraction patterns from a polycrystalline, enriched ^{57}Fe sample were taken at 6 resonant energies for two conditions: one with external magnetic field applied in the direction perpendicular to the scattering plane (In field), and another without an applied magnetic field (No field). The intensities of diffraction peaks (222) and (332) were collected to study their energy dependence. The experimental results were compared to calculations.

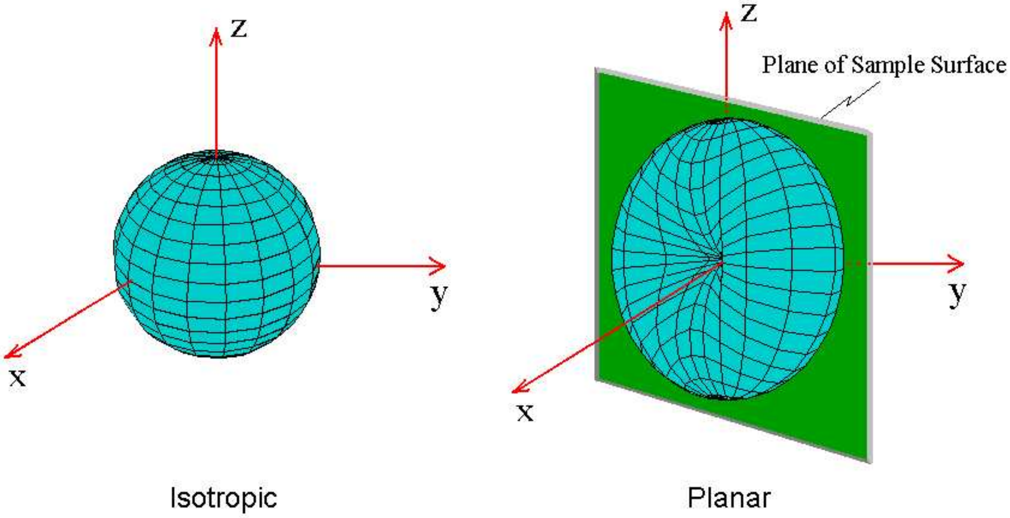

Figure 4.3: Orientational HMF distribution: isotropic and anisotropic

The basic calculation procedure was:

1. calculate the polarization factors (Section 4.3 and Appendix B);

2. substitute the polarization factors into Eqs. 4.20 and 4.36 to evaluate the averaged scattering and absorption cross section;

3. substitute the cross sections into Eq. 4.38 to calculate the diffraction intensity.

For calculating average polarization factors for the "No-field" experiment, we simulate the HMF distribution using two models: the isotropic (spherical) distribution[11], and an anisotropic distribution[12], as shown in Fig. 4.3.

Before we do real calculations, some further simplification can be done for the case of ferromagnetic iron. Because the spacings between the six resonance peaks for ferromagnetic iron are big compared to their width, the interference between different nuclear transitions is small. Therefore, Eq. 4.22 is reduced to

$$\left[\frac{d\sigma}{d\Omega}\right]^{n_i n_f}_{\text{nuc}} = \sum_{m,M} f^0_{\text{nuc}}(m,M)\left[f^0_{\text{nuc}}(m,M)\right]^* \overline{P^2}^{n_i n_f MM}_{\text{nuc}} \tag{4.40}$$

---

[11] for which some of the averaged polarization factors $\overline{P^2}$ have been evaluated by Nakai, et al.[42]

[12] The hyperfine magnetic fields are assumed to be mostly lying in the plane of sample:

$$\rho(\mathbf{u}_z) = \frac{3}{2}\left(1 - (\mathbf{u}_z.\hat{n}_S)^2\right)$$

where $\hat{n}_S$ is the normal of the sample surface.

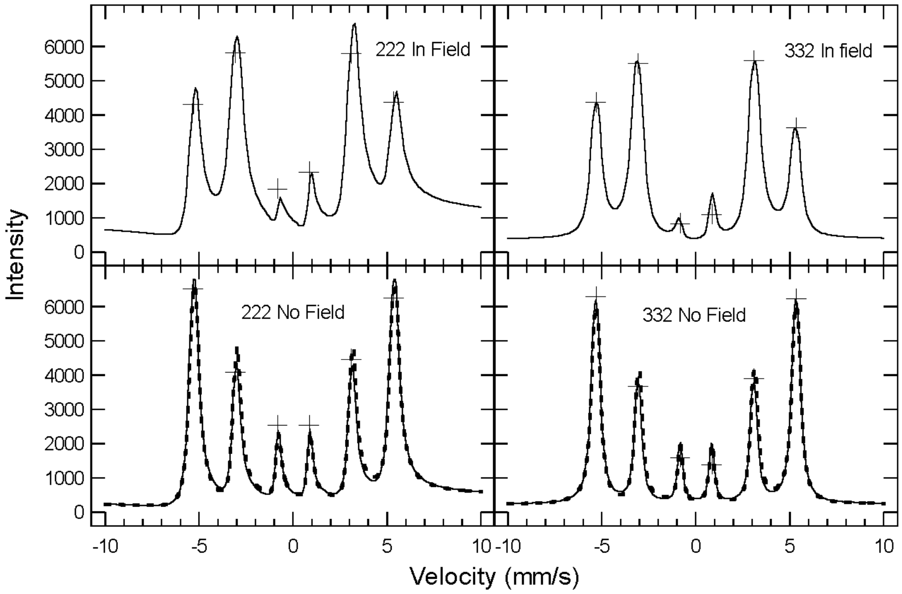

Figure 4.4: Calculated intensities for (222) and (332) Mössbauer diffractions from bcc ^{57}Fe. Crosses: experimental data. Solid lines: calculated from the isotropic model of HMF orientations. Dashed lines: calculated from the anisotropic model.

in which only terms of $M = M'$ are preserved. Table 4.1 gives all relevant average polarization factors for this case.

Results from these calculations of intensities are presented in Fig. 4.4, together with experimental data. To understand these results in a more qualitative way, we first notice that when the sample is two or three times thicker than the extinction length, the scattering intensity can be approximated as

$$I \propto \frac{d\sigma/d\Omega}{\mu} \ . \tag{4.41}$$

When the source is tuned to a nuclear resonance, we can ignore the Rayleigh scattering and interference in our approximation, so we have $\frac{d\sigma}{d\Omega} \propto \overline{P2}_{\text{nuc}}$ and $\mu \propto \overline{P}_{\text{nuc}}(2\theta = 0)$. The scattering intensity therefore can be estimated by

$$I \propto \frac{\overline{P2}_{\text{nuc}}}{\overline{P}_{\text{nuc}}(2\theta = 0)} \ . \tag{4.42}$$

From Fig. 3.5 we see that, for the $l = 2, 5$ transition for which $M = 0$, the polarization factor is zero when $\mathbf{k}$ is parallel to $\hat{z}$. In a uniaxial HMF, no $M = 0$ photons travel along the $\hat{z}$ direction, and the diffracted intensity in the plane of scattering (which is perpendicular to the direction $\hat{z}$) is

Table 4.1: Polarization factors, $\overline{P^2}$ and $\overline{P}$, for Mössbauer scattering averaged over the three HMF distributions. The photon angular momentum in the z direction is M, and the photon polarization indexes are n_i and n_f. The diffraction angle is denoted by 2θ, and angles β_i and β_f are defined in Fig. 4.2.

M	n_i/n_f	Averaged Polarization Factor $\overline{P^2}^{n_i n_f M M}$		
		Uniaxial	Isotropic	Planar Bias
±1	1/1	0	$\frac{1}{10}+\frac{1}{30}\cos^2(2\theta)$	$\frac{1}{70}(9+\cos(2\beta_i)+\cos(2\,2\theta)+\cos(2(\beta_i-2\theta)))$
	1/2	0	$\frac{1}{10}$	$\frac{1}{140}(13+3\cos(2\beta_i))$
	2/1	0	$\frac{1}{10}$	$\frac{1}{140}(13+3\cos(2(\beta_i-2\theta)))$
	2/2	$\frac{1}{4}$	$\frac{2}{15}$	$\frac{4}{35}$
0	1/1	1	$\frac{1}{15}+\frac{2}{15}\cos^2(2\theta)$	$\frac{1}{70}(8-3\cos(2\beta_i)+4\cos(2\,2\theta)-3\cos(2(\beta_i-2\theta)))$
	1/2	0	$\frac{1}{15}$	$\frac{1}{70}(5-\cos(2\beta_i))$
	2/1	0	$\frac{1}{15}$	$\frac{1}{70}(5-\cos(2(\beta_i-2\theta)))$
	2/2	0	$\frac{1}{5}$	$\frac{9}{35}$
M	n_i/n_f	Averaged Polarization Factor $\overline{P}^{n_i n_f M}$		
		Uniaxial	Isotropic	Planar Bias
±1	1/1	0	$\frac{1}{3}\cos(2\theta)$	$\frac{1}{20}(7\cos(2\theta)+\cos(2\beta_i-2\theta))$
	1/2	0	0	0
	2/1	0	0	0
	2/2	$\frac{1}{2}e^{\pm i2\theta}$	$\frac{1}{3}$	$\frac{3}{10}$
0	1/1	1	$\frac{1}{3}\cos(2\theta)$	$\frac{1}{10}(3\cos(2\theta)-\cos(2\beta_i-2\theta))$
	1/2	0	0	0
	2/1	0	0	0
	2/2	0	$\frac{1}{3}$	$\frac{2}{5}$

enhanced for $l = 2, 5$, compared to those for $l = 1, 6$ and $l = 3, 4$. This kind of enhancement is well-known in conventional Mössbauer spectra, and is also expected in diffraction spectra. Table 4.1 shows that for both the isotropic and anisotropic distributions of HMFs, the value of $\overline{P^2}_{\rm nuc}/\overline{P}_{\rm nuc}(2\theta = 0)$, averaged over the polarization states, is approximately $\frac{2}{3}$ for both $M = \pm 1$ and $M = 0$. On the other hand, for the uniaxial distribution in which all nuclear magnetic moments are aligned along $\hat{z}$, the value of $\overline{P^2}_{\rm nuc}/\overline{P}_{\rm nuc}(2\theta = 0)$ averaged over the polarization states is $\frac{1}{4}$ if $M = \pm 1$, and $\frac{1}{2}$ if $M = 0$. Transitions 2 and 5 are therefore favored when an external magnetic field is applied to the sample in a direction perpendicular to the scattering plane, as shown in Fig. 4.4

Figure 4.4 also shows that the diffraction energy spectrum is asymmetric. This is caused by the interference between electronic scattering and nuclear resonant scattering, in which the phase of the polarization factor plays an important role. The asymmetry is more evident for the "In Field" case than the "No Field" case because the phase factor in the polarization factor is averaged out over the distribution of HMF in the case of "No Field." This same argument explains why the diffraction energy spectra are similar for the isotropic and the anisotropic planar-biased HMF distributions.

The dependence of polarization factors on the HMF orientation distribution could be used to obtain information on the orientation distribution of the sample magnetization. However, Eqs. (4.29), (4.24) and (B.10) show that when λ is large, the polarization factor vanishes ($\overline{P^2} = 0$ if $\lambda > 4$, and $\overline{P} = 0$ if $\lambda > 2$). In practice, this means that the polarization factors are not sensitive to sharp gradients in the orientation distribution. Only small differences are found for the intensity differences of the HMF distributions in Fig. 4.4. A benign consequence is that the polarization factors probably do not vary significantly for different polycrystalline samples.

Previous analysis [42] of the polarization factors for Mössbauer diffractometry accounted for the interference between the different nuclear transitions in the case when the HMF distribution is isotropic and without interference with x-ray Rayleigh scattering. The present analysis accounts for a general orientation distribution of the HMF and includes interference with x-ray Rayleigh scattering, but does not account for interference between different nuclear transitions. Although the present analysis is acceptable for the analysis of Mössbauer diffractions from ferromagnetic iron, a more general analysis using the full matrix of $\overline{P^2}^{n_i n_f M M'}$ will be necessary for samples with strong overlaps of different nuclear transitions.

4.6 Dynamical Theory of Mössbauer Diffraction

For a complete QED dynamical theory of Mössbauer diffraction, please see references [28, 29]. The derivations here follow mostly Ref. [29], and some symbols similar to those in Ref. [60] are used to simply expressions.

The basic idea is to “cut” the crystal into very thin slices so that inside each slice kinematical theory of diffraction can be applied.

4.6.1 Scattered Wave from a Thin Layer of Crystal

Here we seek the scattered wave from a thin layer of crystal. We first present the formalisms of kinematical theory, then apply the formalism to a thin layer of crystal regarded as a two-dimensional structure.

Scattered Wave from a Collection of Atoms in Kinematical Diffraction Theory

In this Section we derive the basic formula (Eq. 4.52) of kinematical diffraction theory: the scattered wave amplitude, ψ, as a function of scattering vector, $\mathbf{k}$, on a detector far from the scattering center, is proportional to the Fourier transform of scattering amplitude as a function of $\mathbf{r}$ inside the crystal.

As pointed out in Section 3.1.3 and 3.2, the scattered wave from a Mössbauer atom in response to an incident photon $A^{in}_\mu(\mathbf{r},\, t) = a^i_\mu \exp i(\mathbf{k}^i \cdot \mathbf{r})$ is

$$A^{sc}_\mu = f_{\mu\nu} a^i_\nu \, \frac{e^{ik^i r}}{r} \tag{4.43}$$

where we have explicitly written down the scattering form factor as a tensor $f_{\mu\nu}$. The cartesian indexes are denoted by μ and ν, whereas a repetition of any of those indexes indicates a summation. The superscript i indicates the incident wave. The μ component of the amplitude of the incident wave is a^i_μ. The scattered wave from a collection of atoms at positions $\{\mathbf{r}_i\}$ is then

$$A_\mu(\mathbf{r}) = \sum_i f_{i;\,\mu\nu} a^i_\nu e^{i\mathbf{k}^i\cdot\mathbf{r}_i} \, \frac{e^{ik^i|\mathbf{r}-\mathbf{r}_i|}}{|\mathbf{r}-\mathbf{r}_i|} \tag{4.44}$$

where the scattering form factor of atom i is $f_{i;\,\mu\nu}$. This equation can be rewritten by using Dirac δ functions

$$A_\mu(\mathbf{r}) = \int d^3\mathbf{r}' f_{\mu\nu}(\mathbf{r}') \sum_i e^{i\mathbf{k}^i\cdot\mathbf{r}_i} \delta(\mathbf{r}'-\mathbf{r}_i) \, \frac{e^{ik^i|\mathbf{r}-\mathbf{r}'|}}{|\mathbf{r}-\mathbf{r}'|} \, a^i_\nu \tag{4.45}$$

where the function $f_{\mu\nu}(\mathbf{r})$ is defined to have value of $f_{i;\,\mu\nu}$ at each position $\mathbf{r} = \mathbf{r}_i$. Notice that $\frac{e^{ikr}}{r}$ is just the photon propagator (Green’s function)

$$D^{(0)}(\mathbf{r},\, \omega) = -\frac{e^{i\omega r}}{r}\ . \tag{4.46}$$

We obtain

$$A_\mu(\mathbf{r}) = -\int d^3\mathbf{r}' \mathcal{A}_{\mu\nu}(\mathbf{r}') D^{(0)}(\mathbf{r}-\mathbf{r}',\, k^i)\, a^i_\nu \tag{4.47}$$

$$= -\mathcal{A}_{\mu\nu} \otimes D^{(0)}\, a^i_\nu \tag{4.48}$$

where $\otimes$ denotes a convolution and the function $\mathcal{A}_{\mu\nu}(\mathbf{r}')$ is defined as

$$\mathcal{A}_{\mu\nu}(\mathbf{r}') = f_{\mu\nu}(\mathbf{r}') \sum_i e^{i\mathbf{k}^i\cdot\mathbf{r}_i} \delta(\mathbf{r}'-\mathbf{r}_i) \tag{4.49}$$

The Fourier transform (F.T.) of Eq. 4.48 gives the F.T. of $A_\mu(\mathbf{r})$, $A_\mu(\mathbf{k})$, as

$$A_\mu(\mathbf{k}) = -\mathcal{A}_{\mu\nu}(\mathbf{k}) D^{(0)}(\mathbf{k},\, k^i)\, a^i_\nu \tag{4.50}$$

The F.T. of $\mathcal{A}_{\mu\nu}(\mathbf{r}')$ is easy to evaluate from Eq. 4.49

$$\mathcal{A}_{\mu\nu}(\mathbf{k}) = \sum_i f_{i;\,\mu\nu} e^{i(\mathbf{k}^i-\mathbf{k})\cdot\mathbf{r}_i} \tag{4.51}$$

which is just the Fourier tranform of the spatial distribution of the form factors. The scattered wave field is then

$$A_\mu(\mathbf{k},\, t) = -D^{(0)}(\mathbf{k},\, k^i) \sum_i f_{i;\,\mu\nu} e^{i(\mathbf{k}^i-\mathbf{k})\cdot\mathbf{r}_i - i\omega^i t}\, a^i_\nu \tag{4.52}$$

where we make use of Eqs. 4.50 and 4.51, and explicitly include the time evolution. After taking the Fourier transform of the time variable, t, we obtain

$$A_\mu(\mathbf{k},\, \omega) = -D^{(0)}(\mathbf{k},\, k^i) \sum_i f_{i;\,\mu\nu} e^{i(\mathbf{k}^i-\mathbf{k})\cdot\mathbf{r}_i} 2\pi\delta(\omega-\omega^i)\, a^i_\nu \tag{4.53}$$

$$= -2\pi D^{(0)}(\mathbf{k},\, \omega) \sum_i f_{i;\,\mu\nu} e^{i(\mathbf{k}^i-\mathbf{k})\cdot\mathbf{r}_i} \delta(\omega-\omega^i)\, a^i_\nu \tag{4.54}$$

The photon propagator in reciprocal space is given by

$$D^{(0)}(\mathbf{k},\, \omega) = \frac{4\pi}{\omega^2 - k^2 + i\epsilon} \tag{4.55}$$

Scattered Wave from a Thin Layer

The periodicity of a crystal can be used to rewrite the summation, $\sum_i f_{i;\,\mu\nu} e^{i(\mathbf{k}^i - \mathbf{k})\cdot\mathbf{r}_i}$, to a product of the structure factor and the shape factor[13]

$$\mathcal{F}_{\mu\nu}(\mathbf{k}^i - \mathbf{k})\mathcal{S}(\mathbf{k}^i - \mathbf{k})$$

where the structure factor $\mathcal{F}_{\mu\nu}(\mathbf{k}^i - \mathbf{k})$ depends on the strucuture of the unit cell of the crystal

$$\mathcal{F}_{\mu\nu}(\mathbf{k}^i - \mathbf{k}) = \sum_i^{\mathrm{uc}} f_{i;\,\mu\nu} e^{i(\mathbf{k}^i - \mathbf{k})\cdot\mathbf{r}_i} \tag{4.56}$$

and the shape factor $\mathcal{S}(\mathbf{k}^i - \mathbf{k})$ depends on the periodicity and geometry of the crystal

$$\mathcal{S}(\mathbf{k}^i - \mathbf{k}) = \sum_i e^{i(\mathbf{k}^i - \mathbf{k})\cdot\mathbf{R}_i} \tag{4.57}$$

where $\mathbf{R}_i$ is the position of unit cell i. For a thin layer of crystal of thickness b, the shape factor is a sum of 2D Dirac functions

$$\mathcal{S}(\mathbf{k}^i - \mathbf{k}) = \frac{4\pi^2 b}{v} \sum_\tau \delta(\mathbf{k}^i_{xy} - \mathbf{k}_{xy} - \mathbf{g}_\tau) \tag{4.58}$$

where v is the volume of the unit cell, and $\{\mathbf{g}_\tau\}$ are the 2D reciprocal vectors. Here τ is regarded as an index of "channel", to be defined in the next subsection. Therefore, the scattered wave is

$$A_\mu(\mathbf{k}, \omega) = -2\pi D^{(0)}(\mathbf{k},\, \omega)\mathcal{F}_{\mu\nu}(\mathbf{k}^i - \mathbf{k})\mathcal{S}(\mathbf{k}^i - \mathbf{k})\delta(\omega - \omega^i)\, a^i_\nu \tag{4.59}$$

The transformation back to real space by a 4D Fourier transform is not difficult now: the integrations of k_x, k_y, and t are trivial because of the δ function in the function $\mathcal{S}(\mathbf{k}^i - \mathbf{k})$ and the δ function $\delta(\omega - \omega^i)$; the integration of k_z is related to

$$\int dk_z D^{(0)}(\mathbf{k},\, \omega)\, e^{ik_z z} = \int dk_z \frac{4\pi}{k_\tau^2 - k_z^2 + i\epsilon} e^{ik_z z} \tag{4.60}$$

where k_τ is defined as

$$k_\tau = \sqrt{(\mathbf{k}^i)^2 - \left(\mathbf{k}^i_{xy} + \mathbf{g}_\tau\right)^2} \tag{4.61}$$

---

[13] See, for example, Ref. [20], pg 342.

Equation 4.60 can be evaluated as:

$$\int dk_z \frac{4\pi}{k_\tau^2 - k_z^2 + i\epsilon} e^{ik_z z} = -\frac{4\pi^2 i}{k_\tau}\left[e^{ik_\tau z}\theta(z) + e^{-ik_\tau z}\theta(-z)\right] \tag{4.62}$$

where

$$\begin{aligned} \theta(x) &= 1 \text{ if } x > 0 \\ &= 0 \text{ if } x < 0 \end{aligned} \tag{4.63}$$

Finally we obtain

$$\begin{aligned} A_\mu(\mathbf{r},t) &= \text{F. T. of } A_\mu(\mathbf{k},\omega) \\ &= \frac{2\pi i b}{v}\sum_\tau \frac{1}{k_\tau}\mathcal{F}_{\mu\nu}(\mathbf{k}^i - \mathbf{k}_{\tau^+}) \exp i\left[\mathbf{k}_{\tau^+}\cdot\mathbf{r} - \omega^i t\right]\, a^i_\nu \;\text{ if } z > 0 \\ &= \frac{2\pi i b}{v}\sum_\tau \frac{1}{k_\tau}\mathcal{F}_{\mu\nu}(\mathbf{k}^i - \mathbf{k}_{\tau^-}) \exp i\left[\mathbf{k}_{\tau^-}\cdot\mathbf{r} - \omega^i t\right]\, a^i_\nu \;\text{ if } z < 0 \end{aligned} \tag{4.64}$$

where

$$\mathbf{k}_{\tau^\pm} = \mathbf{k}^i_{xy} + \mathbf{g}_\tau \pm \hat{z}k_\tau \tag{4.65}$$

Therefore, the scattered wave from a thin layer of Mössbauer atoms is a superposition of waves with wave vectors $\{\mathbf{k}_{\tau^\pm}\}$. A wave of wave vector $\mathbf{k}_{\tau^s}$ is called a wave of "channel" τ^s, where $s = + \, or \, -$. Wave of channel τ^+ only exists at $z > 0$, while that of channel τ^- only exists at $z < 0$.

4.6.2 Propagation of Waves

The optics for a thin layer of Mössbauer atoms was presented in the previous Section. Now we develop the optics of a perfect crystal. As mentioned before, a crystal is cut into layers and the propagation of waves in these layers is tracked. In general, there might be a few channels with nonzero amplitudes (those channels are called "open"). For simplicity, we will only consider the optics of Bragg diffraction. In this case there are only two open channels: one for transmission, the other for reflection. A further simplification is achieved by assuming that there is no coupling between polarizations. To simplify formalisms, we define

$$\phi(\tau_2^{s_2}, \tau_1^{s_1}) = \frac{2\pi}{v}\frac{\mathcal{F}_{\mu\nu}(\mathbf{k}_{\tau_1^{s_1}} - \mathbf{k}_{\tau_2^{s_2}})}{k_\tau} \tag{4.66}$$

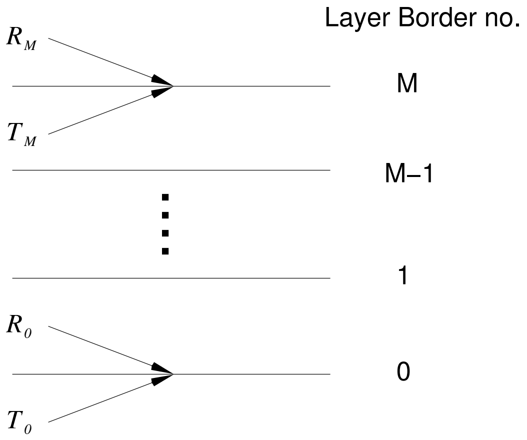

Figure 4.5: Propagation of transmission and reflection waves.

The propagation of the transmission wave from layer m to layer $m+1$ is then given by (please refer to Fig. 4.5)

$$A^{0+}_{m+1} = A^{0+}_m e^{ik_0 b}(1 + ib\phi^{00}) + A^{1-}_m ib\phi^{01} e^{ik_0 b} \tag{4.67}$$

where ϕ^{01} is an alias for $\phi(0^+,\,1^-)$. Similarly, for the reflection wave we have

$$A^{1-}_{m-1} = A^{1-}_m e^{ik_1 b}(1 + ib\phi^{00}) + A^{0+}_m ib\phi^{10} e^{ik_1 b} \tag{4.68}$$

where ϕ^{10} is an alias for $\phi(1^-,\,0^+)$. To use the symbols that look more familiar and to simplify the formalisms, the transmission wave amplitude T and the reflection wave amplitude R are defined as

$$\begin{aligned} T_m &= A^{0+}_m / e^{i\,(\mathbf{k}^i + \mathbf{G}_0)_z mb} \qquad (4.69)\\ R_m &= A^{1-}_m / e^{i\,(\mathbf{k}^i + \mathbf{G}_1)_z mb} \qquad (4.70) \end{aligned}$$

Here $\mathbf{G}_0 = 0$ and $\mathbf{G}_1$ is the reciprocal vector that connects the incident wave vector to the reflected wave vector. Define

$$\kappa_{\tau\pm} = k_\tau \mp (\mathbf{k}^i + \mathbf{G}_\tau)_z \tag{4.71}$$

Then we have

$$\begin{aligned} T_{m+1} &= T_m e^{i\kappa_{0+} b}(1 + ib\phi^{00}) + R_m ib\phi^{01} e^{i\kappa_{0+} b} \qquad (4.72)\\ R_{m-1} &= R_m e^{i\kappa_{1-} b}(1 + ib\phi^{00}) + T_m ib\phi^{10} e^{i\kappa_{1-} b} \qquad (4.73) \end{aligned}$$

The boundary conditions are

$$T_0 = a^i \tag{4.74}$$

$$R_M = 0 \tag{4.75}$$

where $M = d/b$ and d is the thickness of the crystal. To solve this propagation problem, one way is to transform these two equations into differential equations. In order to enable the transformations, it is necessary to define the quantities $\{\delta_\tau\}$

$$\kappa_{\tau^s} b = 2\pi(n + \delta_{\tau^s} b/2\pi) \tag{4.76}$$

where [14]

$$0 \leq \delta_{\tau^s} b/2\pi \ll 1 \tag{4.77}$$

Then Eqs. 4.72 and 4.73 can be approximated by differential equations (by doing first order expansions like $T_{m+1} = T_m + \frac{dT}{dz} b$ and $e^{i\kappa_\tau b} = 1 + i\delta_\tau b$)

$$\frac{dT}{dz} = i\delta_{0^+} T + iT\phi^{00} + iR\phi^{01} \tag{4.78}$$

$$-\frac{dR}{dz} = i\delta_{1^-} R + iR\phi^{11} + iT\phi^{10} \tag{4.79}$$

with boundary conditions

$$T(0) = a^i \tag{4.80}$$

$$R(d) = 0 \tag{4.81}$$

The solution of this set of differential equations gives the reflection coefficient as [15]

$$R(0)/a^i = -\frac{\phi^{10}}{\alpha + i\beta\zeta} \tag{4.82}$$

where

$$\alpha = \frac{1}{2}(\phi^{00} + \phi^{11} + \delta_{0^+} + \delta_{1^-}) \tag{4.83}$$

$$\beta = \frac{1}{2}\sqrt{-\alpha^2 + \phi^{01}\phi^{10}}, \mathrm{Re}[\beta] > 0 \tag{4.84}$$

---

[14] Note that the experimental condition is very close to Bragg diffraction.

[15] This is tedious, but one can do it with Maple, for example.

$$\zeta \quad = \quad \coth(\beta d) \tag{4.85}$$

For a thick crystal, $\beta d \gg 1$, and we have $\zeta = 1$. So

$$\frac{R(0)}{a^i} = -\frac{\phi^{10}}{\alpha + i\beta} \tag{4.86}$$

For a thin crystal, $\beta d \ll 1$, we have

$$\zeta = \frac{e^{\beta d} + e^{-\beta d}}{e^{\beta d} - e^{-\beta d}} \simeq \frac{2 + (\beta d)^2}{2\beta d} = \frac{1}{\beta d} + \frac{\beta d}{2} \tag{4.87}$$

So

$$\frac{R(0)}{a^i} \simeq -\frac{\phi^{10}}{\alpha + i\beta^2 d/2 + i/d} = -\frac{\phi^{10} d}{\alpha d + i\beta^2 d^2/2 + i} \simeq -\frac{\phi^{10} d}{\alpha d + i} \tag{4.88}$$

4.6.3 Enhancement of Coherent Scattering Width

A remarkable feature of dynamical Mössbauer diffraction is the suppression of resonant absorption near a Bragg angle. Here we use a more specific example to illustrate this phenomenon. Suppose the incident radiation is arranged for the (332) Bragg diffraction from a bcc ^{57}Fe crystal. The diffraction angle, 2θ, is about 90°. The unit cell has two ^{57}Fe atoms, and its size is a =2.89 Å. The unit cell volume is

$$v = a^3 = 23.4\,\text{Å}^3 \tag{4.89}$$

An external magnetic field is used to align the hyperfine magnetic fields to be perpendicular to the scattering plane. The incident γ-ray is tuned to be near resonance with transitions of $m = 0$ (line 2 or line 5 of the sextet). Then the polarization factor is (Eqs. 3.73 and 3.74)

$$p = \mathbf{h} \cdot \mathbf{u}_z \tag{4.90}$$

So only photons with polarization $\mathbf{h}$ perpendicular to the scattering plane will be scattered. For these photons, we have [16](using Eqs. 4.66 and 4.8)

$$\phi^{11} = \phi^{00} = \phi^{01} = \phi^{10} = C\frac{1}{\frac{2}{\Gamma_1}(E_{10} - E) - i} \tag{4.91}$$

where

$$C = 2 \times \frac{3\eta f_{\mathrm{ML}}}{4k(1 + \alpha_{\mathrm{IC}})}\frac{2}{3} \times \frac{2\pi}{v}\frac{1}{\kappa_0} = \frac{2\pi\eta f_{\mathrm{ML}}}{vk^2 \sin[(2\theta)/2](1 + \alpha_{\mathrm{IC}})} \tag{4.92}$$

---

[16] We neglect scattering from electrons for simplicity.

The wave vector is

$$k = \frac{1}{\lambda/2\pi} = \frac{1}{0.86\text{Å}/2\pi} = [0.137\text{Å}]^{-1} \tag{4.93}$$

The enrichment of ^{57}Fe, η, is assumed to be 0.9. The internal conversion factor is

$$\alpha_{\text{IC}} = 8.21 \tag{4.94}$$

So

$$C = 5.4 \times 10^{-4}\text{Å}^{-1} \tag{4.95}$$

The diffraction is assumed to be very close to Bragg condition, then $\delta_{0^+} = \delta_{1^-} = 0$. So Eq. 4.83 reduces to

$$\alpha = \phi^{00} \tag{4.96}$$

Thick Crystal

From Eq. 4.84 and 4.91, we have

$$\beta = 0 \tag{4.97}$$

Therefore, the reflection is (from Eq. 4.86)

$$\frac{R(0)}{a^i} = -1 \tag{4.98}$$

which means that all wave is reflected into the (332) diffraction and all absorption is suppressed. This is a truly remarkable result, but this is an ideal case in which we have assumed 1) infinitely thick crystal, 2) perfect Bragg condition, and 3) no electronic scattering.

Thin Crystal

We have (from Eqs. 4.88 and 4.91)

$$\frac{R(0)}{a^i} = -\frac{1}{1 + \frac{i}{d}\frac{1}{C}\left[\frac{2}{\Gamma_1}(E_{10} - E) - i\right]} \tag{4.99}$$

Therefore, the "energy line-width of the crystal" due to dynamical diffraction is

$$\Gamma_{\text{xtl}} = (1 + dC)\Gamma_1 = (1 + dC)(1 + \alpha_{\text{IC}})\Gamma_{1\gamma} \tag{4.100}$$

The enhancement factor is then $(1+dC)(1+\alpha_{\mathrm{IC}})$. For a crystal of thickness $d = 10^4 a$ (10^4 layers, each layer in the thickness of one unit cell), the enhancement is 1.5×10^2. With a crystal of adequate thickness, the coherent scattering energy width can dominate over widths of other decay channels like internal conversion. As a result, the absorption is suppressed, and the energy width of the nuclear resonance is broadened. For a crystal of ^{57}Fe nuclei oriented for Bragg diffraction, the decay rate of the nuclear excited state is reduced from its usual half-life of $140\,ns$. Experiments with high-quality crystals have shown that the speed-up of nuclear decay can be a factor of 300 in the coherence hcannel, giveing a line broadening of about a factor of 40.

Naive Explanation

The key point is the coherence among the nuclear states in the crystal. First look at a system composed of two nuclei. The coupling between the two nuclei results in two modes, for which the decay rates are given by

$$\Gamma_{\pm} = \frac{1}{2}\Gamma_\gamma \overline{|1 \pm exp(i\mathbf{k}\cdot\mathbf{R})|^2} = \Gamma_\gamma \frac{\sin(kR)}{kR} \tag{4.101}$$

This is a result of the coherent superposition of decaying amplitudes of two nuclei. Similarly, the linewidth of coherent radiation decay of a nuclear exciton (a Bloch-wave-like mode which is the superposition of nuclear states of nuclei in the crystal) is

$$\Gamma_{\mathrm{c}}(\mathbf{q}) = \frac{\Gamma_\gamma}{4\pi N}\int d\Omega_{\mathbf{n}} \left|\sum_l \exp(-i(\mathbf{k}-\mathbf{q})\cdot\mathbf{R}_l)\right| \tag{4.102}$$

For most of the modes, there is a random distribution of phase for nuclear states and the radiation decay rate decreases to the order of Γ_γ/N. Near the Bragg condition, many nuclear states are in phase and as a result, the radiation decay rate is enhanced because of the coherence

$$\Gamma_{\mathrm{c}} = \frac{2\pi}{vk^2}\frac{d}{\sin[(2\theta)/2]}\frac{2j_1+1}{4j_0+2}\eta f_{\mathrm{ML}}\cdot\Gamma_\gamma \tag{4.103}$$

4.7 Test for the Applicability of Kinematical Theory

Dynamical theory is necessary in the case of thick crystals. In this Section we present one way to evaluate the importance of dynamical effects, by using the CONUSS software package.

CONUSS is a software package for calculating the nuclear-resonance scattering of photons [59]. It implements the theory of Hannon and Trammel [28] for the coherent scattering of γ-ray and x-ray photons by the nucleus and the electrons of each atom. In CONUSS the same multi-slice method presented in Ref. [29] and outlined in Section 4.6 is used for the propagation of the incident wavefield.

Mössbauer diffractions from polycrystalline samples have been interpreted successfully with kinematical theory [39, 35], but this requires that multiple scattering is suppressed by small crystal sizes or crystalline imperfections. In the present work, CONUSS was adapted to test this assumption. A polycrystalline sample was modeled as composed of crystallites, all of equal size, ζ. The sample was divided into slices, each with thickness ζ. For each crystallite in each slice, the transmission and scattering properties were obtained with CONUSS. All crystallites were of one of two types, either oriented perfectly for Bragg diffraction, or oriented improperly. The use of only perfectly-oriented crystals for Bragg diffraction should underestimate the thickness where dynamical effects become important. Owing to their weaker intensities, superlattice diffractions should be in the kinematical limit for even thicker crystals. We define r_p to be the reflecting power from a perfectly-oriented crystal, t_p the transmission probability (the fraction of incident photons transmitted through the perfectly-oriented crystal), and t_i the transmission probability through an improperly-oriented crystal. The scattering intensity of a γ-ray from a slice at the depth of $m\zeta$, I_{sc}, is then:

$$I_{\mathrm{sc}} = (x_p t_p + x_i t_i)^{m-1} r_p (x_p t_p + x_i t_i)^{m-1} \ ,$$

where x_p and x_i are the fractions of perfectly and improperly-oriented crystals in the sample, respectively. The diffraction intensity from the sample is an incoherent sum of the scattering intensities from all slices,

$$I_{\mathrm{sc}} = r_p \, \frac{1 - T^{t/\zeta}}{1 - T} \ , \tag{4.104}$$

where $T = (x_p t_p + x_i t_i)^2$.

Chapter 5

Instrumentation and Data Analysis Procedure

5.1 Diffractometer

In essence, a Mössbauer diffractometer consists of a γ-ray source, a detector and a goniometer. A schematic of our diffractometer[1] is presented in Figure 5.1.

A pair of slits, fitted near its exit with a Pb-Cu-Al graded shield, collimates the radioactive source to a beam of cross section 10 mm×2 mm. An optional external magnetic field was applied to the sample in the vertical direction with a permanent magnet having Nd-Fe-B pole pieces and a field of 0.33 T. A Bruker X-1000 Xe-filled position-sensitive detector is mounted on the outer stage of a General Electric XRD-5 θ-2θ goniometer. A Wissel Mössbauer drive system provides a digital function generator, electronics for feed back control, a Doppler drive transducer, and a laser interferometer for absolute velocity measurements.

Signals from the detector are gathered by the "Frambo" computer, which is loaded with a software program (frambo) that runs under MS-DOS 5.0 [2]. Through a RS232 serial port, the control computer talks to a keyboard emulator, which commands this "frambo" software to do the data collection. The data files are transferred from the "Frambo" computer to the control computer through Ethernet. A veto generator and a velocity controller, both custom-made, can receive commands from the control computer, and control the status of the instrumentation.

---

[1] This is the "second generation" diffractometer built in our research group, mostly by Ushma Kriplani[34]. The new modal has been upgraded in the Mössbauer drive system. We have also been working on circuits for a new velocity controller, veto generator, and velocity read-back, of which details can be found in section 5.1.2.

[2] Sounds really outdated, hah! But the point is, it is still working!

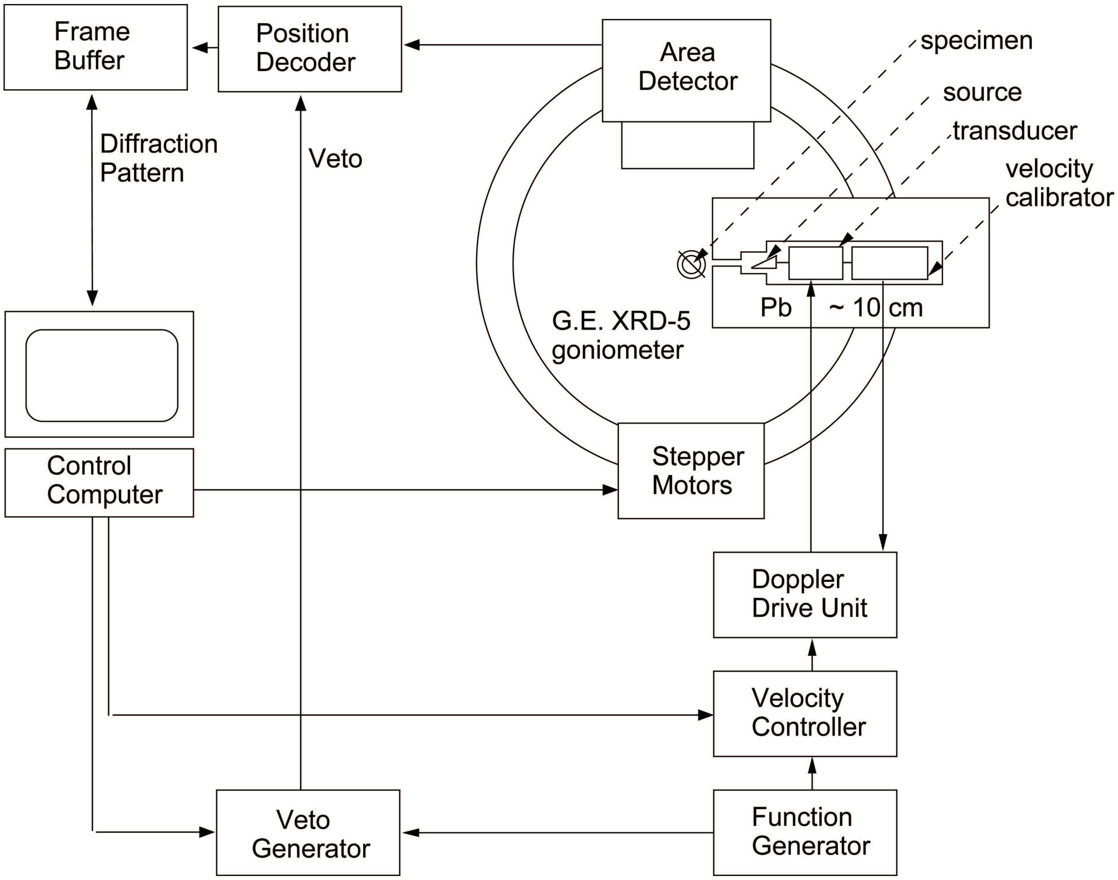

Figure 5.1: Schematic of the Mössbauer powder diffractometer.

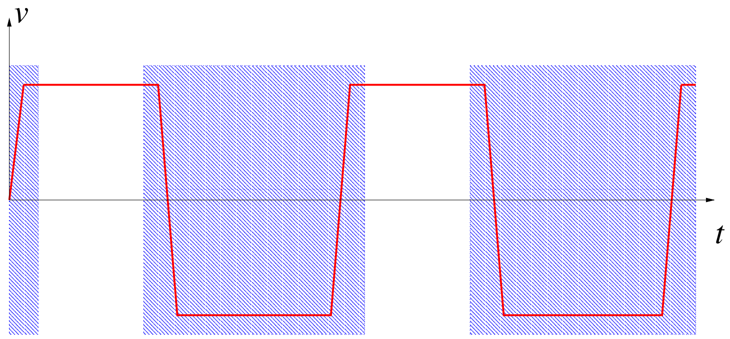

Figure 5.2: Operation of veto generator for Doppler drive running in constant velocity mode. Detector signals are collected only when the Doppler drive is at the desired velocity. At times when the Doppler drive is in regions of blue shadow, the detector is disabled by the veto generator.

5.1.1 Detector

There is a detailed description of the Bruker detector in Kriplani's thesis [34]. The X-1000 area detector includes a chamber pressurized to approximately 4 bar with Xe gas. Locations of γ-ray detection are provided with a multi-wire grid electrode, about 10 cm×10 cm in size. The detector subtends a solid-angle of approximately 1 sr[3] about the sample. It has very high efficiency ($> 80\%$) in stopping photons of 14.4 keV and, fortunately, stops few photons of 122 keV energy from the initial decay of the ^{57}Co nucleus. It also has good spatial resolution (200μm). It unfortunately has no energy resolution. The Bruker detector is a planar detector, so a basic data reduction procedure is required to transform the acquired data file into an intensity as a function of diffraction angle.

5.1.2 Custom Circuits

We have constructed the following circuits to automate our Mössbauer diffractometer. These circuits were built in part upon the past work of Ushma Kriplani, and ongoing work by Ryan Monson[4].

Veto Generator

In conventional Mössbauer spectrometry, the Doppler drive is usually run in the constant acceleration mode, and a multi-channel scaler is used to split a motion period of the Doppler drive into several channels. A Doppler-velocity-dependent signal such as transmission intensity is recorded for every channel. Due to limitations of current detector hardware and software, we were unable to operate

---

[3] about 1/3 of which gives the best-quality diffraction pattern.

[4] Actually Ryan Monson has already built a better version of veto generator.

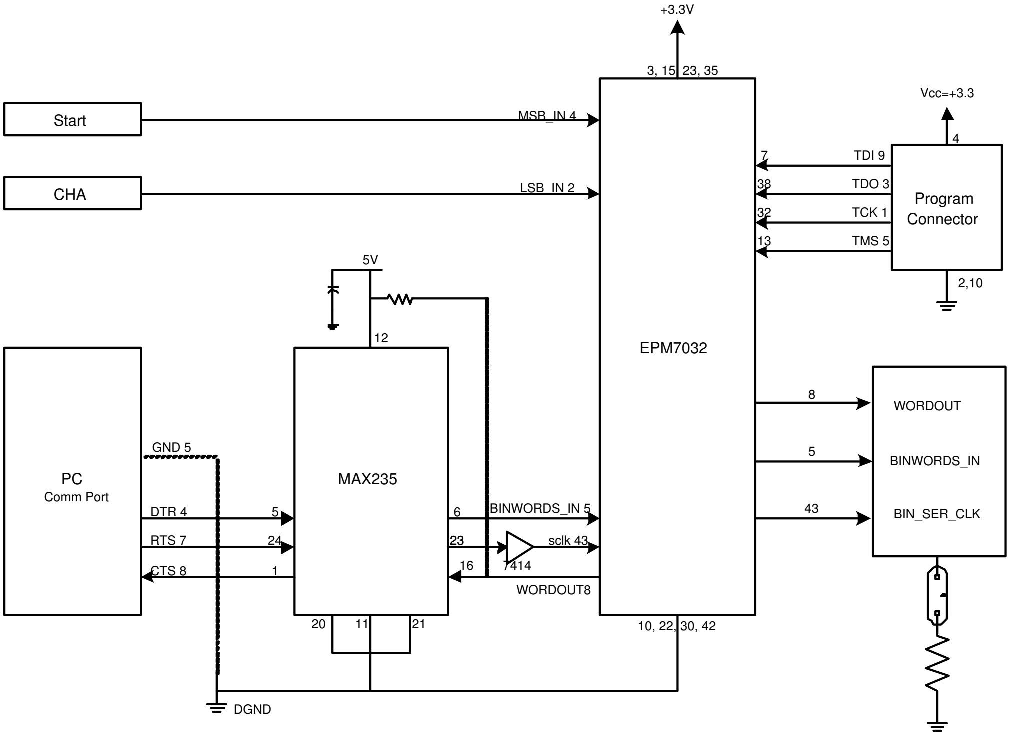

Figure 5.3: Schematic design of the veto generator.

our Mössbauer diffraction spectrometer in the constant-acceleration mode[5]. Instead, the constant velocity mode is used. To obtain a full spectrum of Mössbauer diffraction intensity, a set of diffraction patterns must be acquired at different Doppler velocities. Since a Mössbauer diffraction spectrum is not symmetric about the origin of Doppler velocity ($v = 0$), we must "veto" the detector signals when the Doppler drive is not moving in the desired direction, as shown in Figure 5.2.

The circuit for the veto generator is shown in Fig. 5.3. The control computer can send two numbers, ch_{max} and ch_{min} into the circuit through a RS232 comm port. The channel advance signal from the digital function generator is counted by the circuit to obtain the channel number. This number is in the range (0, 511), with 512 being the total number of channels used in our experiments. The channel number, ch, is compared to ch_{max} and ch_{min}. Only when $ch_{min} < ch < ch_{max}$, the "Enable" output of the veto generator is set to 1. The MAX235 chip is used to transform the signal from RS232 to TTL signals.

The EPM7032, a programmable chip, is the kernel of this circuit. The logic design this chip

---

[5] We should be able to overcome this difficulty with the new-generation diffractometer, which is being built now. Section 7 has more details.

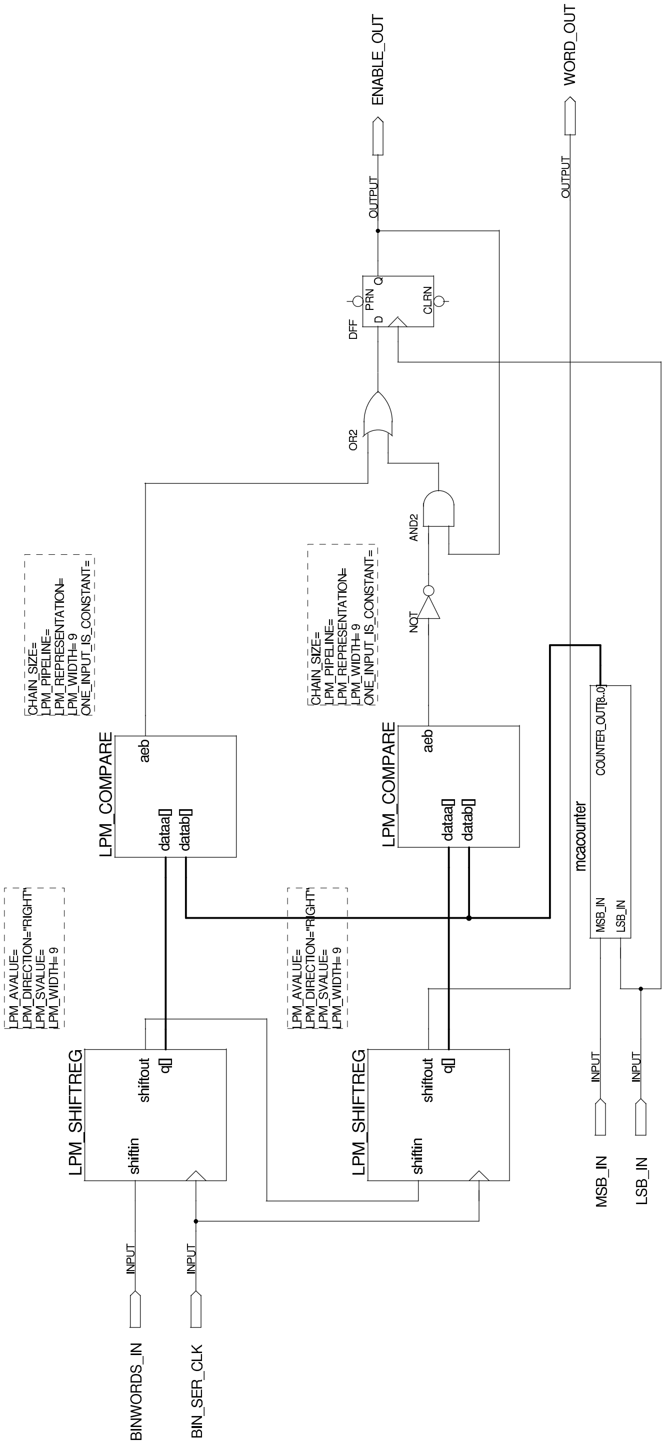

Figure 5.4: Logic design of the veto generator.

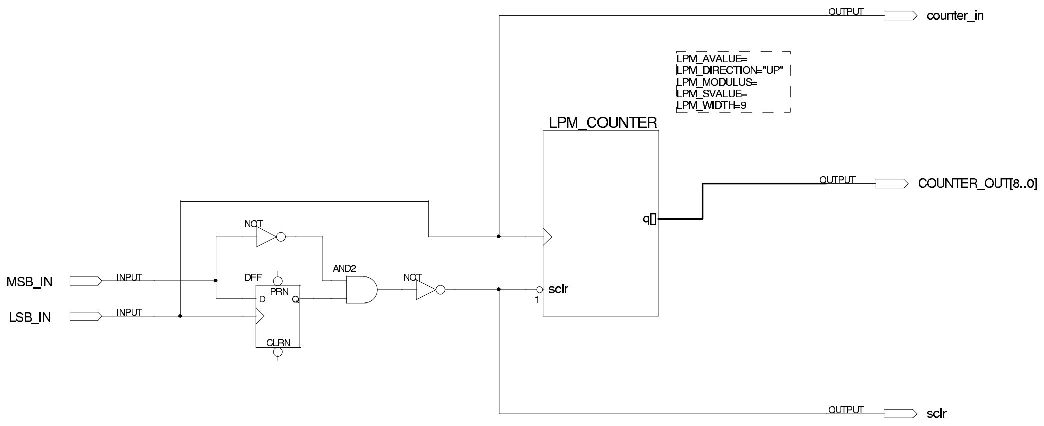

Figure 5.5: MCA counter in the veto generator.

is shown in Fig. 5.4. Two shift registers (LPM_SHIFTREG) are used to get the values of ch_{max} and ch_{min} from the control computer. The channel number, ch, is counted by the "mcacounter" shown in Fig. 5.5. These three numbers are fed to two comparators (LPM_COMPARE) to test if the channel number, ch, is in the right range, indicating that the Doppler drive is moving in the desired direction at the desired speed.

Velocity Controller

The square-wave generated by the Wissel digital function generator is amplified by the velocity controller before being sent to the Doppler drive. This allows the control computer to adjust the Doppler velocity by varyng the gain of the amplifier. A schematic design is presented in Fig. 5.6. MAX532 is a programmable amplifier. The amplification factor is set by the control computer through an RS232 interface.

Velocity Read-Back

The velocity read-back circuit counts the number of laser fringes in specific time periods from the laser interferometer. The control computer then can deduce the velocity of Doppler drive. Figure 5.7 presents the schematic of this circuit. Two RS232 serial ports are used to implement three I/O lines (two output lines: one for resetting devices, another for the clock signal, and one input line: read all bits of counting results).

The core of the velocity read-back circuit is a programmable chip. Its logic design,[6] shown in Fig.

---

[6] The design was started by Ushma Kriplani, and finished by me. The circuit was built by Ryan Monson.

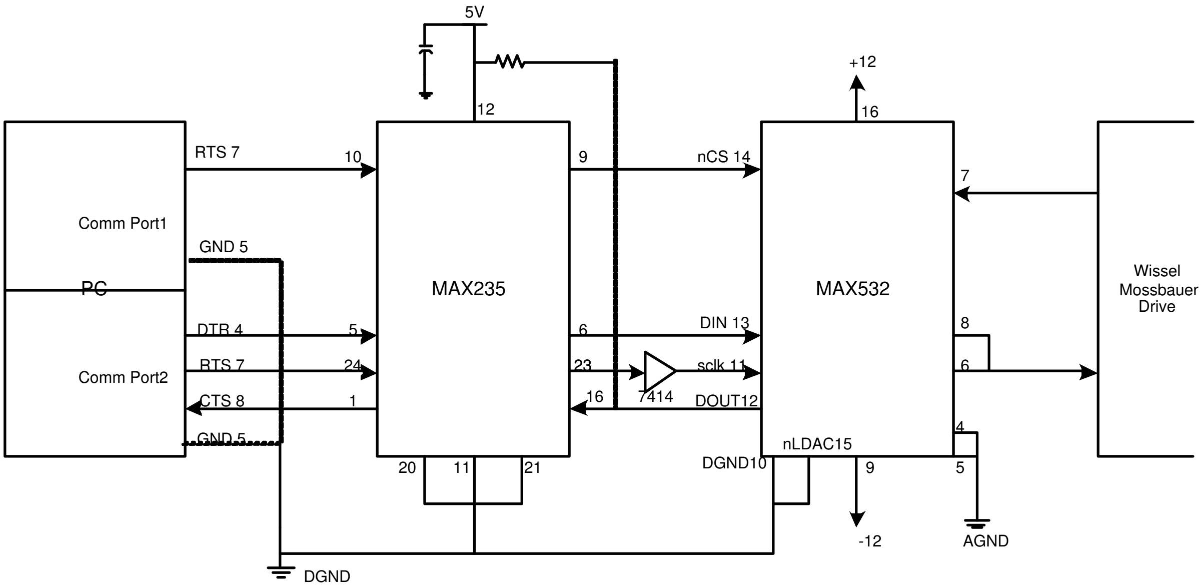

Figure 5.6: Velocity controller schematic design.

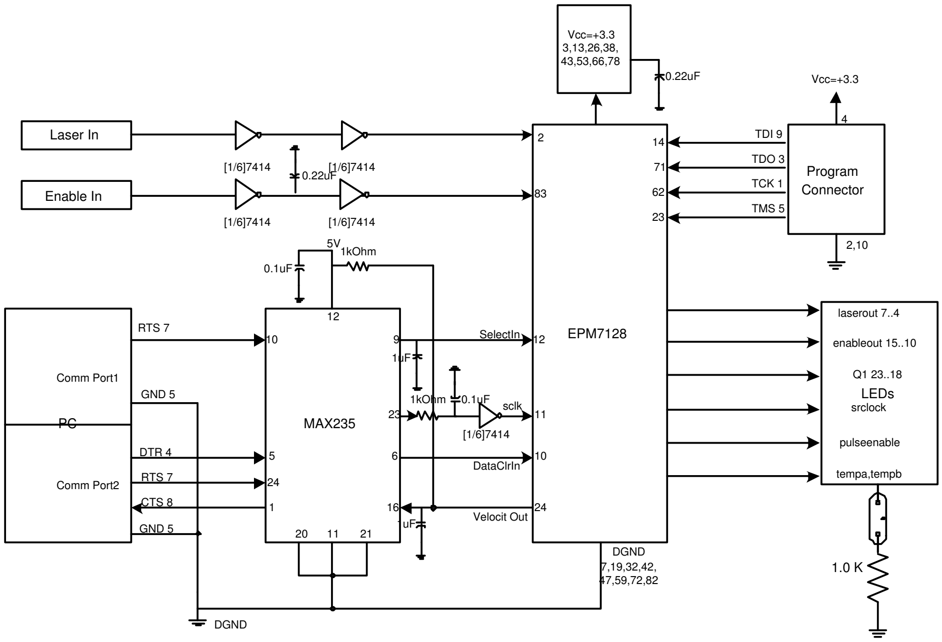

Figure 5.7: Schematic design of the velocity read-back circuit.

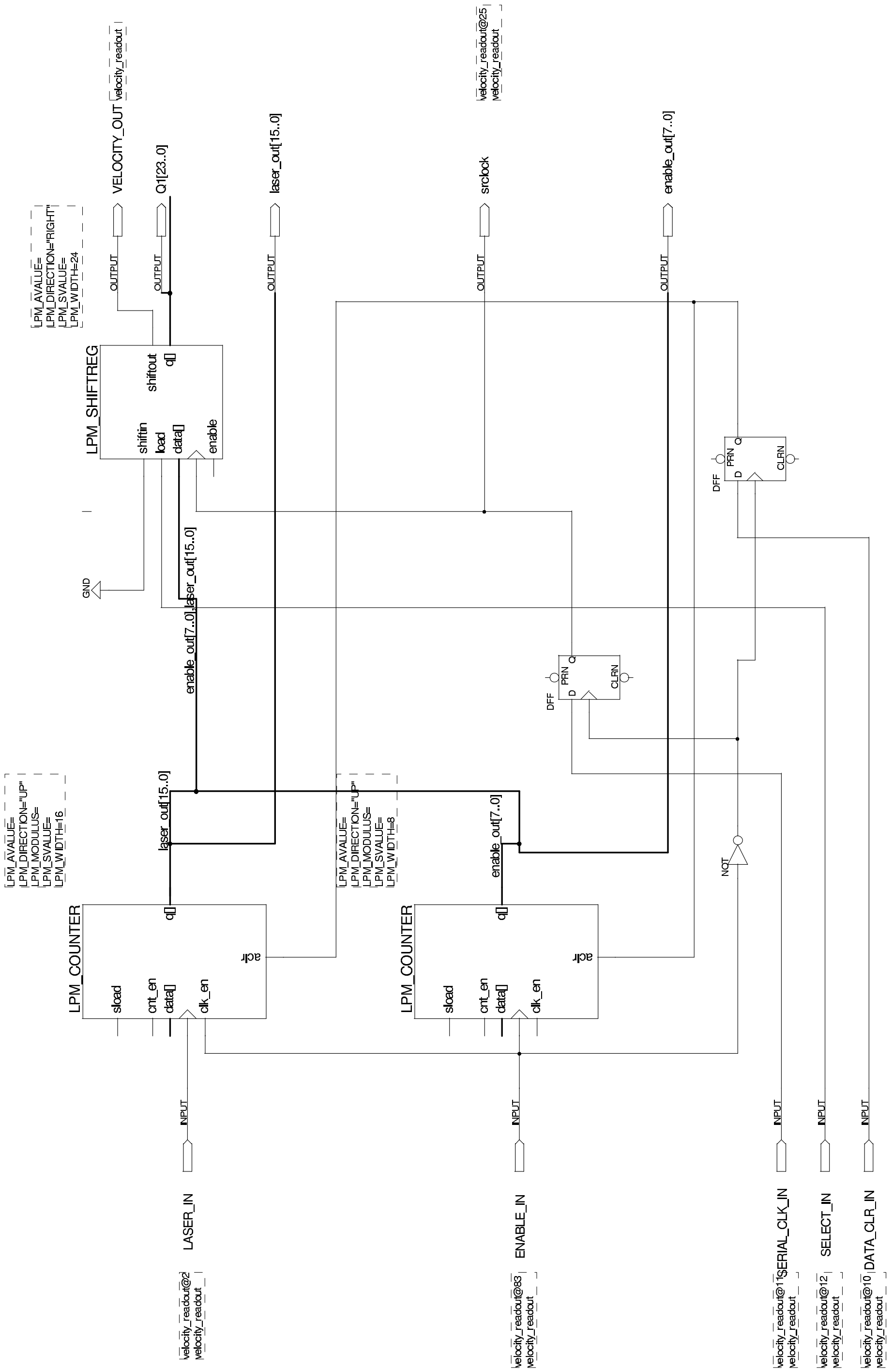

Figure 5.8: Logic design of the velocity read-back circuit.

5.8, was burned into an Altera EPM7128 device. It consists of two counters, one for counting the number of laser fringes and the second for counting the number of cycles of the Doppler drive, and a shift-register for reading the results back to the control computer. Laser fringe signals and veto signals are used as clock signals to the two counters (LPM_COUNTER). By setting DATA_CLR_IN to zero, one can clear both counters. The values of both counters are combined together and sent to a shift-register (LPM_SHIFTREG). The register, when driven by SERIAL_CLK_IN (clock signal for this register), will send the combined value to the RS232 serial port of the control computer.

5.1.3 Data Collection

To examine the data when data acquisition is under way, each raw data file in the "Frambo" computer is transfered to the control computer after it is collected. A Windows Workgroup 3.11 was installed in the DOS operating system on "Frambo" computer so that the data can be transfered through the Ethernet. Every time a detector image is obtained, the control computer tells the Frambo computer to exit the "frambo" software, and starts Windows 3.11 for data transfer. After that, the Frambo computer is asked to restart the "frambo" software.).

Some automation capabilities of the control software are:

1. It can save and load running parameters of a "job", which is usually a set of detector images taken at the same goniometer position but different Doppler velocities. The saved parameter file will be used as an important resource for the data analysis program to determine the experimental conditions on which each detector image is taken.

2. It can keep a list of jobs and automatically run through all jobs.

5.2 General Data Reduction Procedure

To do data analysis more efficiently, three programs have been developed in the course of this thesis research (see Figure 5.9): GCSAXI (C++ program for SAXI image processing with Graphical interface), MDS (Mössbauer Diffraction Simulation) and MEF (Mössbauer diffraction Energy spectra Fitting program). GCSAXI transforms raw data into diffraction patterns, and then energy spectra of diffraction peaks. MDS is a simulation program for calculating energy spectra of diffraction peaks. MEF is the program connecting GCSAXI and MDS. It can compare simulated energy spectra to experimental results and optimize the parameters used in MDS.

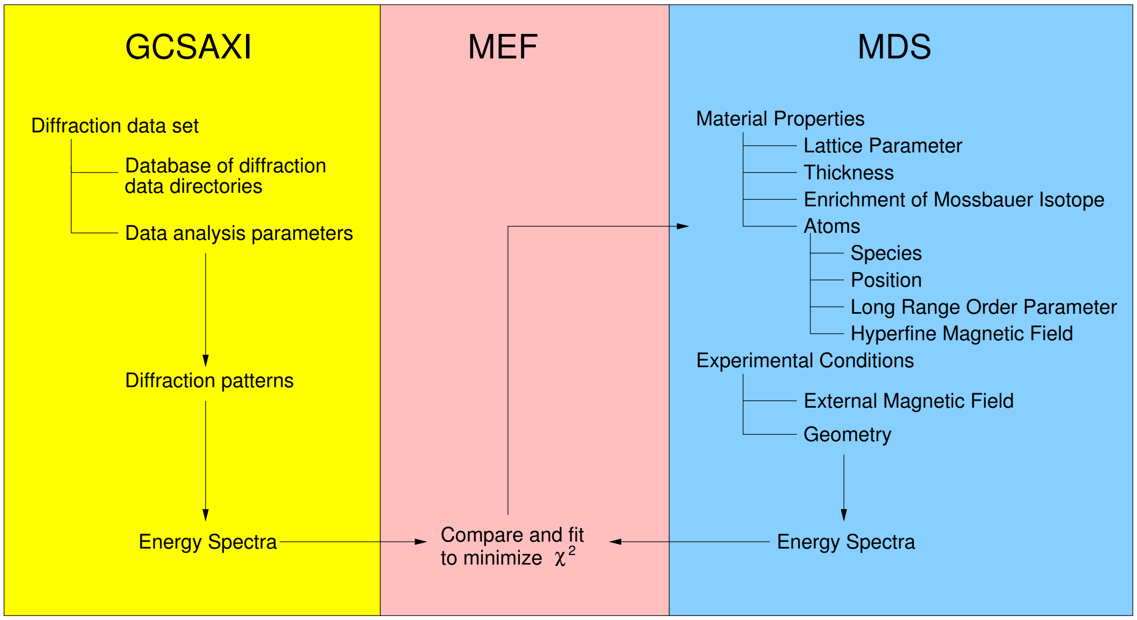

Figure 5.9: Data reduction procedure

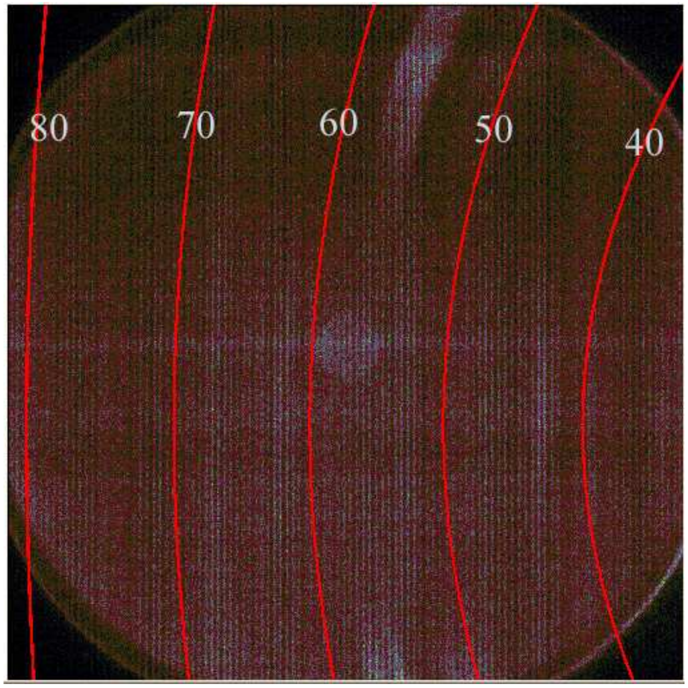

Figure 5.10: A typical SAXI image. Red curves show pixels of $2\theta = 40,\ 50,\ 60,\ 70$ and 80 degree. Some diffraction peaks are visible as bright stripes.

5.2.1 GCSAXI

To compensate for differences in sensitivity of pixels in the area detector, the detector is rotated in several small steps by the step-motor-driven goniometer. For each step, a set of detector images are recorded at selected Doppler velocities. The structure of the acquired data has the following form:

1. A data set is composed of an indefinite number of data directories;
2. In a data directory, there are an indefinite number of detector images, all of which are taken at the same goniometer position. A text file records all parameters used in these experiments;
3. Each image is taken at one Doppler velocity.

The program GCSAXI

1. reads a list of data directories from a database file;
2. for each data directory, it reads the file containing the experimental parameters such as goniometer position and Doppler velocity bins; transforms each image into a diffraction pattern; and categorizes these diffraction patterns according to their Doppler velocities;
3. combines diffraction patterns of all data directories by summing those patterns of the same Doppler velocities; the result will be a set of diffraction patterns, each diffraction pattern belonging to one Doppler velocity bin;
4. extracts energy spectra of diffraction intensities at a number of diffraction peaks.

In the following we will discuss some details involved in this program, such as:

1. how do we transform a detector image to a diffraction pattern?
2. how to do proper normalization?
3. how to obtain energy spectra of diffraction intensities?

Conversion from Detector Coordinates to 2θ

A typical detector SAXI image is presented in Fig. 5.10, in which red curves mark the intersections of Bragg cones with the plane of the detector. To transform detector images into diffraction patterns, the first step is to determine the scattering angle for each pixel of the detector.

There are two coordinate systems involved in this problem (Fig. 5.11). Figure 5.11a is the z projection of the scattering geometry defined in Fig. 4.1; we call it the "external" coordinate

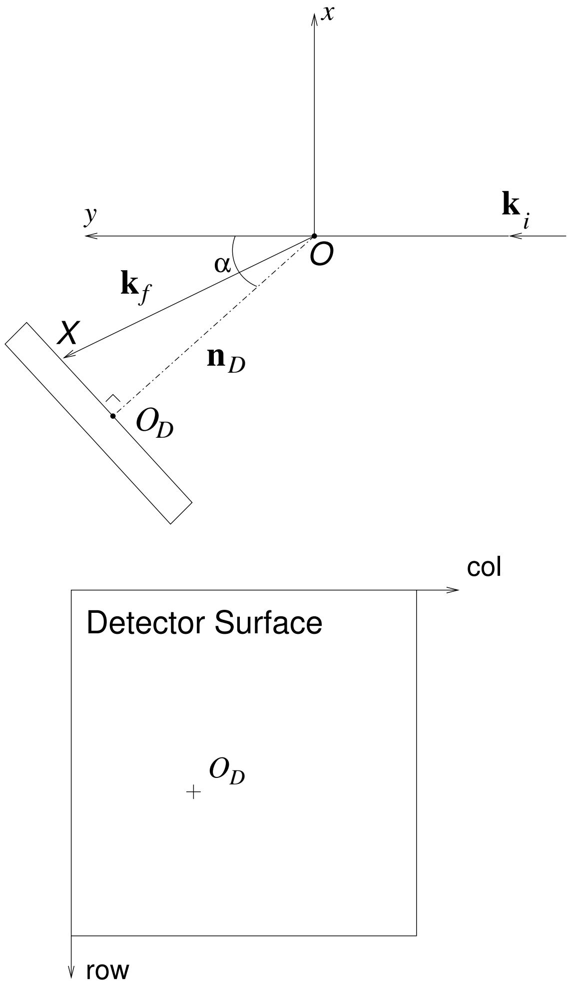

Figure 5.11: Geometry for determining the scattering angle, 2θ, of a detector pixel.

system. Figure 5.11b shows the 2D coordinate system of the detector surface seen from the front of the detector; we call it the "internal" coordinate system. Denote the normal of the detector surface toward the sample holder as $\mathbf{n}_D$, and define the angle α as

$$\alpha = \angle(\mathbf{e}_y, \mathbf{n}_D)$$

where $\mathbf{e}_y$ is the unit vector in the y direction. The point on the detector plane that is closest to the scattering center is denoted by O_D, and its detector coordinates are $(\mathrm{col}_0, \mathrm{row}_0)$. Then the position vector of a pixel X at (col,row) is given by

$$\begin{aligned} \overrightarrow{OX} &= \overrightarrow{OO_D} + \overrightarrow{O_DX} && (5.1) \\ \overrightarrow{O_DX} &= (l_x(\mathrm{col} - \mathrm{col}_0)\cos\alpha,\ l_x(\mathrm{col} - \mathrm{col}_0)\sin\alpha,\ -l_y(\mathrm{row} - \mathrm{row}_0)) && (5.2) \end{aligned}$$

where l_x and l_y are the width and the height of a pixel, respectively. Define h to be the distance between O_D and the origin of the external coordination system, O,

$$h = \overline{OO_D}$$

Then

$$\overrightarrow{OO_D} = (-h\sin\alpha,\ h\cos\alpha,\ 0) \tag{5.3}$$

The direction of the scatered wave vector is then

$$\hat{\mathbf{k}}_f = \frac{\overrightarrow{OX}}{OX} \tag{5.4}$$

The scattering angle, 2θ, to pixel X is then

$$2\theta = \arccos(\mathbf{e}_y \cdot \hat{\mathbf{k}}_f)\,. \tag{5.5}$$

Thus, the parameters involved in determining the scattering angle are

- α: angle between y direction and detector normal;
- h: distance $\overline{OO_D}$;
- $(\mathrm{col}_0, \mathrm{row}_0)$: position of detector center in the internal coordinate system;
- (l_x, l_y): dimension of a detector pixel.

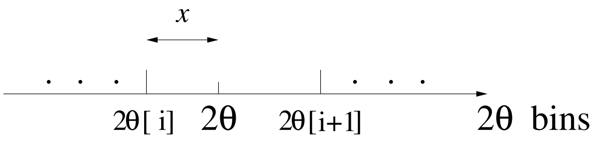

Figure 5.12: Data re-binning

Only the ratios $\frac{l_x}{h}$ and $\frac{l_y}{h}$ are relevant for determination of 2θ. For our Bruker detector, $l_x = l_y = l \approx \frac{100}{512}$mm, so we only need to find out the ratio of $\frac{h}{l}$ [7]. The angle α is linearly dependent on the goniometer position, α_g:

$$\alpha = \alpha_g + \delta\alpha \tag{5.6}$$

In summary, the assignment of a 2θ angle for each pixel requires three parameters: $\delta\alpha$, h/l, and $(\mathrm{col}_0, \mathrm{row}_0)$. With these, the scattering angle can be calculated from Eqs. 5.1-5.6.

Determination of Parameters The parameter $\delta\alpha$ can be obtained easily by positioning the detector directly in front of the beam to make $\alpha = 0$ and then $\delta\alpha$ is just the goniometer angle α_g. Using this method, we have obtained

$$\delta\alpha \approx -32^\circ$$

In the same setup we could estimate

$$(\mathrm{col}_0, \mathrm{row}_0) = (255.5, 315)$$

Since 10 cm on the detector corresponds to 512 pixels, and $h \approx 10$ cm, we obtain

$$\frac{h}{l} \approx 512$$

More precise results can be obtained from a calibration diffraction pattern.

Solid Angle The solid angle covered by a pixel at (col, row) is:

$$d\Omega = \frac{l_x l_y \left|\mathbf{k}_f \cdot \mathbf{n}_D\right|}{\left|\overline{OX}\right|^2} \tag{5.7}$$

Reduction of Data in a Detector Image

To obtain intensities of coherent elastic scattered photons, a detector image in a SAXI file needs to be transformed to a diffraction pattern. A rebinning procedure is needed to gather counts into 2θ bins. Since the detector is planar, the counts in one 2θ bin cannot be directly compared to another 2θ bin; the counts need to be normalized. We must keep track of the following quantities for each detector image:

- Doppler velocity (v, mm/s)
- exposure time (t, hour)
- source strength (Φ, mCi)
- counts at each pixel ($n[]$, 2D array)

These data should be transformed by rebinning to the data arrays

- Doppler velocity: $v[\,]$
- 2θ bins: $2\theta[\,]$
- counts at every 2θ bin: $cnts[\ ]$
- source_strength × exposure_time × solid_angle at every 2θ bin: $ses[\ ]$

The last quantity is the normalization factor, which includes three components: source strength, exposure time and solid angle, because

1. the solid-angle spanned by a pixel differs from that of pixels of different positions;
2. the data were taken over a period of several months and the source strength decays with a half-life of 270 days;
3. some velocity bins were given more exposure time to achieve better counting statistics.

The procedure of this transformation is:

1. for each pixel, calculate the scattering angle, 2θ, and the solid angle, $d\Omega$;

---

[7] which has the physical meaning: how many pixels equals h.

2. find (Fig. 5.12) in the array $2\theta[\,]$ the two 2θ bins that are closest to the value of 2θ of this pixel, $2\theta[i]$ and $2\theta[i+1]$, and calculate the fractional weight, x, of 2θ bin no. i,

$$x = \frac{2\theta - 2\theta[i]}{2\theta[i+1] - 2\theta[i]}\,;$$

3. add the number of counts at this pixel, n[the_pixel], and the value of source_strength × exposure_time × solid_angle, to the *cnts* and the *ses* arrays:

$$\begin{aligned}
cnts[i] &= cnts[i] + (1-x)\,n[\text{the\_pixel}] \\
cnts[i+1] &= cnts[i+1] + x\,n[\text{the\_pixel}] \\
ses[i] &= ses[i] + (1-x)\,\Phi t\,d\Omega \\
ses[i+1] &= ses[i+1] + x\,\Phi t\,d\Omega
\end{aligned}$$

Experimental Energy Spectra of Diffracted Intensities

A normalized diffraction pattern in a specified range is fit to a background and several Gaussian peaks. Then the background is subtracted from the diffraction pattern and the counts in each diffraction peak are integrated to get the diffracted intensity. The integrated intensities for each peak are plotted against the Doppler velocity to obtain the energy spectrum of diffracted intensity for this particular diffraction peak.

5.2.2 MDS

The program MDS calculates the energy spectrum of one diffraction peak according to the parameters of the input file “mds.in”. The simulation is done by applications of formulas presented in the previous two sections. The input parameters include material properties and experimental conditions:

1. external magnetic field: magnitude and direction
2. sample density, thickness
3. isotopic enrichment of the Mössbauer atom
4. description of atoms in a unit cell:
    (a) number of atoms

   (b) for each atom: atom species, position, weight, hyperfine magnetic field distribution (if applicable)

5. (hkl) and 2θ

The format of a “mds.in” file is presented in Appendix C.1.

5.2.3 MEF

This program is designed to obtain variables such as LRO/SRO parameters by fitting the theoretical diffraction energy spectra to the experimental ones. Theoretical results are calculated by program MDS, while the experimental ones are extracted from raw data by program GCSAXI. Parameters including those for scattering geometry, material properties, etc., are needed for the theoretical simulation program MDS as well as the program MEF. All parameters are supplied to program MEF by an input file “mef.in”. In this file, known parameters such as lattice parameters are constants, while unknown parameters such as LRO parameters are variables. A variable has an initial value, a maximum value, and a minimum value. The program MEF first generates a “mds.in” file according to the input template“mef.in” using all constants and the initial values of all variables, and calls the program MDS to calculate the energy spectra. It then compares the calculations to the experimental spectra. If the fit is inadequate, MEF will generate another “mds.in” with a new set of parameters for next round of compuation, and so on and so forth. The χ^2 minimization is done using a downhill simplex algorithm, because this algorithm does not require known functions to evaluate the partial derivatives of the target multi-dimensional function.

Chapter 6

Chemical Periodicities in Fe_3Al

This chapter presents the first study by Mössbauer powder diffractometry of the spatial arrangements of defect-related chemical environments in a material. The data cover both energy and momentum on an enriched $^{57}Fe_3Al$ polycrystalline sample. The long-range order of irregular ^{57}Fe chemical environments was measured and its origin explored by simulation and auxillary measurments.

We first give an overview of the candidate long-range orders for first-nearest-neighbor chemical environments of Fe atoms in Fe_3Al (section 6.1). Then we show how selected Mössbauer diffractions of Fe atoms with (0), (3) and (4) Al 1nn can demonstrate a basic capability of Mössbauer diffractometry measurments (section 6.3.1). The full energy spectrum of diffraction patterns is then presented (section 6.3.2). The intensities of fundamental diffractions are used as a test case for kinematical theory (section 6.4) and also a way to reveal the short range order (section 6.3.3). Energy spectra of superlattice diffraction orders are analyzed to give the long-range order of defect-related chemical environments (section 6.3.5). The origin of the B2 LRO for Fe atoms with (3) Al 1nn is explored with both simulations (sections 6.5.1 and 6.5.2) and transmission electron microscopy (TEM) (section 6.5.3). We find that the ^{57}Fe atoms with (3) Al 1nn environments have a high degree of simple cubic periodicity. This is consistent in part with antisite defects, but with the presence of some antiphase domain boundaries.

6.1 First-Nearest-Neighbor Environments for B2 and $D0_3$ Chemical Order

Fe_3Al with perfect $D0_3$ structure (Fig. 1.1) has two types of 1nn environments for Fe atoms — two-thirds of the Fe atoms have (4) Al 1nn atoms, and the other one-third has (0) Al 1nn atoms.

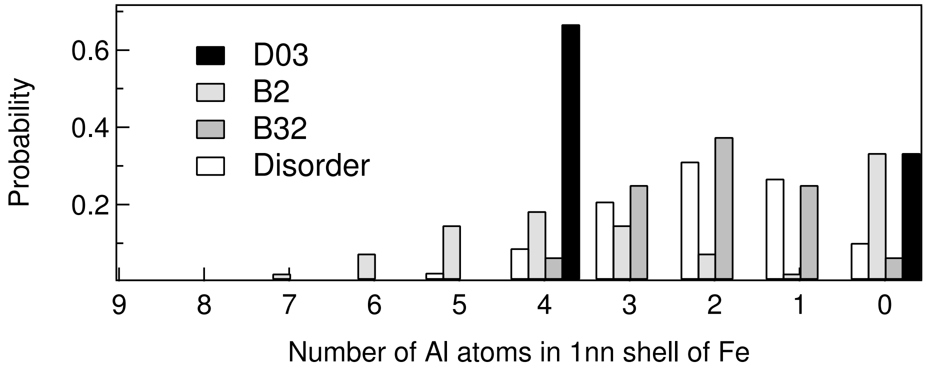

Figure 6.1: Distribution of Fe chemical environments for perfect A2, B2, D0_3, and B32 orders. (A reproduction of Fig. 1.3 of Ref. [25])

Although perfect B2 order requires an equiatomic composition, it is possible geometrically for Fe_3Al to have B2 order without D0_3 order if the Fe atoms are placed on the Fe sites of the B2 structure, and the Al atoms are mixed randomly with the remaining Fe atoms over the other sites (Fig. 1.5). The distribution of Fe atoms for this B2 ordered structure has a strong (0) Al 1nn peak superimposed on a binomial distribution centered about the (4) Al 1nn peak (Fig. 6.1).

The Fe atoms with (0) Al 1nn environments require the existence of only B2 order, and can be considered as antisite Fe atoms in a B2 structure (Fig. 1.5). With D0_3 chemical order, however, Fig. 1.1 shows that these Fe atoms are arranged as an fcc structure with a unit cell edge of twice the edge length of the bcc cube (γ sublattice). Note also from Fig. 1.1 that the Fe atoms having a (4) Al 1nn environment form a simple cubic (sc) arrangement. Experimental confirmation of this structural fact was published previously when Mössbauer diffraction patterns were measured by tuning the incident photons to nuclear resonances of ^{57}Fe atoms in (0) and (4) Al 1nn environments [57]. We confirmed this result in the course of the present work.

Other first-nearest-neighbor chemical environments exist for ^{57}Fe in an Fe_3Al alloy with imperfect chemical order. The (3) Al 1nn environment is characteristic of neither the D0_3 nor the B2 structures. In an alloy with partial disorder, the (3) Al 1nn environment could perhaps originate with Fe atoms on the α and β sublattices (Fig. 6.2), but having an extra Fe neighbor. It could also originate, perhaps, with Fe atoms in disordered zones on the bcc lattice, Fe atoms at antiphase domain boundaries or near local zones of B32 order, or with Fe atoms on the γ sublattice having an excess of Al 1nn atoms. In the present work we determined the source of order of this (3) Al 1nn environment.

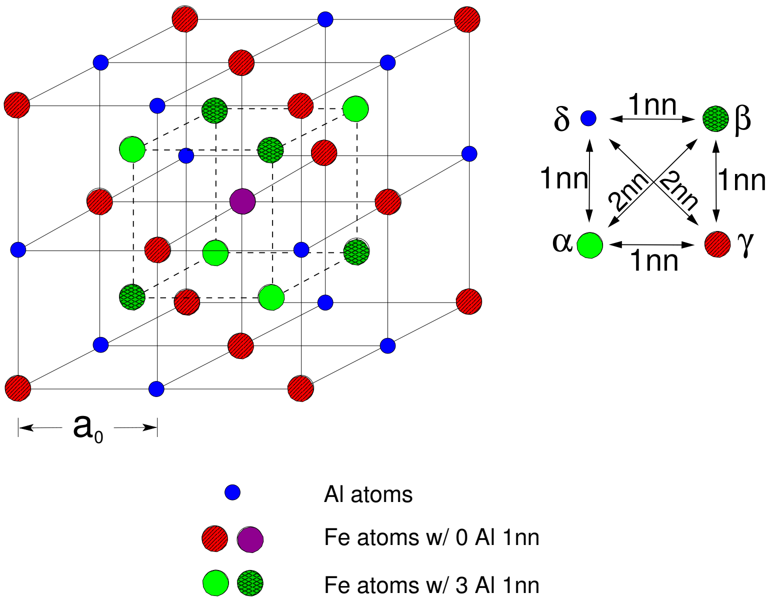

Figure 6.2: Fe atoms with (3) Al 1nn as a result of one antisite defect. An antisite defect (purple) is now in a δ-site. All iron atoms in its 1nn shell (green) now have 3 Al 1nn.

6.2 Experimental Details

The sample of Fe_3Al [1] was prepared from ^{57}Fe of 95% isotopic enrichment and 99.99% chemical purity, and Al metal of 99.999% chemical purity. These metals were processed by arc-melting, splat-quenching and cold-rolling, followed by an annealing for 100 h at 450 °C to develop $D0_3$ chemical order. A conventional conversion electron Mössbauer spectrum was acquired from this sample in constant acceleration mode. Conventional x-ray powder diffractometry was used to confirm a high degree of $D0_3$ LRO in the sample.

For Mössbauer diffractometry, the sample was about 10 mm×15 mm in area, and about 7 μm thick. To control the polarization factor of the diffraction intensities, a magnetic field of 3.3 kG was applied to the sample, oriented perpendicular to the scattering plane. The Doppler drive was operated in "constant velocity mode," and diffraction patterns were acquired at 89 velocities. For each velocity, the detector was rotated in steps of 0.4°, and in each step a detector image was acquired in the "frame buffer" computer for 4.5 hours. The intensities in a set of detector images in 5 steps (which cover the 2θ range of 40–79°) were transformed geometrically into a one-dimensional powder diffraction pattern (section 5.2.1). Longer acquisition times (for better statistics) were used

---

[1] This was the same sample used by Tab Stephens. More details about the sample can be found in his thesis [56].

for velocities between 1.9–4.9 mm/s because the calculations described in Section 6.3 indicated that the diffraction intensities in this region would be most sensitive to the periodicities of the different chemical environments. All diffraction patterns were normalized to incident flux, with units of counts/sr/(mCi·hour).

For all diffraction patterns at each Doppler velocity, Bragg diffraction peaks were identified, and peaks in the 2θ range of 40–70° were fit to a background curve and several Gaussian functions. Background was then removed and the counts in each peak were integrated over two characteristic widths on each side of the peak. The integrated counts were plotted against velocity to obtain nuclear resonance energy spectra of the Bragg diffractions.

6.3 Diffraction Patterns and Determination of Long-Range Order

6.3.1 Chemical Environment Selective Mössbauer Diffraction Patterns

As already pointed out in Chapter 1, tuning the resonance between an incident γ-ray and a ^{57}Fe nucleus provides a means for altering the amplitude and phase of the scattering factor of the ^{57}Fe atom. Resonances occur at different Doppler velocities for ^{57}Fe atoms in different chemical environments (see Fig. 1.4 and 2.6), so we can emphasize the diffraction from ^{57}Fe nuclei in different chemical environments by appropriate selection of the Doppler velocity.

To illustrate the basic amplitude dependence, the following velocities (in mm/s) were used to emphasize the (n) chemical environments: 4.22 for the (3) environment; 3.72 for the (4) environment; 5.00 for the (0) environment; and 7.85 for the off-resonance condition. Figure 6.3 presents Mössbauer diffraction patterns measured at these velocities. The crystallographic texture of the foil sample makes it impossible to compare the intensities of different diffraction peaks (the (220) fundamental diffraction is absent at $2\theta = 49.7°$, for example), but it is appropriate to examine how the peak intensities change with resonance condition. The diffraction pattern from the (4) Al 1nn environment shows a relatively strong intensity at the position of the degenerate superlattice diffractions (300), (221) at $2\theta = 53.0°$, as expected for its sc periodicities in the B2 structure. The (0) Al 1nn environment shows enhanced intensity in the $(\frac{3}{2}\frac{3}{2}\frac{3}{2})$, $(\frac{5}{2}\frac{1}{2}\frac{1}{2})$ diffraction at $2\theta = 45.5°$ and the $(\frac{5}{2}\frac{3}{2}\frac{3}{2})$ diffraction at $2\theta = 58.4°$.[2] These superlattice diffractions from the large fcc periodicities in the D0$_3$ structure are less evident in the diffraction pattern obtained by tuning to Fe atoms with the (4) Al 1nn environment. These effects around 45.5°, 53.0°, 58.4°, and perhaps the other weaker

---

[2] It may be helpful to refer to Fig. 1.1 and 1.2.

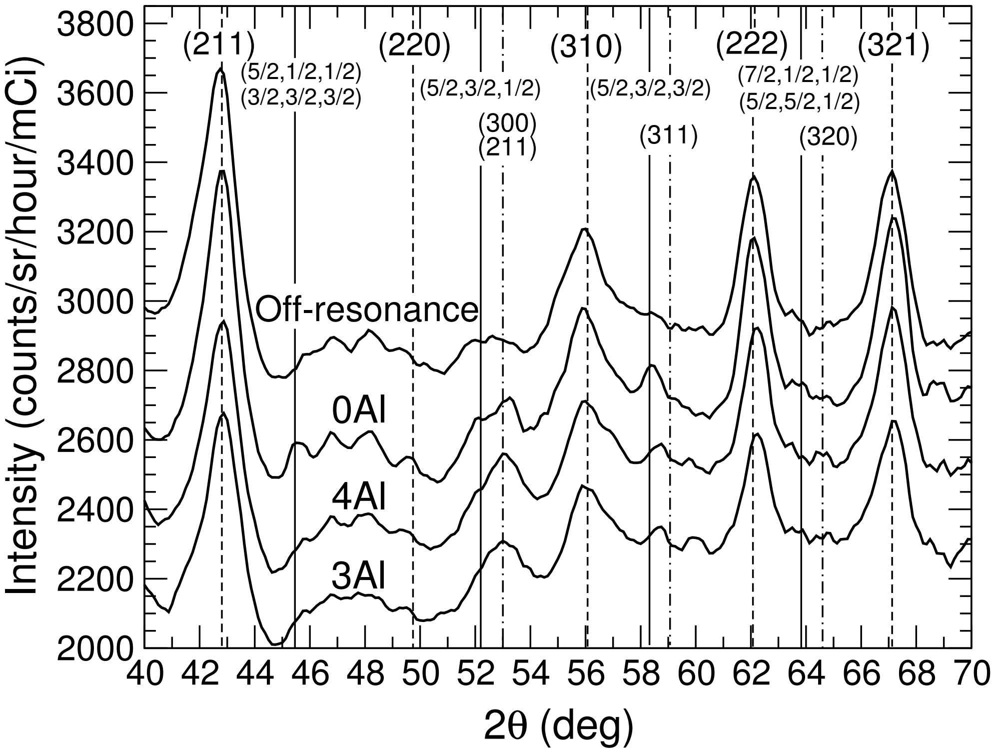

Figure 6.3: Four Mössbauer diffraction patterns from Fe_3Al. Variations in detector sensitivity are responsible for much of the background variations.

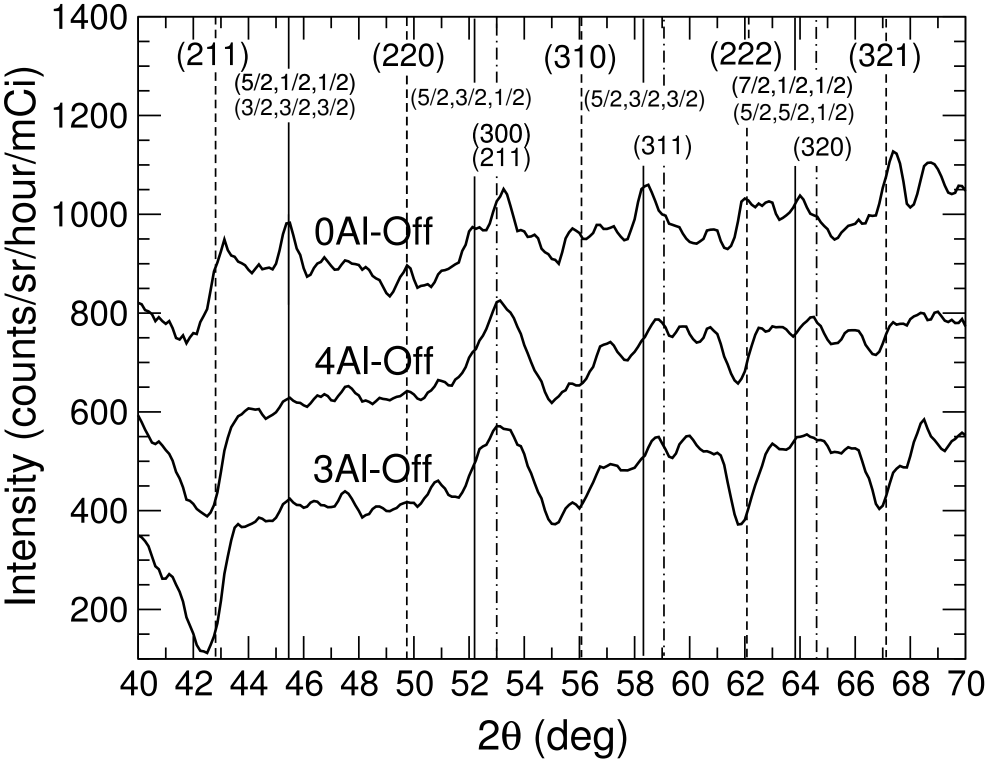

Figure 6.4: Difference of the Mössbauer diffraction patterns of figure 6.3 for (0), (4) and (3) environments and off-resonance diffraction pattern.

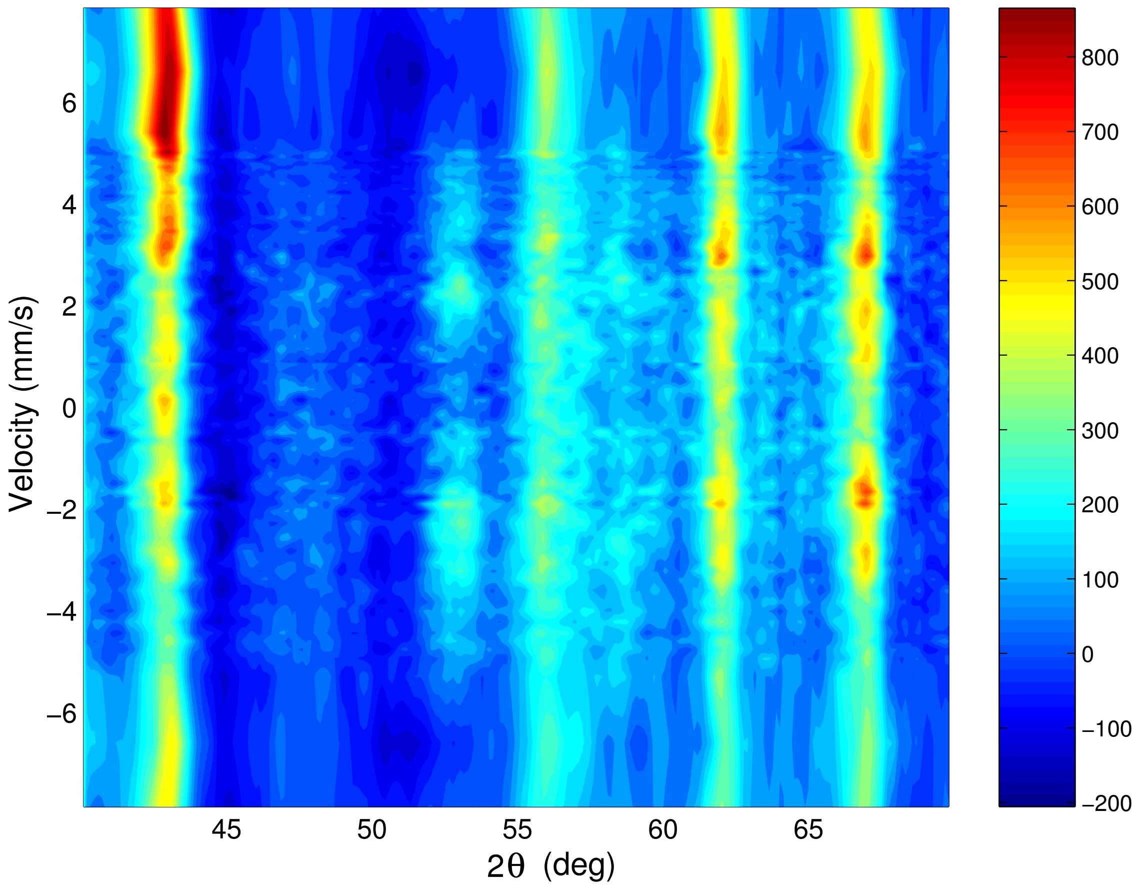

Figure 6.5: Mössbauer diffraction patterns from $^{57}Fe_3Al$, taken at 89 velocities arranged vertically. Data were normalized by incident flux, and background was subtracted.

superlattice diffractions are more evident in Fig. 6.4, which presents the differences between the (0), (3) and (4) Al 1nn resonance tuning and the off-resonance tuning.[3] Note that the difference involving the (3) Al 1nn environment is rather similar to that of the (4) Al 1nn environment.

6.3.2 Energy Spectra of Mössbauer Diffraction Patterns

The phase of the scattering factor varies strongly across each nuclear resonance, so much more information is available if diffraction patterns are acquired over a full spectrum of energies (not just the four used for the previous example). Those more complete data are presented in Fig. 6.5 and were the main data used in our investigation.

---

[3] The residual intensities around the fundamental peaks should not be zero, owing to interference effects between x-ray and nuclear scattering.

Table 6.1: Parameters needed for all MDS and MEF calculations.

External Magnetic Field (Telsla)	0.33
Direction of Ext. Magnetic Field	(0,0,1)
Sample density (number of unit cells in 1 cubic meter)	0.0517×10^{29}
Sample thickness (μm)	7
Enrichment of ^{57}Fe	90%

Table 6.2: First-nearest-neighbors chemical environments in partially-ordered Fe_3Al.

	(0,1) Al	(2) Al	(3) Al	(4)Al	(5) Al
CEMS Spectra	0.290	0.116	0.138	0.388	0.025
Monte-Carlo Simulation	0.335	0.050	0.146	0.374	0.087
Diffraction Spectra	0.248	0.132	0.110	0.373	0.083

6.3.3 Intensities of bcc Fundamental Diffractions

The energy spectra of fundamental bcc diffraction peaks are presented in Fig. 6.6 with calculated results obtained from kinematical diffraction theory.

The intensities of fundamental diffraction peaks do not depend on long-range chemical order (LRO) on the bcc lattice, but they do depend on the short-range order (SRO) of the local chemical environments of ^{57}Fe. The reason is that all atoms scatter photons coherently in this case.

The diffraction intensities given by Eqs. 4.38 and 4.39 are related to scattering differential cross section, $\frac{d\sigma}{d\Omega}$. For the fundamental diffraction peaks, we have

$$\frac{d\sigma}{d\Omega} = \left| f^{\mathrm{Al}} c^{\mathrm{Al}} + \sum_{n=0}^{8} f^{(n)} c^{(n)} \right|^2 = \left| \sum_{n=-1}^{8} f^{(n)} c^{(n)} \right|^2 , \tag{6.1}$$

where f^{Al} and $f^{(n)}$ denote the scattering factors for Al atoms and Fe atoms with (n) Al 1nn, respectively. For simplicity in the expression at right, we use the index $n = -1$ for Al atoms. The total concentration of the (n) environment is $c^{(n)}$, normalized so that $\sum_n c^{(n)} = 1$. The scattering factor of an Fe^{57} atom with (n) Al 1nn and hyperfine magnetic field H, $f^{(n)}(H)$, is given by Eqs. 4.12 and 4.8 in Chapter 4 . For $0 \leq n \leq 8$, the total scattering factor $f^{(n)}$ is integrated over all

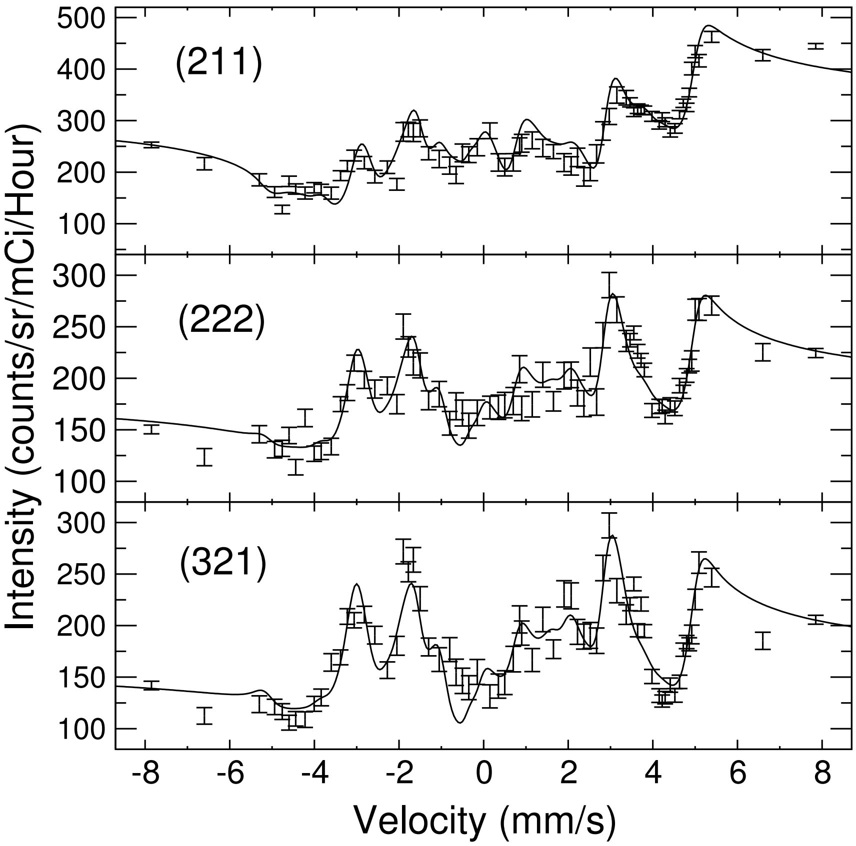

Figure 6.6: Full energy spectra of (211), (222) and (321) diffraction intensities from Fe_3Al, including kinematical theory calculations and experimental data.

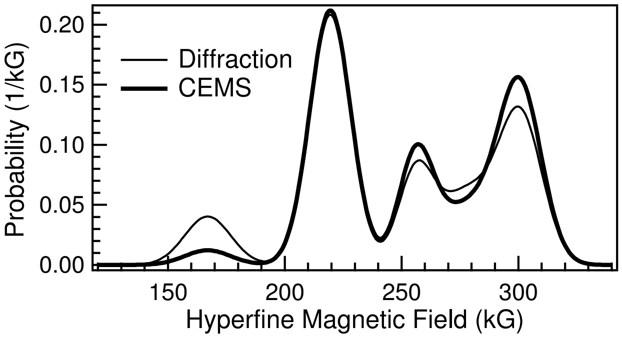

Figure 6.7: Hyperfine magnetic field distribution obtained from energy spectra of (211), (222) and (321) diffraction intensities of figure 6.6 compared to HMF distribution obtained by CEMS.

atoms with different HMFs but the same number of Al first-nearest neighbors:

$$f^{(n)} = \int p^{(n)}(H)\, f^{(n)}(H)\, dH \ , \tag{6.2}$$

where $p^{(n)}(H)$ is a Gaussian function with center $H_0^{(n)}$, width $w^{(n)}$ and area 1.

The parameters $c^{(n)}$, $H_0^{(n)}$ and $w^{(n)}$ were obtained by fitting the measured energy spectra of fundamental diffraction peaks to Eq. 6.1 using a least squares procedure (including the electronic scattering factor for Al atoms) implemented in the program MEF (see section 5.2.3).

Details of the fitting procedure The simulations require inputs of material properties and experimental conditions. Parameters that are common in all simulations described in this chapter are presented in Table 6.1. In addition to these common parameters, we need parameters describing atoms in a unit cell. The results from conversion electron Mössbauer spectrometry (CEMS) measurement (Table 6.2) were used as an initial guess for some of the fitting parameters, and the concentration of Al, $c^{(-1)}$, was set to 0.25. The concentrations of Fe atoms with different chemical environments, $c^{(0)}$ through $c^{(5)}$, were adjustable parameters in the fitting, although normalization reduced to five the number of degrees of freedom. The concentrations $c^{(6)}$ through $c^{(8)}$ were set to zero as found by conventional Mössbauer spectrometry.

Figure 6.6 presents the energy spectra of the Mössbauer diffraction peaks (211), (222) and (321), and the results calculated by fitting with HMF distributions. As SRO information, this HMF distribution reflects directly the numbers of Fe atoms with various numbers of 1nn Al atoms (Table 6.2). The final result is an HMF distribution $\sum_n c^{(n)} p^{(n)}(H)$. Figure 6.7 shows that this HMF distribution differs from that of the CEMS spectrum of Fig. 1.4, probably because the diffraction measurement samples different depths in the sample. Note that short-range order data were obtained

Table 6.3: Phase factors for the four fcc sublattices in the D0_3 structure for (100)-type and $(\frac{1}{2}\frac{1}{2}\frac{1}{2})$-type diffractions.

	α	γ	β	δ
(100)	1	-1	1	-1
$(\frac{1}{2}\frac{1}{2}\frac{1}{2})$	1	i	-1	-i

from the measured energy spectra of fundamental diffractions. This is a feature unique to Mössbauer diffractometry that is impossible with x-ray diffractometry, for example.

6.3.4 Intensities of Superlattice Diffractions

For the D0_3 structure there are two types of superlattice diffractions: (100)-type for sc periodicities and $(\frac{1}{2}\frac{1}{2}\frac{1}{2})$-type for fcc periodicities. The energy spectra for these two diffraction peaks are presented in Fig. 6.8 with calculation results.

The scattering factors for superlattice diffractions include a phase factor for each of the four fcc sublattices of the D0_3 structure as listed in Table 6.3. For Mössbauer diffraction we define order parameters for each chemical environment (n) in terms of the concentration of the chemical environment on each sublattice. For example, the concentration of a chemical environment (n) on the α sublattice is $c_\alpha^{(n)}$. The two types of LRO parameters are

$$\eta_{\text{sc}}^{(n)} = \frac{c_\alpha^{(n)} + c_\beta^{(n)} - c_\gamma^{(n)} - c_\delta^{(n)}}{c^{(n)}} \,, \tag{6.3}$$

and

$$\eta_{\text{fcc}}^{(n)} = \frac{c_\alpha^{(n)} - c_\beta^{(n)} + \mathrm{i}\,(c_\gamma^{(n)} - c_\delta^{(n)})}{c^{(n)}} \,. \tag{6.4}$$

The quantity $\eta_{\text{sc}}^{(n)}$ is a measure of the B2 order between two sc sublattices ($\delta + \gamma$ vs. $\alpha + \beta$), while the real and imaginary parts of $\eta_{\text{fcc}}^{(n)}$ are measures of LRO between two pairs of fcc sublattices (δ vs. γ and α vs. β). Parameters $\eta_{\text{sc}}^{(n)}$ and $\eta_{\text{fcc}}^{(n)}$ combined with the total concentration $c^{(n)}$ give all information about the sublattice occupancy of the chemical environment (or atomic species), (n),

$$\begin{aligned}
c_\alpha^{(n)} &= \frac{1}{4}\,c^{(n)}\left(1 + \eta_{\text{sc}}^{(n)} + 2\mathrm{Re}\left[\eta_{\text{fcc}}^{(n)}\right]\right) \,, \\
c_\beta^{(n)} &= \frac{1}{4}\,c^{(n)}\left(1 + \eta_{\text{sc}}^{(n)} - 2\mathrm{Re}\left[\eta_{\text{fcc}}^{(n)}\right]\right) \,, \\
c_\gamma^{(n)} &= \frac{1}{4}\,c^{(n)}\left(1 - \eta_{\text{sc}}^{(n)} + 2\mathrm{Im}\left[\eta_{\text{fcc}}^{(n)}\right]\right) \,,
\end{aligned} \tag{6.5}$$

Table 6.4: LRO parameters for prominent chemical environments of Fe and Al.

^{57}Fe Environment	$\eta_{\rm sc}^{(n)}$	Im$\left[\eta_{\rm sc}^{(n)}\right]$	Re$\left[\eta_{\rm sc}^{(n)}\right]$	$c^{(n)}$
(0) Al 1nn	-0.98±0.01	0.98±0.25	-0.00±0.31	0.16±0.01
(1) Al 1nn	-0.81±0.45	0.51±0.80	-0.09±0.70	0.03±0.01
(2) Al 1nn	-0.35±0.13	0.61±0.45	-0.29±0.55	0.10±0.01
(3) Al 1nn	0.59±0.05	-0.20±0.45	-0.18±0.44	0.09±0.01
(4) Al 1nn	1.00±0.01	0.00±0.01	-0.02±0.27	0.28±0.01
(5) Al 1nn	0.87±0.10	-0.07±0.70	0.93±1.18	0.06±0.01
Al atom	-0.70±0.20	-0.80±0.30	-0.01±0.35	0.25

$$c_{\delta}^{(n)} = \frac{1}{4}\, c^{(n)} \left(1 - \eta_{\rm sc}^{(n)} - 2{\rm Im}\left[\eta_{\rm fcc}^{(n)}\right]\right) .$$

The intensities of the (100)-type and $(\frac{1}{2}\frac{1}{2}\frac{1}{2})$-type superlattice diffractions are related to:

$$\frac{d\sigma}{d\Omega}_{(100)} = \left|\sum_n f^{(n)} c^{(n)} \eta_{\rm sc}^{(n)}\right|^2 , \tag{6.6}$$

$$\frac{d\sigma}{d\Omega}_{(\frac{1}{2}\frac{1}{2}\frac{1}{2})} = \left|\sum_n f^{(n)} c^{(n)} \eta_{\rm fcc}^{(n)}\right|^2 . \tag{6.7}$$

Care must be taken when we evaluate Eq. 6.7, considering the possibilities that there are domains with preference of Al atoms for different fcc sublattice. This consideration can be accounted for by a slight modification of Eq. 6.7 to

$$\frac{d\sigma}{d\Omega}_{(\frac{1}{2}\frac{1}{2}\frac{1}{2})} = \frac{1}{2}\left\{\left|\sum_n f^{(n)} c^{(n)} \eta_{\rm fcc}^{(n)}\right|^2 + \left|\sum_n f^{(n)} c^{(n)} \left[\eta_{\rm fcc}^{(n)}\right]^*\right|^2\right\} . \tag{6.8}$$

The measured diffraction energy spectrum of $I_{(100)}$ can be fitted to Eq. 6.6 to obtain parameters $\eta_{\rm sc}^{(n)}$, and the $\eta_{\rm fcc}^{(n)}$ can be obtained from the diffraction energy spectrum of $I_{(\frac{1}{2}\frac{1}{2}\frac{1}{2})}$. The normalization conditions for these two parameters are $\sum_n c^{(n)}\eta_{\rm sc}^{(n)} = 0$ and $\sum_n c^{(n)}\eta_{\rm fcc}^{(n)} = 0$, assuming there are neither vacancies nor impurities in the alloy.

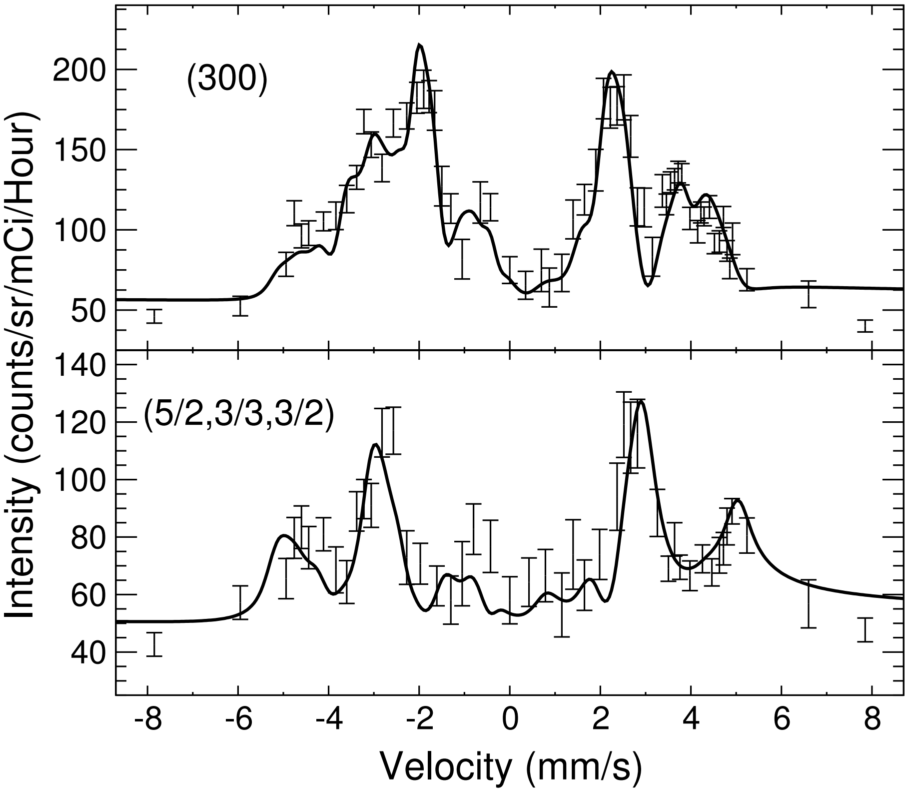

Figure 6.8: Full energy spectra of (300) and $(\frac{5}{2}\frac{3}{2}\frac{3}{2})$ diffraction intensities from Fe_3Al, including kinematical theory calculations and experimental data.

6.3.5 Long-Range Order

Using the fitting procedure described in the previous section, we determined the simple-cubic and the face-centered cubic long-range order of the different chemical environments for ^{57}Fe atoms. Using the HMF distribution obtained from fundamental diffraction peaks, the superlattice diffraction energy spectra were fitted using $\eta_{\mathrm{sc}}^{(n)}$ and $\eta_{\mathrm{fcc}}^{(n)}$ as adjustable parameters. Figure 6.8 presents the experimental data and calculated energy spectra of peaks (300) and $(\frac{5}{2}\frac{3}{2}\frac{3}{2})$. Order parameters providing the best fit are listed in Table 6.4. Error bars were estimated from the covariance matrix.

Simple Cubic Periodicities

The superlattice diffraction intensities are quite sensitive to B2 order parameters. This is due in part to the strong phase differences between scattering factors of different chemical environments. To show the sensitivity of the diffraction energy spectra to the order parameters $\eta_{\mathrm{sc}}^{(n)}$, various simulated energy spectra of superlattice diffractions are presented in Fig. 6.9. The energy spectrum of the (300) diffraction is very sensitive to the B2 order of Fe atoms with (0) or (4) Al 1nn. The (0) and (4) Al 1nn environments have very strong B2 order. The B2 order of (3) Al 1nn environments influence the energy spectrum in the velocity range of 4–5 mm/s, which was emphasized in our measurements.

Figure 6.9(c) shows that (3) Al chemical environments have partial B2 order. This order parameter of $\eta_{\mathrm{sc}}^{(3)} = 0.6$ drew our attention since a naive thought would be that a chemical environment related to disruption of order should be disordered. This is discussed further below. Table 6.4 shows a significant amount of B2 order of Fe atoms in the (1) Al 1nn environments. This is plausible because Fe atoms on δ or γ sites can have the (1) Al 1nn environment if there is one adjacent antisite defect on either α or β sites. This differs from Fe atoms on α and β sites, which require three antisite defects on δ sites. The result for (1) Al 1nn environments suffers from large error bars, however, because it is hard to distinguish the (1) Al 1nn environment from the (0) Al 1nn environment. The (2) Al 1nn environments also have some B2 order, similar to (0) and (1) Al 1nn environments, and the (5) Al environments show strong B2 order similar to (4) Al 1nn environments.

Face-Centered Cubic Order Parameters

The analysis of the energy spectrum of the $(\frac{5}{2}\frac{3}{2}\frac{3}{2})$ diffraction is similar, but more difficult. The calculated energy spectrum was still sensitive to the long-range order of (0) and (4) Al 1nn environments (Fig. 6.10a and b). However, it had only weak sensitivity to the parameter $\eta_{\mathrm{fcc}}^{(n)}$ for the minor chemical environments, for example, the (3) Al 1nn environment (Fig. 6.10c and d). The errors for these fcc order parameters are large in Table 6.4. The insensitivity of diffraction intensities to fcc

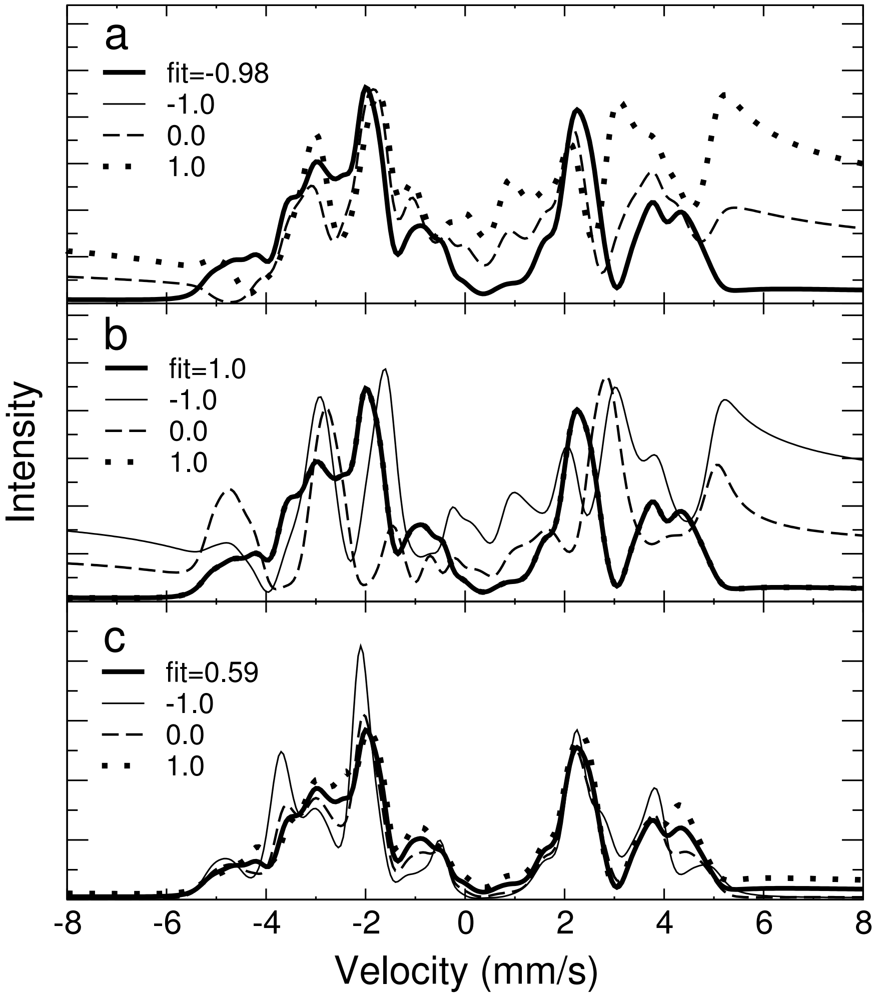

Figure 6.9: Sensitivity of simulated energy spectra of (300) diffraction peak to variations of LRO parameter η_{SC} for (a) Fe atoms with (0) Al 1nn, (b) Fe atoms with (4) Al 1nn, and (c) Fe atoms with (3) Al 1nn. The thick lines are the best fit to experimental data with $\eta_{\mathrm{sc}}^{(0)} = -0.98$, $\eta_{\mathrm{sc}}^{(4)} = 1.0$ and $\eta_{\mathrm{sc}}^{(3)} = 0.59$. Some lines are invisible due to overlap with curves of the best fit: the thin line with $\eta_{\mathrm{sc}}^{(0)} = -1.0$ in (a), and the dotted line with $\eta_{\mathrm{sc}}^{(4)} = 1.0$ in (b).

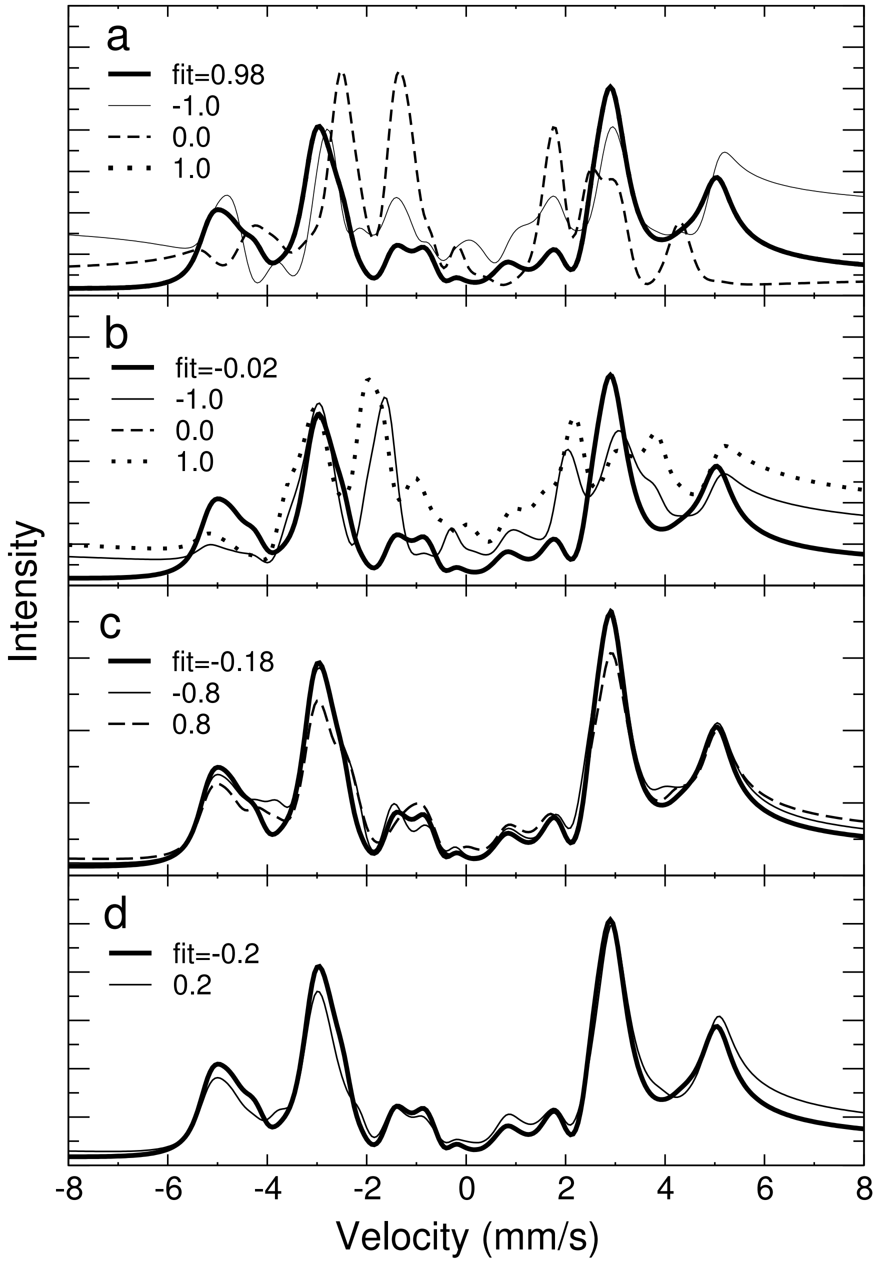

Figure 6.10: Sensitivity of simulated energy spectra of $(\frac{5}{2}\frac{3}{2}\frac{3}{2})$ diffraction peak to variations of LRO parameters $\eta_{\rm fcc}$: (a) $\mathrm{Im}[\eta^{(0)}_{\rm fcc}]$, (b) $\mathrm{Re}[\eta^{(4)}_{\rm fcc}]$, (c) $\mathrm{Re}[\eta^{(3)}_{\rm fcc}]$, and (d) $\mathrm{Im}[\eta^{(3)}_{\rm fcc}]$. The thick lines are the best fit to experimental data.

Table 6.5: Concentration of chemical environments on the four fcc sublattices (experimental)

^{57}Fe Environment	δ	α	γ	β
(0) Al 1nn	0.001 ± 0.020	0.001 ± 0.024	0.155 ± 0.030	0.001 ± 0.024
(1) Al 1nn	0.006 ± 0.014	0.000 ± 0.010	0.020 ± 0.019	0.003 ± 0.011
(2) Al 1nn	0.003 ± 0.023	0.002 ± 0.028	0.063 ± 0.029	0.030 ± 0.030
(3) Al 1nn	0.019 ± 0.023	0.028 ± 0.023	0.000 ± 0.021	0.044 ± 0.025
(4) Al 1nn	0.000 ± 0.002	0.137 ± 0.043	0.000 ± 0.002	0.143 ± 0.043
(5) Al 1nn	0.004 ± 0.023	0.058 ± 0.046	0.000 ± 0.022	0.000 ± 0.037
Al atom	0.206 ± 0.040	0.017 ± 0.046	0.006 ± 0.040	0.020 ± 0.046

order is due in part to the lack of global preference of Al atoms for one specific fcc sublattice in polycrystalline sample, indicated by Eq. 6.8, which smears out some of the interference effects that are essential for the sensitivity of Mössbauer Diffractometry to long-range order.

6.3.6 Distribution of Chemical Environments on Four fcc Sublattices

Table 6.5 presents the sublattice concentrations of all prominent chemical environments of Fe and that of Al. These concentrations were obtained from values of $c^{(n)}$, $\eta_{\rm sc}^{(n)}$ and $\eta_{\rm fcc}^{(n)}$ in Table 6.4 and defining the Al-rich sublattice as the δ sublattice. Iron atoms with (0), (1), and (2) Al neighbors are mostly on the γ sublattice, while those with (3), (4) and (5) Al neighbors are mostly on the α and β sublattices. These results for the (0) and (4) Al environments are as expected from the geometry of the $D0_3$ structure shown in Fig. 1.1, but the results for the other environments are not obvious *a-priori*.

The existence of B32 order would involve an imbalance of Fe occupancies on the α and β sublattices. It is not impossible for B32 order to be stronger for some chemical environments than others, but within the statistical quality of the present data we have no evidence for B32 order for any of the chemical environments.

6.4 Is Kinematical Diffraction Theory Good Enough?

Figure 6.11 shows the measured energy spectra of the fundamental (211) Bragg diffractions. The experimental spectrum is shown at the top of Fig. 6.11 with calculated results obtained from kinematical theory. The energy spectrum calculated with the kinematical theory agrees well with

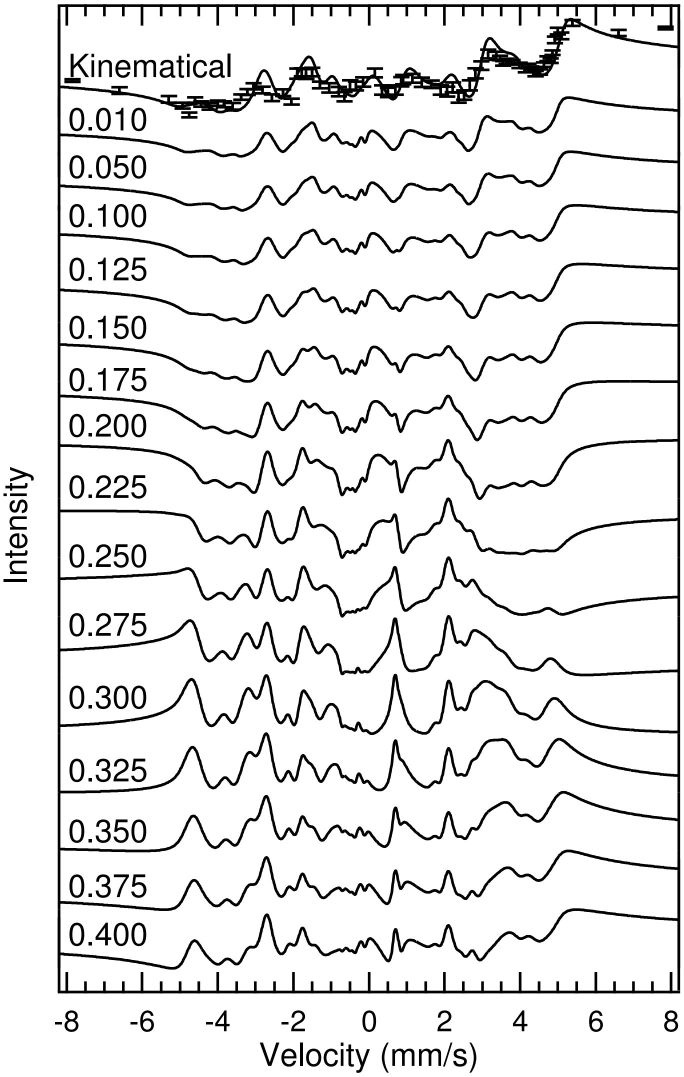

Figure 6.11: Energy spectra of Mössbauer diffraction peak (211) of Fe_3Al calculated by the polycrystalline adaptation of CONUSS, labeled with values of ζ (unit: μm), the characteristic size of crystallites.

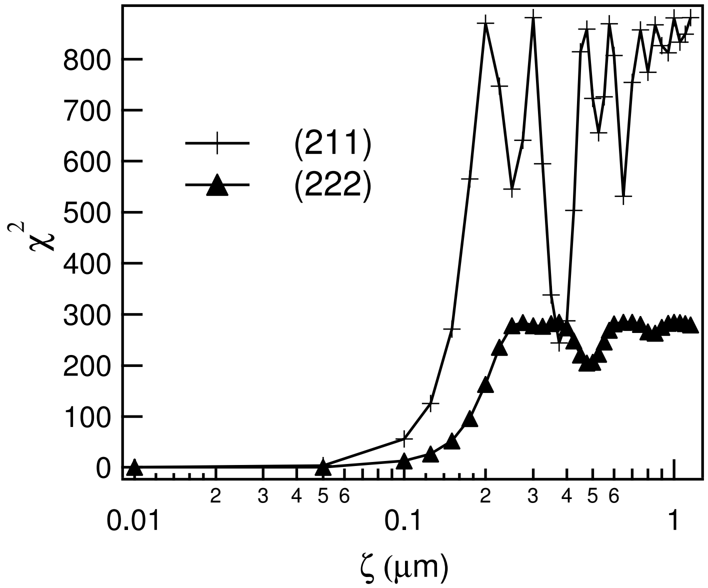

Figure 6.12: Values of χ^2 for the best fit to experimental spectra by the polycrystalline adaptation of CONUSS, plotted against crystal thickness parameter ζ.

the experimental data.

To identify the effects expected from dynamical diffraction, calculations were performed with our polycrystalline adaptation of the CONUSS software (section 4.7). The characteristic crystallite size, ζ, was treated as a free parameter. Parameters x_p and x_i play minor roles in the shape of diffraction energy spectrum, provided that x_p is small. (For the (211) peak, the calculated spectrum with $x_p = 10\%$ is nearly identical to the spectra with $x_p = 1\%$ or $x_p = 0.1\%$.) In the following discussion, all calculations were performed with $x_p = 1\%$. Calculated energy spectra for the (211) diffraction peak with various values of ζ are also presented in Fig. 6.11. Calculations with small ζ agree well with the kinematical spectrum, although calculations for large ζ do not.

A comparison between these calculated dynamical intensities and the experimental (211) and (222) diffraction intensities is presented quantitatively in Fig. 6.12. For each value of ζ, the calculated energy spectrum of diffraction intensity was fit to the measured data by vertical scaling. The statistical χ^2 from the fitting is plotted against ζ in Fig. 6.12. For both (211) and (222) peaks, χ^2 is a minimum in the kinematical limit (ζ=0) of the full dynamical calculations. It is interesting that the fits to the dynamical theory have an oscillating component, with minima in the fitting at intervals of about 0.4 μm for the (211) diffraction and about 0.5 μm for the (222) diffraction. This

Table 6.6: Relative superlattice diffraction intensities of chemical environments in Monte-Carlo simulated Fe_3Al.

	(0)	(1)	(3)	(4)	(5)
$I_{(100)}/I_{(110)}$	0.99	0.75	0.95	0.99	0.99
$I_{(\frac{1}{2}\frac{1}{2}\frac{1}{2})}/I_{(110)}$	0.72	0.20	0.00	0.00	0.00

probably originates with a pendellösung of dynamical theory.

For our sample, kinematical calculations are appropriate for interpreting the Mössbauer diffraction data.

6.5 B2 LRO of Fe Atoms with (3) Al 1nn

In this section we seek to determine the structure(s) responsible for the partial sc order of Fe atoms with (3) Al 1nn. We first describe an important tool: Monte-Carlo simulations of ordering kinetics with a vacancy mechanism, which is capable of producing chemical order with domains. A separate type of simulation of "homogeneous disorder" was also performed by random interchanges of pairs of atoms. It is found that homogeneous disorder cannot account for the experimental results. The anti-phase boundaries in partially-ordered structure are found to be important, and transmission electron microscopy is used to confirm this.

6.5.1 Environment-Sensitive Diffraction Intensities from Monte-Carlo Simulations

We constructed a bcc alloy on a computer with chemical order to match the probabilities of the 1nn chemical environments listed in Table 6.2. This was done with a Monte-Carlo algorithm [4] where a vacancy moved by first-nearest-neighbor jumps through a bcc alloy that was initially disordered chemically [22, 44]. Chemical interactions between 1nn and 2nn pairs of atoms were set at $V_{1\mathrm{Al-Al}} = 1.1$, $V_{1\mathrm{Fe-Fe}} = 1.1$, $V_{1\mathrm{Fe-Al}} = 0.0$, $V_{2\mathrm{Al-Al}} = 1.1$, $V_{2\mathrm{Fe-Fe}} = 0.0$, $V_{2\mathrm{Fe-Al}} = 0.0$, in units of $k_{\mathrm{B}}T$. The simulation was stopped when the alloy possessed the 1nn chemical environments of Table 6.2, and had a high degree of $D0_3$ LRO, consistent with the conventional x-ray diffraction pattern.

---

[4] The program was written by L. Anthony.

Table 6.7: Superlattice diffraction intensities of chemical environments in Monte-Carlo simulated Fe_3Al.

	(0) Al	(1) Al	(3) Al	(4) Al	(5) Al
$V_{1\mathrm{Al-Al}} = V_{1\mathrm{Fe-Fe}} = V_{2\mathrm{Fe-Fe}} = 1.1$					
$\sqrt{I_{(100)}/I_{(110)}}$	1.00	0.85	**0.94**	1.00	1.00
$\sqrt{I_{(\frac{1}{2}\frac{1}{2}\frac{1}{2})}/I_{(110)}}$	0.84	0.44	0.17	0.07	0.17
$V_{1\mathrm{Al-Al}} = V_{1\mathrm{Fe-Fe}} = 0.91, V_{2\mathrm{Al-Al}} = V_{2\mathrm{Fe-Fe}} = 0.807$					
$\sqrt{I_{(100)}/I_{(110)}}$	1.00	0.88	**0.90**	1.00	1.00
$\sqrt{I_{(\frac{1}{2}\frac{1}{2}\frac{1}{2})}/I_{(110)}}$	0.93	0.65	0.16	0.00	0.20
$V_{1\mathrm{Al-Al}} = V_{1\mathrm{Fe-Fe}} = 1.0, V_{2\mathrm{Al-Al}} = 2.0$					
$\sqrt{I_{(100)}/I_{(110)}}$	1.00	0.96	**0.97**	1.00	1.00
$\sqrt{I_{(\frac{1}{2}\frac{1}{2}\frac{1}{2})}/I_{(110)}}$	0.95	0.73	0.13	0.00	0.16

Within this simulated alloy, we identified all Fe atoms having different numbers of 1nn Al atoms. For example, we found the coordinates, $\{\mathbf{r}_3\}$, of all Fe atoms with the (3) Al 1nn environment. We set the scattering factor of these Fe atoms to 1, all others to zero, and calculated the scattering factor

$$\psi_3(\Delta\mathbf{k}) = \sum_{\mathbf{r}_3} \mathrm{e}^{\mathrm{i}\Delta\mathbf{k}\cdot\mathbf{r}_3} \; . \tag{6.9}$$

We obtained the diffracted intensity from the Fe atoms with this (3) Al 1nn environment as $I_3(\Delta\mathbf{k}) = |\psi_3(\Delta\mathbf{k})|^2$. The same procedure was used for the diffracted intensities of other chemical environments, the (0) and (4) Al 1nn environments, I_0 and I_4, for example. As expected from the arrangements of these two Fe sites in Fig. 1.1, the intensity I_0 showed a family of $(\frac{1}{2}\frac{1}{2}\frac{1}{2})$ diffraction peaks plus the (100) family, whereas I_4 showed only the (100) family. Interestingly, the calculated intensity I_3 showed the (100) family of diffractions, and their intensities were strong. When this intensity was normalized to the number of Fe atoms with the (3) Al 1nn environment, the calculated intensity of I_3 was 95% of I_4.

One may wonder if this large sc LRO of (3) Al 1nn environment could be an artifact of the particular values of interatomic interaction potentials. Therefore, simulations were performed with a range of ratios for 1nn and 2nn interatomic interactions that produce $D0_3$ chemical order (Table 6.7). Simulations using these potentials all provided large sc LRO parameters for the (3) Al 1nn environments, with an average of 0.94 for $\eta_{\mathrm{sc}}^{(3)}$. The alloys of Monte-Carlo simulations do show very strong sc LRO for Fe atoms with (3) Al 1nn. Curiously, this parameter is too strong, compared to experiment result of 0.59 ± 0.05.

6.5.2 Homogeneous Disorder

General consideration

It was mentioned in section 6.3.5 that we were surprised to find substantial sc order for Fe atoms with (3) Al 1nn environment. The Monte-Carlo simulation presented in the previous section support this experimental result. Here we investigate the structure responsible for this sc order. We seek a modification of the α and β sublattices of Fig. 1.1 to account for the (3) Al 1nn environment. The most efficient way to produce this (3) Al 1nn environment is to place antisite Fe atoms on the δ sublattice (Fig. 6.2). This produces eight (3) Al 1nn environments on the α and β sublattices, and no other types of Fe 1nn environments. The alternative possibility of multiple Al atoms on α and β sublattices is less likely, since many other types of Al 1nn environments would be created. Relatively few Fe atoms need to be placed on the δ sublattice to create (3) Al 1nn environments, so this way is favored.

To test our idea, a second type of computer simulation was performed to generate "homogeneous disorder". The simulation began with a structure having perfect $D0_3$ order. Random interchanges of Al atoms off the δ-sublattice were then performed until each Al atom was swapped for an Fe atom. Results are presented in Figs. 6.13 and 6.14 and discussed below.

Analytic Calculation of Sublattice Concentration for Homogeneous Disorder

Suppose x is the concentration of antisite defects in δ-site, it is easy to calculate the concentration of chemical environments on all 4 fcc sublattices. Table 6.8 presents the results for α and β sublattices. The concentrations on the γ and δ sublattices can be related to those of α and β sublattices by

$$\begin{aligned} c_\delta &= x c_\gamma \\ c_\alpha &= c_\beta \end{aligned}$$

Simulation Results for Defect Periodicities

The SRO and LRO parameters for different amounts of homogeneous disorder were obtained from simulations, and are presented in Figs. 6.13 and 6.14. Figure 6.13 shows that for the near-perfect $D0_3$ structure (near 0% antisite defects), the Fe atoms have primarily 0 and 4 Al atoms in their 1nn shells. The fractions of these environments decrease with increasing numbers of antisite defects.

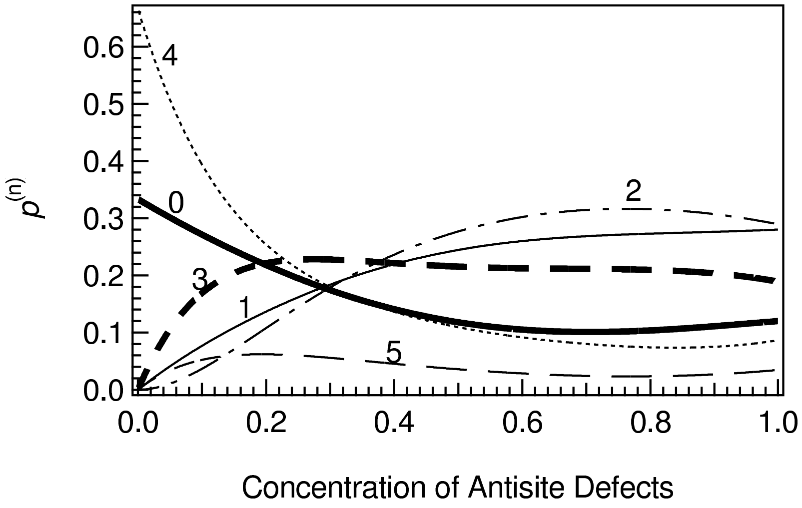

Figure 6.13: Short-range order with random antisite defects, obtained from simulations of homogeneous disorder. The axis $p(n)$ is the fraction of ^{57}Fe atoms having the number n Al atoms in their 1nn shell. Labels denote numbers, (n), of Al 1nn atoms about ^{57}Fe atoms.

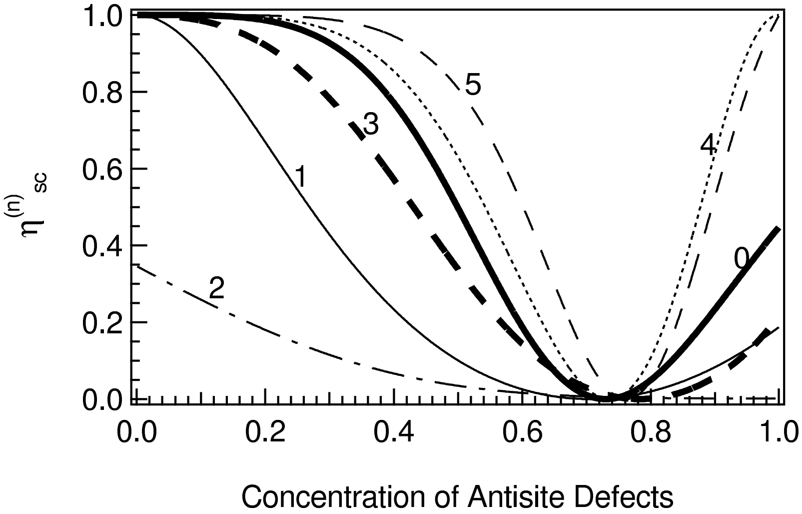

Figure 6.14: Long-range order with random antisite defects, obtained from simulations of homogeneous disorder. The LRO parameter, η_{sc}, was obtained from Eq. 6.9

Table 6.8: Concentration of chemical environments in α and β fcc sublattices in case of homogeneous antisite defect concentration x.

Chemical Environments	c_α	c_β
(0)	$x(1-\frac{x}{3})^8$	$x^4(1-\frac{x}{3})^4$
(1)	$\frac{8}{3}x(1-\frac{x}{3})^7$	$4x^3(1-x)(1-\frac{x}{3})^4+\frac{4}{3}x^5(1-\frac{x}{3})^3$
(2)	$\frac{28}{9}x^2(1-\frac{x}{3})^6$	$6x^2(1-x)^2(1-\frac{x}{3})^4+\frac{16}{3}x^4(1-x)(1-\frac{x}{3})^3+\frac{2}{3}x^6(1-\frac{x}{3})^2$
(3)	$\frac{56}{27}x^3(1-\frac{x}{3})^5$	$4x(1-x)^3(1-\frac{x}{3})^4+8x^3(1-x)^2(1-\frac{x}{3})^3+\frac{8}{3}x^5(1-x)(1-\frac{x}{3})^2+\frac{4}{27}x^7(1-\frac{x}{3})$
(4)	$\frac{70}{81}x^4(1-\frac{x}{3})^4$	$(1-x)^4(1-\frac{x}{3})^4+\frac{16}{3}x^2(1-x)^3(1-\frac{x}{3})^3+4x^4(1-x)^2(1-\frac{x}{3})^2$
(5)	$\frac{56}{243}x^5(1-\frac{x}{3})^3$	$\frac{4}{3}x(1-x)^4(1-\frac{x}{3})^3+\frac{8}{3}x^3(1-x)^3(1-\frac{x}{3})^2+\frac{8}{9}x^5(1-x)^2(1-\frac{x}{3})+\frac{4}{81}x^7(1-x)$

The state of full disorder, a random solid solution of Fe-25at.% Al, exists when the antisite defect concentration is 0.75 (beyond this there is some $D0_3$ order with Fe atoms on the Al sublattice). At the antisite defect concentration of 0.75, the probabilities for Fe atoms having n Al neighbors are equal to the binomial probability, $p(8,n,0.25) = \{8!\,[(8-n)!\,n!]^{-1}\}\ 0.25^n\,0.75^{(1-n)}$. At this antisite defect concentration of 0.75, all LRO parameters are zero.

Figure 6.14 shows that, at low antisite concentrations, Fe atoms with (3) Al 1nn have exactly the same LRO as Fe atoms with (4) Al 1nn. For a $D0_3$-ordered domain with few defect atoms, the B2 LRO parameter for Fe atoms with (3) Al 1nn is, therefore, $\eta_{\mathrm{sc}}^{(3)} \simeq 1$.

It is straightforward to test if the experimental measurements are consistent with the homogeneous disorder of Figs. 6.13 and 6.14. With an experimental SRO of approximately 0.13 for the (3) Al 1nn chemical environments, Fig. 6.13 shows that the concentration of antisite defects is approximately 0.07. Figure 6.14 shows that for an antisite defect of 0.07, the (3) Al 1nn chemical environments have a high B2 LRO parameter, nearly 1.0. Figures 6.13 and 6.14, based on a homogeneous random distribution of antisite atoms, predict that the B2 LRO of (3) Al 1nn chemical environments should be much higher than our experimental results. This result is consistent with results of Monte-Carlo simulation presented in section 6.5.1. However, the discrepancy between the near-perfect order of 1.0 and the experimental result of 0.59 ± 0.05 is still unresolved.

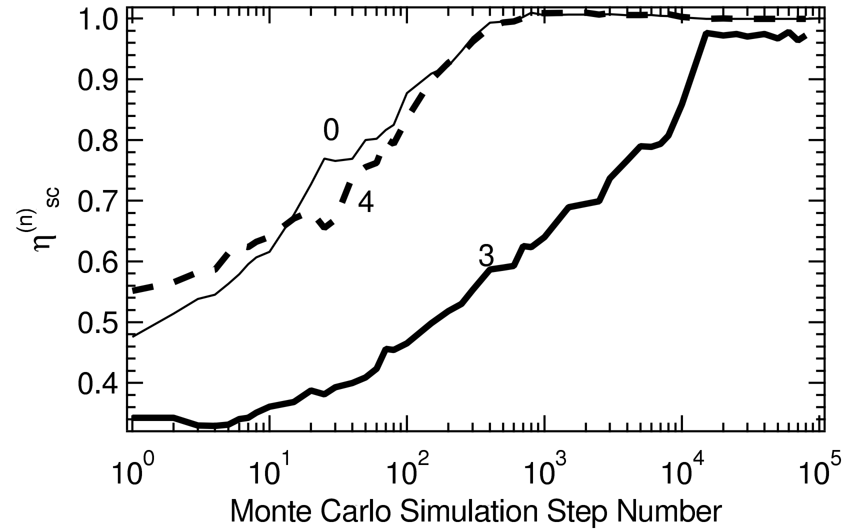

Figure 6.15: Development of B2 LRO of the different Al neighborhoods of ^{57}Fe, calculated by Monte–Carlo simulation. Labels denote numbers, (n), of Al 1nn atoms about ^{57}Fe atoms.

6.5.3 Effects of Antiphase Boundaries

We seek to understand why the LRO of (3) Al 1nn environments measured by Mössbauer diffractometry is 0.59, rather than nearly 1.0. One possibility is suggested by a Monte–Carlo simulation of ordering kinetics presented in Fig. 6.15. This figure shows that the LRO of (3) Al 1nn chemical environments undergoes a sharp increase at Monte–Carlo step number 10,000, well after the (0) and (4) Al 1nn environments have developed order. Graphical displays of the atom arrangements at this late stage of the simulation showed the disappearance of the antiphase boundaries. It therefore seems that the (3) Al 1nn chemical environments in the neighborhood of an antiphase boundary have smaller LRO than those in other regions.

Since the four variants of the D0_3 structure are determined by the position of the Al sublattice, an antiphase boundary (APB) can be characterized by the displacement of the Al sublattices across the APB. Antiphase boundaries are either B2-type, for which the displacement vector is $a_0\langle\frac{1}{2}\frac{1}{2}\frac{1}{2}\rangle$, or D$0_3$-type, for which it is $a_0\langle 100\rangle$ [41]. The plane of the APB is also specified, e.g., (hkl).

An APB alters chemical environments by shifting pairs of atoms across the boundary. Only atoms in pairs whose bonds are cut by the APB can have changes to their chemical environments. A D0_3-type APB changes only 2nn bonds [41]. Second neighbors cause only weak effects on the ^{57}Fe hyperfine magnetic field, so we can neglect D0_3-type APBs. We concern ourselves only with B2-type APBs, an example of which is presented in Fig. 6.16. The central Fe atom in Fig. 6.16a has

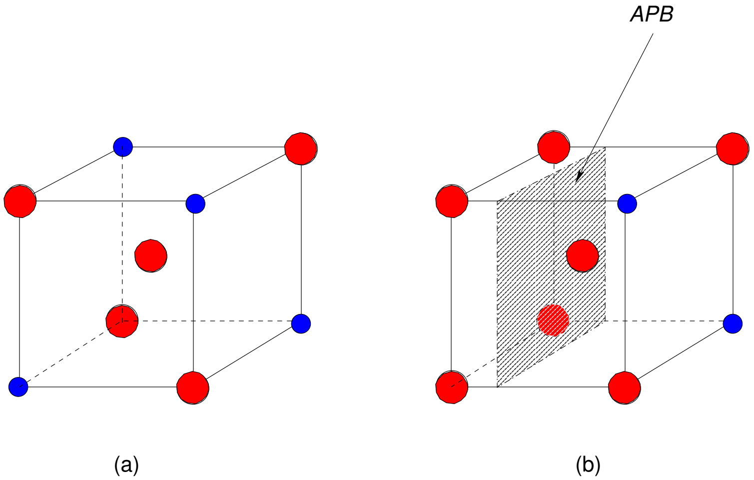

Figure 6.16: Geometry of a B2-type APB on a (100) plane. The Fe atoms are represented by bigger spheres and Al atoms are smaller. (**a**) A structure without APB. The Fe atom at the center has 4 Al and 4 Fe 1nns. (**b**) A B2-type APB is inserted between the central Fe atom and the 4 atoms on the left.

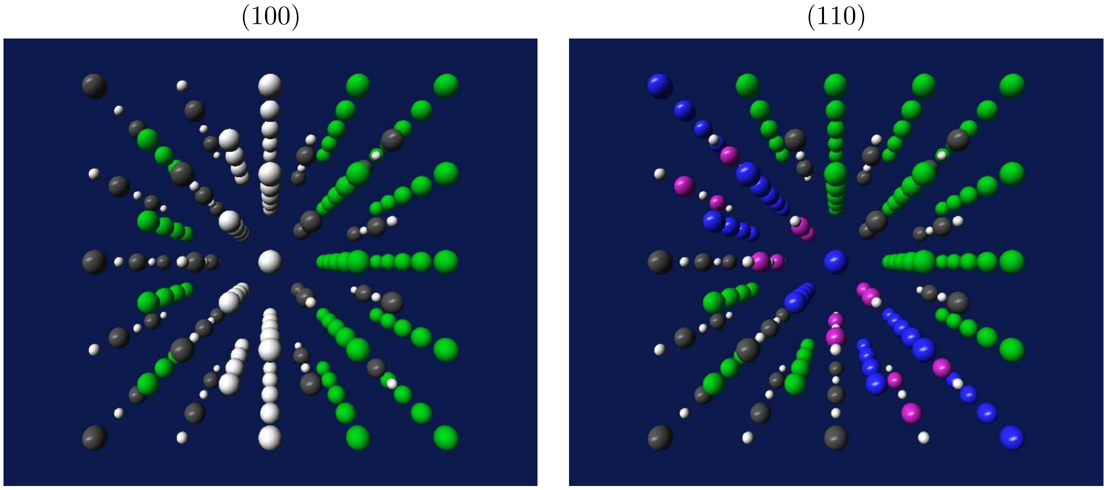

Figure 6.17: B2 type APBs on the (100) and (110) planes. Small, white balls are Al atoms. Big atoms are all Fe atoms, in which color indicates number of Al 1nn, black:0, green:4, white:2, blue:3, purple:1. It is clear that the B2-APB on the (100) plane consists of Fe atoms with (2) Al 1nn; the B2-APB on the (110) plane consists of Fe atoms with (3) and (1) Al 1nn.

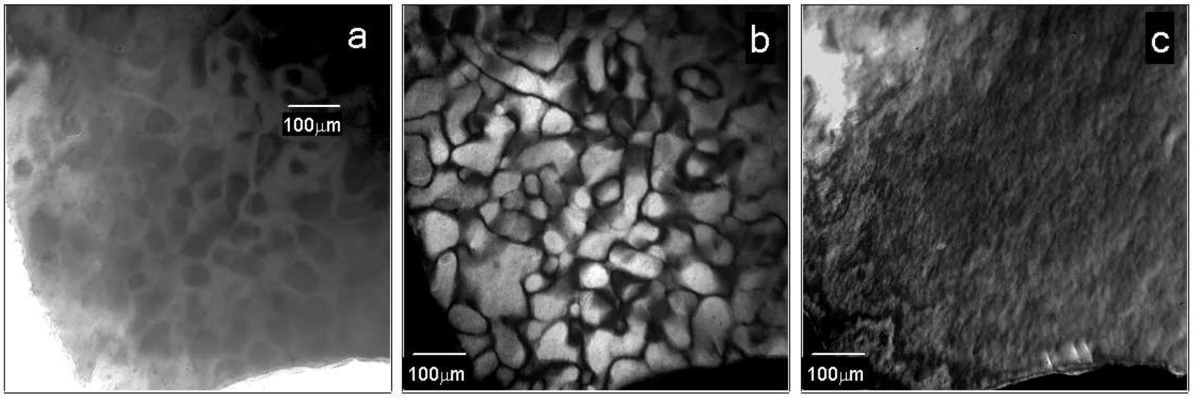

Figure 6.18: TEM images of B2-type APBs in ordered Fe_3Al: (a) bright-field image, (b) axial dark-field image using a (100) superlattice diffraction, (c) axial dark-field image using a (200) diffraction.

4 Al and 4 Fe atom neighbors. The B2-type APB on the (100) plane in Fig. 6.16b brings four Fe atoms to the left of the APB (these four Fe atoms were originally on the α and β sublattices). This particular APB transforms a (4) Al 1nn chemical environment to a (2) Al 1nn chemical environment. Similarly, an Fe atom having a (0) Al 1nn environment will also be transformed to a (2) Al 1nn environment. These facts were confirmed by computer constructions (Fig. 6.17) of several B2-type APBs. Similar analysis and computer constructions of B2-type APBs on (111) and (110) planes showed the formation of (1) and (3) Al 1nn chemical environments on the boundary. None of these Fe atoms had fcc or sc spatial periodicities. With further thought one concludes that B2-type APBs on planes other than (100), (110) and (111) will induce combinations of (1), (2) and (3) Al 1nn chemical environments.

In summary, B2-type APBs can produce Fe atoms with (1), (2) or (3) Al 1nn environments, depending on the orientation of the boundary. The Fe atoms whose bonds are modified by the APB could be on any sublattice except the Al sublattice. These defect environments are almost evenly distributed over all four fcc sublattices, and have neither fcc-type nor sc-type LRO.

We understand the LRO parameter $\eta_{\text{sc}}^{(3)} \simeq 0.6$ for (3) Al 1nn environments as follows. For homogeneous disorder of a few random antisite defects, the Fe atoms with (3) Al 1nn are highly ordered. On the other hand, an antiphase boundary produces (3) Al 1nn chemical environments on all sublattices. Together these two mechanisms can produce various states of LRO for (3) Al 1nn chemical environments, with order parameters $\eta_{\text{sc}}^{(3)}$ ranging from 0 to 1.

The APBs are responsible for a fraction of iron atoms having the (3) Al 1nn environment, f_3^{APB}:

$$f_3^{\mathrm{APB}} = \overline{\frac{6a_0}{0.75l}}\kappa = 8\kappa a_0 \overline{l^{-1}} \;, \tag{6.10}$$

where the factor of 6 is an approximation to scale the number of atom sites at the domain boundary to the number of sites in the domains (a cubical domain has 6 surfaces). The factor 0.75 is the fraction of all atoms that are Fe. The lattice constant is a_0, and is 0.289 nm. The domain size is l, and $\overline{l^{-1}}$ is the averaged inverse-domain-size. The fraction of (110) and (111)-direction APBs in all APBs is κ, which is expected to be on the order of 0.5,[5] because there is no preference in the directions of APBs [41].

From Table 6.2, the fraction of all Fe atoms having the (3) Al 1nn chemical environments is 0.14, so the homogeneous disorder is responsible for a fraction of iron atoms having the (3) Al 1nn environment equal to $f_3^{\mathrm{HD}} = 0.14 - f_3^{\mathrm{APB}}$. The total B2 LRO of 0.6 can be estimated as $0.6 = [(0.14 - f_3^{\mathrm{APB}}) \times 0.9 + f_3^{\mathrm{APB}} \times 0.0]/0.14$, which provides $f_3^{\mathrm{APB}} = 0.05$, and hence a fraction $f_3^{\mathrm{HD}} = 0.09$ from homogeneous disorder. Substituting this f_3^{APB} into Eq. 6.10 provides $\overline{l^{-1}} = [23\,\mathrm{nm}]^{-1}$. This is close to what we estimate from the broadenings of the superlattice x-ray diffractions, although these measurements are not so accurate for domains of this size.

Transmission Electron Microscopy Study of Antiphase Domain Boundaries

The dark-field imaging technique of transmission electron microscopy is especially well-suited for determining the sizes of domains in ordered alloys. The interest here is in identifying the sizes of B2-type domains, since these are capable of producing aperiodic defect environments for Fe atoms with (3) Al 1nn.

Figure 6.18 shows a bright-field image and two dark field images, taken with a superlattice (100) diffraction and a fundamental (200) diffraction. The diffraction conditions used for these images are shown in Fig. 6.19. It is significant that the rounded dark lines are visible for the (100) dark-field image, but not for the (200) dark-field image. This shows that the curved lines in Fig. 6.18b are from antiphase domain boundaries [41]. Some domain boundary contrast is expected in the bright field image, owing to the modest intensity of the (001) diffraction in Fig. 6.19b. The average size of the domains was determined by drawing lines at random through the image of Fig. 6.18b, and collecting a histogram of line segments between boundaries. Assuming the sample to be thin compared to the size of the domains, the average length of a line segment is properly volume-averaged for use as $\overline{l^{-1}}$

---

[5] This is a conservative estimate. Actually, there are 6 kinds of (100) planes, but 12 of (110) and 8 of (111). If these are the only planes, and exist with equal probabilities, then $\kappa = \frac{20}{26}$.

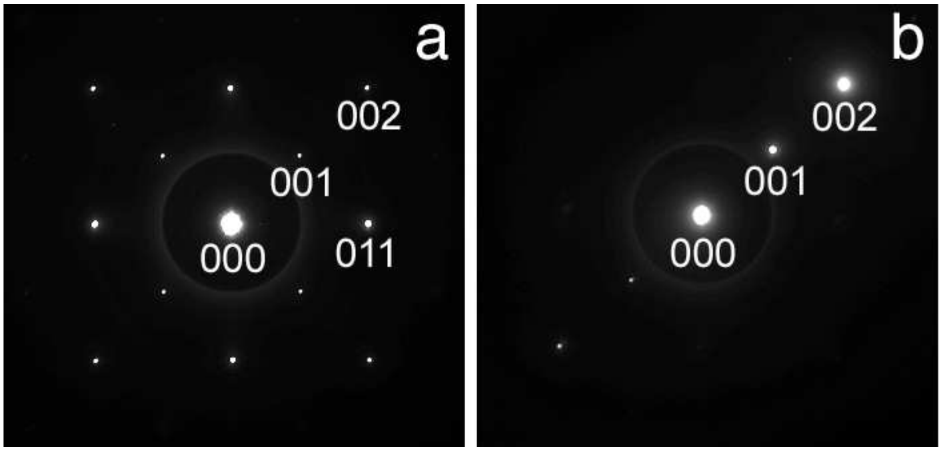

Figure 6.19: Diffraction patterns showing the conditions used for the bright-field and dark-field images of Fig. 6.18. (a) (100) zone axis used, (b) actual tilt used for imaging.

in Eq. 6.10}. From images such as Fig. 6.18b we obtained $\overline{l^{-1}} = [46\,\mathrm{nm}]^{-1}$. This is of the right order, but approximately half as large as needed to account for all aperiodic Fe atoms having the (3) Al 1nn environment. This suggests the presence of other sources of disordered Fe environments, but there are uncertainties from the approximations in our analysis, and perhaps differences in the samples.

6.6 Conclusions

A Mössbauer powder diffractometer was used to measure the energy spectra of the nuclear and electronic Bragg diffractions from a partially-ordered sample of ^{57}Fe$_3$Al. Effects of dynamical diffraction were calculated with a polycrystalline adaptation of the software package CONUSS, and it was found that the experimental diffraction data were in the kinematical limit. The energy spectra of the (300) and $(\frac{5}{2}\frac{3}{2}\frac{3}{2})$ superlattice diffractions showed that Fe atoms with (0) and (4) Al 1nn environments have the expected spatial LRO of the D0$_3$ structure. It was less obvious what, if any, spatial periodicity should be expected for other chemical environments of Fe atoms. By comparing the measured energy spectra of fundamental and superlattice diffractions with calculations for different arrangements of Fe atoms with various Al first nearest-neighbors, detailed information about the long-range order of these defect environments were measured for the first time. It was found that Fe atoms with the (3) Al 1nn environment have sc LRO parameters about 60% as large as that for Fe atoms with the (4) Al 1nn environment. This is lower than predicted for a geometrical structure generated by a

Monte-Carlo simulation that otherwise matches the SRO and LRO of the alloy. These Fe atoms in the (3) Al 1nn environment are probably neighbors of antisite Fe atoms on the δ sites of the D0_3 structure (the Al-rich sublattice is denoted δ). Sublattice occupancies of Fe atoms with (1) and (2) Al 1nn neighbors were similar to that of the Fe atoms with (0) Al 1nn neighbors, whereas the sublattice occupancies of Fe atoms with (3) and (5) Al 1nn neighbors were similar to that of the Fe atoms with (4) Al 1nn neighbors. No evidence was found for B32 LRO for any of the chemical environments.

Chapter 7

Ongoing and Future Work

7.1 CdTe Detector

In this thesis research we successfuly measured Mössbauer diffraction patterns, which, for the first time, provided data to determine unknown periodicities in a $^{57}Fe_3Al$ sample. The data collection time was long (several months), making this technique less applicable to many studies of materials. The low count rate and the high background noise in our experiment are two major reasons for long data-collection time. The low count rate is intrinsic to kinematical Mössbauer diffraction experiments using isotope source. The background noise in both the Inel detector used previously by Dr. Stephens and the Bruker detector used by Dr. Kriplani and us accounts for the majority of the detected counts. This is partly due to the fact that both these detectors are not very capable of descriminating against photons of undesired energy. The recent development of CdTe/CdZnTe X-ray detectors, which have very good energy resolution, provides a new possibility for improvement of instrumentaion for Mössbauer powder diffractometry. Table 7.1 presents some critical properties of Inel, Bruker and CdTe detectors. The CdTe detector has similar solid-angle coverage[1] and spatial resolution, and better efficiency, compared to other two detectors. Moreover, it has less ambient noise. The 8Hz noise figure includes events in all energy bins, while only events around 14.4keV are counted as Mössbauer diffraction intensity. Its excellent energy resolution should greatly reduce the background noise by perhaps one order of magnitude or more. In this chapter I describe our progress in building a new-generation detector that takes advantage of CdTe/CdZnTe detector technology.

---

[1] Due to the geometry of the source collimator, actually 2/3 of the solid-angle coverage of the Bruker detector contains unusable data.

Table 7.1: Comparison of detectors. The CdTe detector system is assumed to be composed of 8 detectors as described in Table 7.2. The distance between the sample and the Bruker detector is assumed to be 10 cm; for the CdTe detector it is assumed to be 12 cm. The gas inside the INEL detector is assumed to be 90% Ar and 10% Kr.

	Inel	Bruker	CdTe
Energy resolution	Nil	Nil	<1keV
Efficiency to 14.4keV photons	35%	80%-90%	>90%
Spatial resolution	0.06 deg	0.2 deg (0.4 mm)	0.2 deg (0.5mm)
Solid angle coverage	<0.12 sr	∼1 sr	∼0.1sr (12cm distance)
Ambient noise	3.5Hz	∼20Hz	8Hz

Table 7.2: Technical details about the CdTe detector

Geometry of one detector chip	1 mm×23.6 mm×12.9 mm
Pixel pattern	24×44
Pixel size	0.498 mm
Interconnection	Flip-chip bonding
Energy Resolution	<1 keV

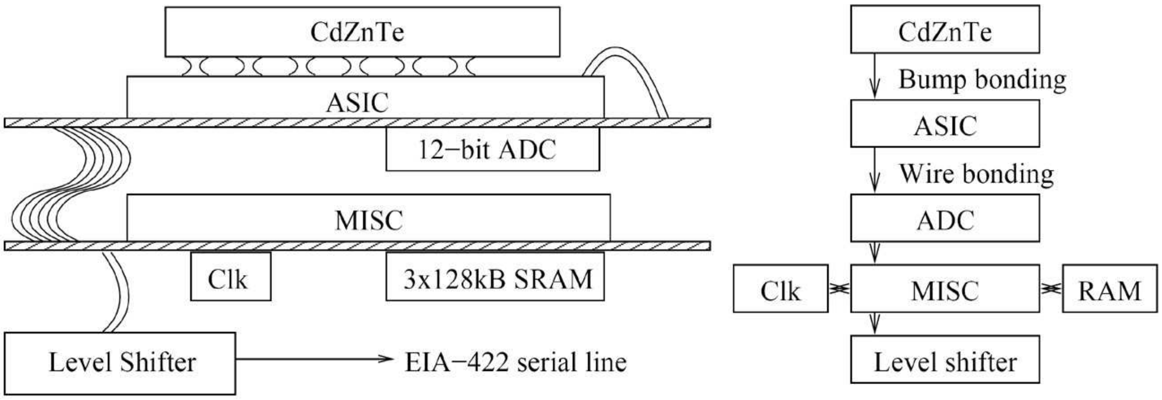

Figure 7.1: A schematic of a CdZnTe detector system.

7.1.1 CdTe/CdZnTe Detector

CdTe/CdZnTe (II/IV) detectors emerged in the 1970s. They are very attractive candidates as room-temperature X-ray and γ-ray detectors. After intensive developments in 1990s, they are now finding more and more applications.

The technical difficulties for the CdTe/CdZnTe detectors involve:

- material uniformity
- detector fabrication (metal contacts, chemical etching, surface passivation)
- interconnectivity (bump bonding)
- low-noise readout electronics (high energy resolution)
- high cost (\$18 per 1 mm^2)

The detector technology we are using is being developed by the Astrophysics group of Prof. Fiona Harrison in Caltech for the balloon-borne, high energy focusing telescope (HEFT) project[2]. Basic properties of a CdTe detector chip are presented in Table 7.2.

A schematic of a CdZnTe/CdTe detector is shown in Fig. 7.1. The CdTe detector chips were made and patterned by ACRORAD, Tokyo. Epoxy bumps are then put on the detector chips and, gold stud bumps are put on the ASIC[3] chips. The flip-chip bonding method is used to bond the

---

[2] We call this technology SRL-ASIC from now on.

[3] Application-Specific Integrated Circuit

CdTe and ASIC chips together to form a detector "hybrid". A detector hybrid is then glued onto a "motherboard". The connection between the ASIC chip and the motherboard which contains the analog-digital-converters (ADC), is done by wire bonding. The computer control of the motherboard is done through a 24-bit microprocessor (P24) running a Forth kernel, which is mounted on a "MISC board". Digital recording of each detector event is sent to a computer by a RS422 connection.

7.1.2 Construction of a CdTe Detector

The development of a CdZnTe/CdTe detector array has been a major engineering accomplishment of the Caltech HEFT group. For us the construction of a CdTe detector involves the following tasks [4]:

1. purchase the CdTe chips
2. upon receiving the detector, do optical examination of detector surface and then leakage current measurements
3. if the detector pass examination, put gold studs on the ASIC and put conductive epoxy on detector; do flip-chip bonding (bond the ASIC and the detector chip)
4. glue the hybrid to motherboard
5. do wire-bonding to connect wires from ASIC to the motherboard
6. connect the high-voltage wire to the top (cathode) of the detector chip
7. build level shifters that are used to talk to the MISC board. test it
8. connect the MISC board, motherboard and level shifters. this completes a detector system as shown in Fig. 7.2. test it

7.1.3 Low-Noise Electronics

In the SRL-ASIC, each pixel in a CdTe/CdZnTe detector has its own preamplifier, postamplifier, shaping amplifier, discriminator, and sampling and pulsing circuits. A serial readout line is shared by all pixels. The ASIC was designed for low noise and power (50 mW). For this purpose, a design (shown in Fig. 7.3) was developed that is different from the conventional amplifier chain for solid-state detectors. Conventional detector electronics use a shaping amplifier to transform a

---

[4] Tasks 3 and 5 need special apparatus and expertise, and are performed by specific companies.

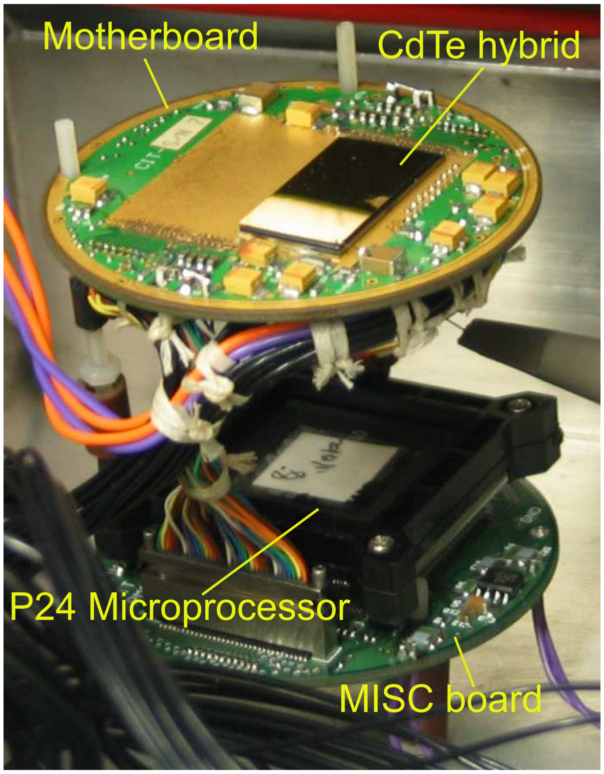

Figure 7.2: A MISC board and a motherboard with one CdTe detector.

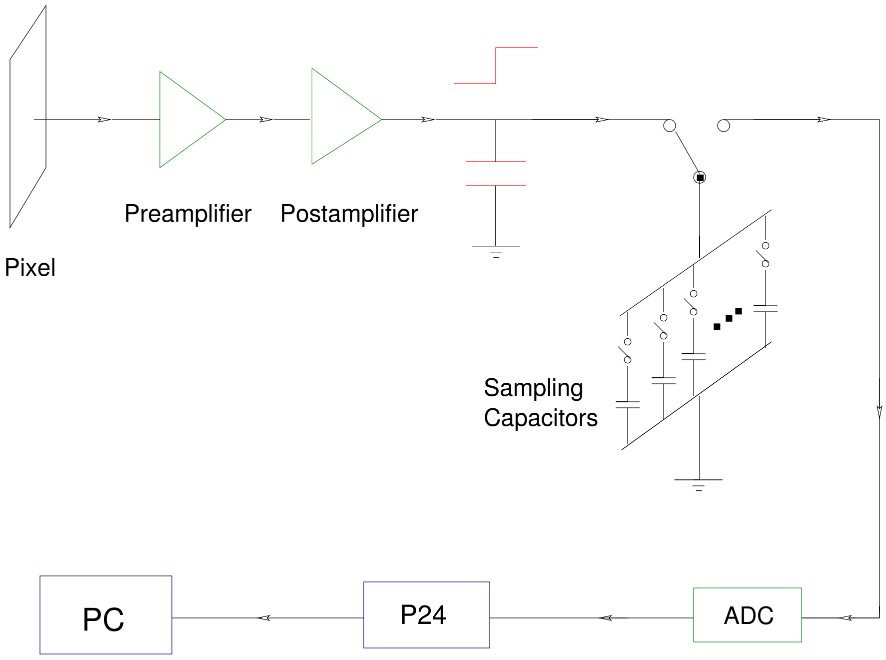

Figure 7.3: A schematic of the low-noise readout electronics for CdTe/CdZnTe detectors developed by Harrison's group.

step-function-like signal from the postamplifier to a pulse having a height proportional to the event energy. In the SRL-ASIC, this approach is replaced by feeding the step-function-like signal through an array of 16 sampling capacitors. The waveform of the signal from the postamplifier is recorded in the 16 sampling capacitors[5]. The signals in these capacitors are then fed to off-chip ADCs. This technique also ensures near optimal energy resolution.

7.1.4 Digital Signal Processing

The novel electronic design presented in the previous subsection requires extra digital signal processing using software. The quality of this software processing influences the quality of the energy spectra.

Pulse-height

The first step of the software is to recover the pulse height of an event from the event record. An event record contains the following information:

- time since last system reset[6], $t_{\rm slr}$
- number of pixels involved in the event, $n_{\rm inv}$. It includes both the triggered (hot) pixels and the neighboring pixels of the hot pixels.
- number of reference pixels[7], $n_{\rm ref}$
- for every pixel:
    - 16 sampling capacitor voltages
    - coordinates of the pixel
- capacitor sequence ID (please refer to footnote 5)

Each event record first goes through several validity-tests; currently the following tests are in effect

1. $t_{\rm slr}$ test. If it is too small, the electronics might not be able to stablize.

---

[5] The current at the postamplifier is fed into each of the 16 sampling capacitors for $0.5\,\mu$sec interval sequentially and cyclically. When an event is detected, the sampling process will continue for 8 more $0.5\,\mu$sec intervals, so that 8 pre-trigger and 8 post-trigger levels are stored in the capacitor array. Notice that the starting capacitor that records the first signal of the waveform of an event may be any one of the 16 capacitors.

[6] Since there is a dc current at the postamplifier output of $0.5\,\mu$A, the sampling capacitor array needs to be reset every 1 ms if there is no tigger.

[7] To reduce background electronic noise, signal levels of some reference pixels are recorded for every event.

2. n_{hot} test. The maximum number of hot pixels is 2. Charge sharing events of 3 or more pixels rarely happen, and it is hard to recover a pulse-height from those events.

If any of the tests failed, the event is discarded. For accepted events, several corrections can be done to achieve more accurate recovery of pulse-height, if requested:

1. subtract reference signals from hot pixels to reduce common-background noise
2. subtract the average signal of neighboring pixels from the hot pixels to reduce cross-talk noise
3. rise-time correction. The descrete sampling of a wave-form could induce systematic errors in pulse-height recovering if the wave-form is blindly passed to a digital filter. One of such errors comes from the fact that the rising edge of an event could be anywhere in between the moments when the 7th and the 9th capacitors are sampling. Blindly passing an event waveform to a filter actually gives rise to a correlation between the obtained pulse-height and the time of rising edge (rise-time). By assuming a linear correlation between the pulse-height and the rise-time, one can carry out rise-time correction, which was found to greatly improve the energy resolution.

After the corrections, the 16 sampling capacitor voltages are fed to a software filter to obtain the pulse-height of the event.

Energy Spectrum of a Pixel

In order to convert pulse-height to event energy, calibration experiments are required. The calibration data is obtained by feeding known electric potentials to the preamplifier of each pixel. The correlation between the pulse-height and the input signal level is then resolved and conversion constants are extracted. These constants are then used to rescale the pulse-heights to energies for real X-ray/γ-ray events.

An energy spectrum summed from all pixels of the first CdTe detector built for our Mössbauer diffractometer is shown in Fig. 7.4. For ^{57}Fe diffraction data, events of energy around 14.4 keV should be integrated for each individual pixel. A diffraction pattern could then be otained using the same algorithm presented in section 5.2.1.

7.2 Future Development and Research

The development of the CdTe detector is critical for future work. Issues need to be addressed in the course of building the CdTe detector system include

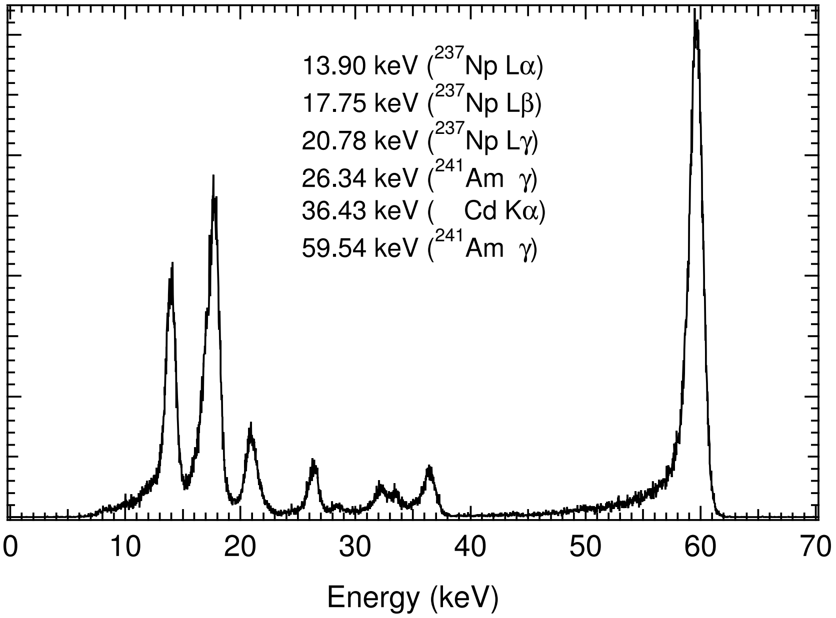

Figure 7.4: Energy spectrum of a ^{241}Am source measured by a CdTe detector with all pixels summed together. Only single-pixel events are included.

- Cooling. The CdTe detector works better at lower temperature. Thermoelectric coolers are required.
- Prevention of condensation caused by cooling.
- Mounting. To hold multiple CdTe detectors, a fixture needs to be designed with much care. For example, when selecting the distance between the detectors and the sample, we must compromise between better spatial resolution and larger solid-angle coverage.
- Data collection control/monitoring hardware and software. Time information should be recorded for each event so that the synchronous router can be discarded and the constant-acceleration mode of the Doppler drive can be used. The system must monitor and protect against faulty in temperature, moisture, voltages of detector cathodes, power to various chips, and Doppler velocity. A mechanism should be provided to automatically shutdown the system in case of emergencies.
- Data processing software capable of real-time processing and display of detector data and diffraction patterns needs development.

The new detector system could enable several new experiments. The evolution of transient B32 order in Fe_3Al is worthy of further investigations by Mössbauer diffraction. We could trace the ordering kinetics by measuring the evolution of the periodicities of the defect-related chemical environments.

The quasicrystal AlCuFe is a potential candidate for future research. The quasicrystal structure has been intensively studied for two decades, and many of its properties are well-known. However, the atomic decoration on the structure units in quasicrystal is still difficult to resolve. In AlCuFe quasicrystal, for example, the sites for Fe and Cu have proved hard to determine. Conventional Mössbauer spectrometry studies of AlCuFe quasicrystals showed a distribution of electric field gradients (EFG) corresponding to a variety of chemical environments for Fe atoms. A large EFG usually indicates a large asymmetry, structural or electronic, of the environment of the Fe atom. Therefore, it is expected that a Mössbauer diffraction study of AlCuFe quasicrystal can shed light on the long range order of those different chemical environments, and hence the atomic decoration for Fe and Cu atoms. This work might need theoretical development of the kinematical diffraction theory to include the quasicrystal case. The averaging of the polarization factors due to a random distribution of EFG main axes might need to be worked out. Perhaps the calculation of EFG, by electronic structure codes such as WIEN2k would also help support the structure determination effort.

As mentioned in section 4.2.3, a Mössbauer diffraction study of INVAR might resolve the controversy on its magnetic structure. This work needs the incorporation of a photon polarizer in the Mössbauer photon source, which could add difficulties, however.

Appendix A

Quantum Description of Recoilless Fraction

The Mössbauer effect is a scattering problem involving an incident photon, a nucleus, and the lattice vibrations, which can be described as a system of phonons. The transition matrix is

$$\left\langle f \middle| \hat{V} \middle| i \right\rangle \tag{A.1}$$

where

$\|i\rangle$	Initial State
$\|f\rangle$	Final State
$\hat{V}$	Interaction Potential

The interaction between a photon and a nucleus involves at least two subsystems, the internal degrees of freedom of the nucleus, and the motions of the nucleus. These two subsystems are not coupled so we can consider the two subsystems separately. The interaction potential is discussed in Chapter 3. Here we assume that it can be approximated as a δ-potential:

$$\hat{V}(\mathbf{x}, \mathbf{X}) \propto \delta(\mathbf{x} - \mathbf{X}) \tag{A.2}$$

The position vectors of the photon and the nucleus are $\mathbf{x}$ and $\mathbf{X}$, respectively.

In the initial state, there is an unexcited nucleus, a photon, and some phonons. In the final state, there is an excited nucleus, no photon, and some phonons. So, considering the independence of the two subsystems

$$|i\rangle = |1\rangle_\gamma |0\rangle_{\mathrm{N}} |\{n_s\}\rangle \tag{A.3}$$

$$|f\rangle = |0\rangle_\gamma |1\rangle_{\mathrm{N}} |\{n'_s\}\rangle \tag{A.4}$$

Here, $|\rangle_\gamma$ is a photon-state, $|\rangle_{\mathrm{N}}$ is a nuclear state, and

$$|\{n_s\}\rangle = \prod_s |n_s\rangle \tag{A.5}$$

is a state of phonons in the solid. Here n_s is the number of phonons in the mode denoted s.

Suppose the incident γ-ray is a plane-wave

$$|1\rangle_\gamma \propto \ exp(i\mathbf{k}\cdot\mathbf{x}) \tag{A.6}$$

then

$$_\gamma \left\langle 0 \left| \hat{V} \right| 1 \right\rangle_\gamma \propto \int d\mathbf{x} \ exp(i\mathbf{k}\cdot\mathbf{x})\delta(\mathbf{x}-\mathbf{X}) = exp(i\mathbf{k}\cdot\mathbf{X})$$

The total probability of all possible transitions is 1

$$\sum_f \left| \left\langle f \left| \hat{V} \right| i \right\rangle \right|^2 = 1 \tag{A.7}$$

So we have

$$\sum_{\{n'_s\}} \left| \langle \{n'_s\} \left| C \ exp(i\mathbf{k}\cdot\mathbf{X}) \right| \{n_s\} \rangle \right|^2 = 1 \tag{A.8}$$

Actually we are lucky; this equation is satisfied when the constant $C = 1$. Thus, the recoilless fraction is A.9

$$f_{\mathrm{ML}} = \left| \langle \{n_s\} \left| \ exp(i\mathbf{k}\cdot\mathbf{X}) \right| \{n_s\} \rangle \right|^2 \tag{A.9}$$

The position operator can be decomposed into the original position and a displacement

$$\mathbf{X} = \mathbf{X}_0 + \mathbf{u} \tag{A.10}$$

and the displacement can be expressed as a superposition of all phonon modes

$$\mathbf{u} = \sum_{s=1}^{3N} \sqrt{\frac{\hbar}{2M\omega_s N}} \mathbf{e}_s \left(a_s e^{i\mathbf{k}_s\cdot\mathbf{X}_0} + a_s^\dagger e^{-i\mathbf{k}_s\cdot\mathbf{X}_0} \right) \tag{A.11}$$

By substituting Eq. A.10 and A.11 into Eq. A.9, and after expanding $exp(i\mathbf{k}\cdot\mathbf{X})$ up to the second order, we find the first order term vanishes, and the second-order term gives N_s. The result is

$$f_{\mathrm{ML}} = exp\left[-\sum_{s=1}^{3N} \frac{(\mathbf{k}\cdot\mathbf{e}_s)^2}{M\hbar\omega_s N} \left(N_s + \frac{1}{2} \right) \right] \tag{A.12}$$

In equilibrium

$$N_s = \frac{1}{exp(\hbar\omega_s/k_B T) - 1}\,, \tag{A.13}$$

and for isotropic solid

$$\overline{(\mathbf{k}\cdot\mathbf{e}_s)^2} = k^2/3\,. \tag{A.14}$$

The Debye model gives the density of phonon states as

$$\rho(\omega)d\omega = 9N\omega^2 d\omega/\omega_{max}^3 \tag{A.15}$$

So Eq. A.12 can be evaulated by changing the sum to an integration as

$$f_{\mathrm{ML}} = exp\left[-\frac{3E_{\mathrm{R,free}}}{2k_B\theta_D}\left(1 + \frac{4T^2}{\theta_D^2}\int_0^{\theta_D/T}\frac{x}{e^x - 1}dx\right)\right] \tag{A.16}$$

Appendix B

Average Polarization Factors

We evaluate Eq. 4.20 here. First examine the case where function ρ is just a spherical harmonic function $Y_{lm}(\mathbf{u}_z)$. In this case we have

$$\begin{aligned} Y_{lm}(\mathbf{R}\mathbf{u}_z^0) &= \sum_{m'} Y_{lm'}(\mathbf{u}_z^0)\left[D^l_{m'm}(R^{-1})\right] \\ &= \sum_{m'} Y_{lm'}(\mathbf{u}_z^0)\left[D^l_{mm'}(R)\right]^* \end{aligned} \tag{B.1}$$

The rotation matrices $D^l_{m'm}(\mathbf{R})$ here are defined by Rose[46]. The cross section corresponding to this kind of "spherical-harmonic-like" distribution can be obtained with the help of Group Theory. It is natural to expand the distribution function by a series of spherical harmonics

$$\rho(\mathbf{u}_z) = \sum_{\lambda\mu} a^{\lambda\mu} Y_{\lambda\mu}(\mathbf{u}_z)\,. \tag{B.2}$$

So the averaged cross section is also written as an expansion

$$\begin{aligned} \overline{\left[\frac{d\sigma}{d\Omega}\right]} &= \int d\mathbf{R}\rho(\mathbf{R}\mathbf{u}_z^o)\mathbf{P}_R\left[\frac{d\sigma}{d\Omega}\right] \\ &= \int d\mathbf{R}\sum_{\lambda\mu} a^{\lambda\mu} Y_{\lambda\mu}(\mathbf{R}\mathbf{u}_z^o)\mathbf{P}_R\left[\frac{d\sigma}{d\Omega}\right] \\ &= \sum_{\lambda\mu} a^{\lambda\mu}\int d\mathbf{R}\sum_{\nu} Y_{\lambda\nu}(\mathbf{u}_z^o)\left[D^l_{\mu\nu}(\mathbf{R})\right]^*\mathbf{P}_R\left[\frac{d\sigma}{d\Omega}\right] \end{aligned} \tag{B.3}$$

We need to evaluate

$$\left[\frac{d\sigma}{d\Omega}\right]^{\lambda}_{\mu\nu} = \int d\mathbf{R}\left[D^{\lambda}_{\mu\nu}(\mathbf{R})\right]^*\mathbf{P}_R\left[\frac{d\sigma}{d\Omega}\right], \tag{B.4}$$

and it is the averaged cross section of a hypothetic HMF distribution in the form of a spherical harmonic. We then have the averaged cross section of HMF distribution $\rho(\mathbf{n})$

$$\overline{\left[\frac{d\sigma}{d\Omega}\right]} = \sum_{\lambda\mu\nu} a^{\lambda\mu} Y_{\lambda\nu}(\mathbf{u}_z^o) \left[\frac{d\sigma}{d\Omega}\right]^{\lambda}_{\mu\nu} \tag{B.5}$$

B.1 Contribution from Nuclear Resonant Scattering

With similar notations as the previous section, we investigate the "pure" contribution from the nuclear resonant scattering [1]

$$\begin{aligned} & \left[\frac{d\sigma}{d\Omega}\right]^{\lambda}_{\mu\nu;\mathrm{nuc}} && \text{(B.6)} \\ = & \int d\mathbf{R} \left[D^{\lambda}_{\mu\nu}(\mathbf{R})\right]^* \mathbf{P}_R \left\{ |f_{\mathrm{nuc}}|^2 \right\} \\ = & \int d\mathbf{R} \left[D^{\lambda}_{\mu\nu}(\mathbf{R})\right]^* \mathbf{P}_R \left\{ \left| \sum_{m,M} f^0_{\mathrm{nuc}} P_{\mathrm{nuc}} \right|^2 \right\} \\ = & \int d\mathbf{R} \left[D^{\lambda}_{\mu\nu}(\mathbf{R})\right]^* \\ & \times \mathbf{P}_R \left\{ \sum_{m,M,m',M'} f^0_{\mathrm{nuc}}(m,M) \left[f^0_{\mathrm{nuc}}(m',M')\right]^* P_{\mathrm{nuc}}(M) \left[P_{\mathrm{nuc}}(M')\right]^* \right\} && \text{(B.7)} \end{aligned}$$

It is convenient to first evaluate the average

$$\begin{aligned} & \left[\overline{P^2}\right]^{\lambda}_{\mu\nu;\mathrm{nuc}} \\ = & \int d\mathbf{R} \left[D^{\lambda}_{\mu\nu}(\mathbf{R})\right]^* \mathbf{P}_R \left\{ P_{\mathrm{nuc}}(M) \left[P_{\mathrm{nuc}}(M')\right]^* \right\} \\ = & \int d\mathbf{R} \left[D^{\lambda}_{\mu\nu}(\mathbf{R})\right]^* \mathbf{P}_R \left\{ \begin{array}{l} \sqrt{\frac{8\pi}{3}} \left[\mathbf{e}_i \cdot \mathbf{Y}^{(\mathrm{m})}_{1M}(\mathbf{n}_i)\right] \sqrt{\frac{8\pi}{3}} \left[\mathbf{e}_f \cdot \mathbf{Y}^{(\mathrm{m})}_{1M}(\mathbf{n}_f)\right]^* \\ \times \sqrt{\frac{8\pi}{3}} \left[\mathbf{e}_i \cdot \mathbf{Y}^{(\mathrm{m})}_{1M'}(\mathbf{n}_i)\right] \sqrt{\frac{8\pi}{3}} \left[\mathbf{e}_f \cdot \mathbf{Y}^{(\mathrm{m})}_{1M'}(\mathbf{n}_f)\right]^* \end{array} \right\} \\ = & \int d\mathbf{R} \left[D^{\lambda}_{\mu\nu}(\mathbf{R})\right]^* \mathbf{P}_R \left\{ \begin{array}{l} \sqrt{\frac{1}{2}} \left[D^1_{1M}(\mathbf{R}_i) + D^1_{-1,M}(\mathbf{R}_i)\right] \sqrt{\frac{1}{2}} \left[D^1_{1M}(\mathbf{R}_f) + D^1_{-1,M}(\mathbf{R}_f)\right]^* \\ \times \sqrt{\frac{1}{2}} \left[D^1_{1M'}(\mathbf{R}_i) + D^1_{-1,M'}(\mathbf{R}_i)\right] \sqrt{\frac{1}{2}} \left[D^1_{1M'}(\mathbf{R}_f) + D^1_{-1,M'}(\mathbf{R}_f)\right]^* \end{array} \right\} \\ = & \frac{1}{4} \int d\mathbf{R} \left[D^{\lambda}_{\mu\nu}(\mathbf{R})\right]^* \left[D^1_{1M}(\mathbf{R}_i\mathbf{R}) + D^1_{-1,M}(\mathbf{R}_i\mathbf{R})\right] \left[D^1_{1M}(\mathbf{R}_f\mathbf{R}) + D^1_{-1,M}(\mathbf{R}_f\mathbf{R})\right]^* \\ & \times \left[D^1_{1M'}(\mathbf{R}_i\mathbf{R}) + D^1_{-1,M'}(\mathbf{R}_i\mathbf{R})\right]^* \left[D^1_{1M'}(\mathbf{R}_f\mathbf{R}) + D^1_{-1,M'}(\mathbf{R}_f\mathbf{R})\right] \end{aligned}$$

---

[1] The symbols used here are a little different from those used in Chapter 3, 4. m is the z-component angular momentum of nuclear ground state (M_0 in Chapters 3,4), and M is the z-component photon angular momentum (m in Chapters 3, 4).

$$\begin{aligned}
= \ & \frac{1}{4}\sum_{m_i,m_i',} \left[D^1_{1m_i}(\mathbf{R}_i)+D^1_{-1,m_i}(\mathbf{R}_i)\right]\left[D^1_{1m_i'}(\mathbf{R}_i)+D^1_{-1,m_i'}(\mathbf{R}_i)\right]^* \\
& \times \left[D^1_{1m_f}(\mathbf{R}_f)+D^1_{-1,m_f}(\mathbf{R}_f)\right]\left[D^1_{1m_f'}(\mathbf{R}_f)+D^1_{-1,m_f'}(\mathbf{R}_f)\right]^* \\
& \times \int d\mathbf{R}\left[D^\lambda_{\mu\nu}(\mathbf{R})\right]^* D^1_{m_i,M}(\mathbf{R})\left[D^1_{m_i',M'}(\mathbf{R})\right]^* D^1_{m_f,M'}(\mathbf{R})\left[D^1_{m_f',M}(\mathbf{R})\right]^*
\end{aligned} \tag{B.8}$$

We separate the last integral and investigate its properties,

$$\begin{aligned}
& J^\lambda_{\mu\nu} \\
= \ & \int d\mathbf{R}\left[D^\lambda_{\mu\nu}(\mathbf{R})\right]^*\left\{D^1_{m_i,M}(\mathbf{R})\left[D^1_{m_i',M'}(\mathbf{R})\right]^* D^1_{m_f,M'}(\mathbf{R})\left[D^1_{m_f',M}(\mathbf{R})\right]^*\right\} \\
= \ & \int d\mathbf{R}\left[D^\lambda_{\mu\nu}(\mathbf{R})\right]^* \sum_{j=0,1,2}\langle 1m_i1m_f|11;j,m_i+m_f\rangle\, D^j_{m_i+m_f,M+M'}(\mathbf{R})\,\langle 11;j,M+M'|1M1M'\rangle \\
& \times\left[\sum_{j'=0,1,2}\left\langle 1m_i'1m_f'|11;j',m_i'+m_f'\right\rangle D^{j'}_{m_i'+m_f',M+M'}(\mathbf{R})\,\langle 11;j',M+M'|1M'1M\rangle\right]^* \\
= \ & \sum_{j=0,1,2}\sum_{j'=0,1,2}\frac{1}{2j+1}C^{1,1,j}_{m_i,m_f,m_i+m_f}C^{1,1,j'}_{m_i',m_f',m_i'+m_f'}C^{1,1,j}_{M,M',M+M'}C^{1,1,j'}_{M',M,M+M'} \\
& \quad \times C^{j',\lambda,j}_{m_i'+m_f',\mu,m_i+m_f}C^{j',\lambda,j}_{M+M',\nu,M+M'}
\end{aligned} \tag{B.9}$$

In the last step, the formula for the integral over three rotation matrices was used.

Obviously

$$J^\lambda_{\mu\nu} = 0 \text{ if } \nu \neq 0$$

so only the $J^\lambda_{\mu 0}$ are non-trivial. We drop ν, and define

$$\begin{aligned}
J^\lambda_\mu(m_i,m_f,m_i',m_f',M,M') \ = \ & \sum_{j=0,1,2}\sum_{j'=0,1,2}\frac{1}{2j+1}C^{1,1,j}_{m_i,m_f,m_i+m_f}C^{1,1,j'}_{m_i',m_f',m_i'+m_f'} \\
& \times C^{1,1,j}_{M,M',M+M'}C^{1,1,j'}_{M',M,M+M'} \\
& \times C^{j',\lambda,j}_{m_i'+m_f',\mu,m_i+m_f}C^{j',\lambda,j}_{M+M',0,M+M'}
\end{aligned} \tag{B.10}$$

Then

$$\begin{aligned}
\left[\overline{P^2}\right]^\lambda_{\mu;\mathrm{nuc}} \ = \ & \frac{1}{4}\sum_{m_i,m_i',m_f,m_f'} J^\lambda_\mu(m_i,m_f,m_i',m_f',M,M') \\
& \times\left[D^1_{1m_i}(\mathbf{R}_i)+D^1_{-1,m_i}(\mathbf{R}_i)\right]\left[D^1_{1m_i'}(\mathbf{R}_i)+D^1_{-1,m_i'}(\mathbf{R}_i)\right] \\
& \times\left[D^1_{1m_f}(\mathbf{R}_f)+D^1_{-1,m_f}(\mathbf{R}_f)\right]\left[D^1_{1m_f'}(\mathbf{R}_f)+D^1_{-1,m_f'}(\mathbf{R}_f)\right]^*
\end{aligned}$$

Select the coordinate system for the incident photon as the initial quantization system, so

$$
\begin{aligned}
D^1_{mM}(\mathbf{R}_i) &= \delta_{mM} && \text{(B.11)}\\
D^1_{mM}(\mathbf{R}_f) &= D^1_{mM}(\frac{\pi}{2}, 2\theta, -\frac{\pi}{2}) && \text{(B.12)}
\end{aligned}
$$

We obtain

$$
\begin{aligned}
\left[\overline{P^2}\right]^{\lambda}_{\mu;\mathrm{nuc}} &= \frac{1}{4} \sum_{m_i, m_i', m_f, m_f'} J^{\lambda}_{\mu}(m_i, m_f, m_i', m_f', M, M')\\
&\quad \times \left[\delta_{1m_i} + (-1)^{n_i-1}\delta_{-1,m_i}\right]\left[\delta_{1m_i'} + (-1)^{n_i-1}\delta_{-1,m_i'}\right]\\
&\quad \times \left[D^1_{1m_f}(\frac{\pi}{2}, 2\theta, -\frac{\pi}{2}) + (-1)^{n_f-1}D^1_{-1,m_f}(\frac{\pi}{2}, 2\theta, -\frac{\pi}{2})\right]\\
&\quad \times \left[D^1_{1m_f'}(\frac{\pi}{2}, 2\theta, -\frac{\pi}{2}) + (-1)^{n_f-1}D^1_{-1,m_f'}(\frac{\pi}{2}, 2\theta, -\frac{\pi}{2})\right]^* && \text{(B.13)}
\end{aligned}
$$

n_i, n_f are the indexes of the polarization of incident and outgoing photons. The geometry is defined in Fig. 4.1.

We have

$$
\left[\frac{d\sigma}{d\Omega}\right]_{\mathrm{nuc}} = \sum_{\lambda\mu} a^{\lambda\mu} Y_{\lambda 0}(\mathbf{u}_z^o) \sum_{m,M,m',M'} f^0_{\mathrm{nuc}}(m, M)\left[f^0_{\mathrm{nuc}}(m', M')\right]^* \left[\bar{P}^2\right]^{\lambda}_{\mu;\mathrm{nuc}}(MM') \tag{B.14}
$$

Choose the original direction of the hyperfine magnetic field to be the z direction of the incident photon coordinate system,

$$
\mathbf{u}_z^o = \hat{z} \tag{B.15}
$$

Recall

$$
Y_{\lambda 0}(\hat{z}) = \sqrt{\frac{2\lambda + 1}{4\pi}} \tag{B.16}
$$

we obtain

$$
\begin{aligned}
\left[\frac{d\sigma}{d\Omega}\right]_{\mathrm{nuc}} &= \sum_{\lambda\mu} \sqrt{\frac{2\lambda + 1}{4\pi}} a^{\lambda\mu}\\
&\quad \times \sum_{m,M,m',M'} F^0_{\mathrm{nuc}}(m, M)\left[F^0_{\mathrm{nuc}}(m', M')\right]^* \left[\overline{P^2}\right]^{\lambda}_{\mu;\mathrm{nuc}}(MM') && \text{(B.17)}
\end{aligned}
$$

Table B.1: $\overline{P^2}$ Matrix

$n_i\backslash n_f$	1				2			
	$M\backslash M'$	-1	0	1	$M\backslash M'$	-1	0	1
1	-1	A_{11}	B_{11}	C_{11}	-1	A_{12}	B_{12}	C_{12}
	0	B_{11}	D_{11}	B_{11}	0	B_{12}	D_{12}	B_{12}
	1	C_{11}	B_{11}	A_{11}	1	C_{12}	B_{12}	A_{12}
	$M\backslash M'$	-1	0	1	$M\backslash M'$	-1	0	1
2	-1	A_{21}	B_{21}	C_{21}	-1	A_{22}	B_{22}	C_{22}
	0	B_{21}	D_{21}	B_{21}	0	B_{22}	D_{22}	B_{22}
	1	C_{21}	B_{21}	A_{21}	1	C_{22}	B_{22}	A_{22}

We can insert the number $\sqrt{\frac{2\lambda+1}{4\pi}}$ into $\left[\overline{P^2}\right]^{\lambda}_{\mu;\mathrm{nuc}}(MM')$, and define

$$\overline{P^2}^{n_i n_f MM'}_{\lambda\mu;\mathrm{nuc}} = \sqrt{\frac{2\lambda+1}{4\pi}}\left[\overline{P^2}\right]^{\lambda}_{\mu;\mathrm{nuc}}(MM') \tag{B.18}$$

Then we have

$$\left[\frac{d\sigma}{d\Omega}\right]_{\mathrm{nuc}} = \sum_{m,M,m',M'} f^0_{\mathrm{nuc}}(m,M)\left[f^0_{ncu}(m',M')\right]^* \overline{P^2}^{n_i n_f MM'}_{\mathrm{nuc}} \tag{B.19}$$

where

$$\overline{P^2}^{n_i n_f MM'}_{\mathrm{nuc}} = \sum_{\lambda\mu} a^{\lambda\mu}\overline{P^2}^{n_i n_f MM'}_{\lambda\mu;\mathrm{nuc}} \tag{B.20}$$

A $\overline{P^2}$ matrix depends on four variables n_i, n_f, M and M'. It could be tabulated as in Table B.1. The matrices A, B, C, and D need to be evaluated for different orientational distributions of the HMF, $\rho(\mathbf{n})$.

B.1.1 Spherical distribution of HMF

Obviously,$\lambda = 0$ for an isotropic distribution as in Fig. B.1. We have

$$\begin{aligned} A_{11} &= \frac{1}{60}(7+\cos[2(2\theta)]), \\ B_{11} &= \frac{1}{60}(1+3\cos[2(2\theta)]), \\ C_{11} &= 2B_{11} \end{aligned}$$

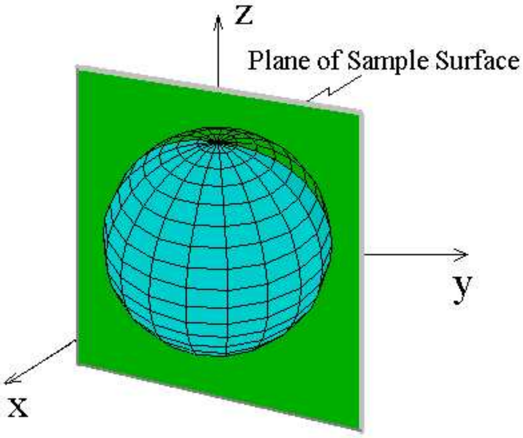

Figure B.1: Spherical distibution of HMF

$$D_{11} = \frac{1}{15}(2+\cos[2(2\theta)])$$

$$\begin{aligned} A_{12} &= A_{21} = \frac{1}{10} \\ B_{12} &= B_{21} = -\frac{1}{30} \\ C_{12} &= C_{21} = -\frac{1}{15} \\ D_{12} &= D_{21} = \frac{1}{15} \end{aligned}$$

$$\begin{aligned} A_{22} &= \frac{2}{15} \\ B_{22} &= \frac{1}{15} \\ C_{22} &= \frac{2}{15} \\ D_{22} &= \frac{1}{5} \end{aligned}$$

B.1.2 The Case of Nearly Planar Distribution of HMFs

Suppose the HMF distribution tends to lie in a plane mostly in a plane as shown in Fig. B.2. This model is more realistic for thin ferromagnetic iron han the previous isotropic one.

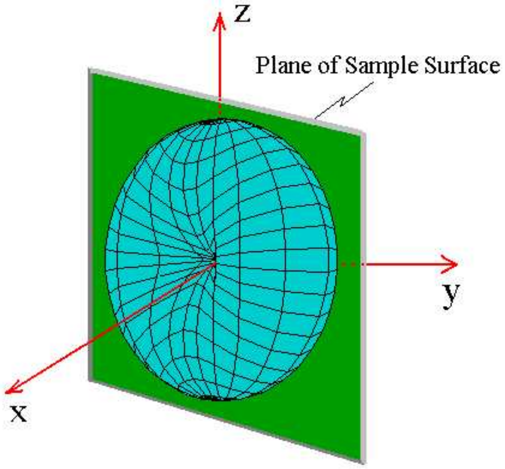

Figure B.2: Nearly planar distribution of HMF

If the normal of the plane is $\hat{n}_S$, let us define

$$\rho(\mathbf{u}_z) = \frac{3}{2}\left(1 - (\mathbf{u}_z \cdot \hat{n}_S)^2\right) \tag{B.21}$$

The factor $\frac{3}{2}$ is a normalization factor. It is easy to obtain that $\hat{n}_S = (\cos\beta_i, -\sin\beta_i, 0)$, where β_i is defined in Fig. 4.2.

After the evaluation of eq B.20 , we obtain the parameters of Table B.1

$$\begin{aligned}
A_{11} &= \frac{1}{70}(9 + \cos[2\beta_i] + \cos[2(2\theta)] + \cos[2(\beta_i - 2\theta)]), \\
B_{11} &= \frac{1}{280}(5 - \cos[2\beta_i] + 13\cos[2(2\theta)] - \cos[2(\beta_i - 2\theta)]), \\
C_{11} &= \frac{1}{70}(2 + \cos[2\beta_i] + 8\cos[2(2\theta)] + \cos[2(\beta_i - 2\theta)]), \\
D_{11} &= \frac{1}{70}(8 - 3\cos[2\beta_i] + 4\cos[2(2\theta)] - 3\cos[2(\beta_i - 2\theta)]),
\end{aligned}$$

$$\begin{aligned}
A_{12} &= \frac{1}{140}(13 + 3\cos[2\beta_i]), \\
B_{12} &= \frac{1}{140}(-5 + \cos[2\beta_i]), \\
C_{12} &= \frac{1}{35}(-2 - \cos[2\beta_i]),
\end{aligned}$$

$$D_{12} = \frac{1}{70}(5 - \cos[2\beta_i]),$$

$$\begin{aligned}
A_{21} &= \frac{1}{140}(13 + 3\cos[2\beta_i]), \\
B_{21} &= \frac{1}{140}(-5 + \cos[2\beta_i]), \\
C_{21} &= \frac{1}{35}(-2 - \cos[2(\beta_i - 2\theta)]), \\
D_{21} &= \frac{1}{70}(5 - \cos[2(\beta_i - 2\theta)]))
\end{aligned}$$

$$\begin{aligned}
A_{22} &= \frac{4}{35} \\
B_{22} &= \frac{1}{14} \\
C_{22} &= \frac{4}{35} \\
D_{22} &= \frac{1}{70}
\end{aligned}$$

B.2 Contribution from Rayleigh Scattering

This scattering mechanism is not related to the direction of the HMF, so we always have

$$\left[\frac{d\sigma}{d\Omega}\right]_{\text{ele}} = \int d\mathbf{R}\mathbf{P}_R \left\{|f_{\text{ele}}|^2\right\} = \left|f^0_{\text{ele}} P_{\text{ele}}\right|^2 \tag{B.22}$$

where

$$\begin{aligned}
P_{\text{ele}} &= -[\mathbf{e}_i.\mathbf{e}_j] \\
&= -\delta_{n_i,n_f}(\delta_{n_i,1} + \delta_{n_i,2}\cos(2\theta))
\end{aligned} \tag{B.23}$$

B.3 Contribution from Interference

This part is not trivial, and gives rich information in Mössbauer diffraction spectra. Noting

$$\left[\frac{d\sigma}{d\Omega}\right]^{\lambda}_{\mu\nu;\text{int}} = \int d\mathbf{R}\left[D^{\lambda}_{\mu\nu}(\mathbf{R})\right]^* \mathbf{P}_R\left\{f^*_{\text{nuc}} f_{\text{ele}} + f_{\text{nuc}} f^*_{\text{ele}}\right\}$$

$$
\begin{aligned}
= \; & f^*_{\mathrm{ele}} \sum_{m,M} f^0_{\mathrm{nuc}} \int d\mathbf{R} \left[D^\lambda_{\mu\nu}(\mathbf{R})\right]^* \mathbf{P}_R \left\{P_{\mathrm{nuc}}\right\} \\
& + f_{\mathrm{ele}} \sum_{m,M} \left(f^0_{\mathrm{nuc}}\right)^* \int d\mathbf{R} \left[D^\lambda_{\mu\nu}(\mathbf{R})\right]^* \mathbf{P}_R \left\{P^*_{\mathrm{nuc}}\right\} \qquad \text{(B.24)}
\end{aligned}
$$

we need to evaluate the integral

$$
\begin{aligned}
\bar{P}^\lambda_{\mu\nu;\mathrm{nuc}}(M) &= \int d\mathbf{R} \left[D^\lambda_{\mu\nu}(\mathbf{R})\right]^* \mathbf{P}_R \left\{P_{\mathrm{nuc}}\right\} \\
&= \int d\mathbf{R} \left[D^\lambda_{\mu\nu}(\mathbf{R})\right]^* \mathbf{P}_R \{ \sqrt{\frac{8\pi}{3}} \left[\mathbf{e}_i \cdot \mathbf{Y}^{(m)}_{1M}(\mathbf{n}_i)\right] \sqrt{\frac{8\pi}{3}} \left[\mathbf{e}_f \cdot \mathbf{Y}^{(m)}_{1M}(\mathbf{n}_f)\right]^* \} \\
&= \frac{1}{2} \int d\mathbf{R} \left\{ \begin{array}{c} \left[D^\lambda_{\mu\nu}(\mathbf{R})\right]^* \left[D^1_{1M}(\mathbf{R}_i\mathbf{R}) + D^1_{-1,M}(\mathbf{R}_i\mathbf{R})\right] \\ \times \left[D^1_{1M}(\mathbf{R}_f\mathbf{R}) + D^1_{-1,M}(\mathbf{R}_f\mathbf{R})\right]^* \end{array} \right\} \\
&= \frac{1}{2} \sum_{m_i,m_f} \left[D^1_{1,m_i}(\mathbf{R}_i) + D^1_{-1,m_i}(\mathbf{R}_i)\right] \left[D^1_{1,m_f}(\mathbf{R}_f) + D^1_{-1,m_f}(\mathbf{R}_f)\right]^* \\
& \quad \times \int d\mathbf{R} \left[D^\lambda_{\mu\nu}(\mathbf{R})\right]^* D^1_{m_i,M}(\mathbf{R}) \left[D^1_{m_f,M}(\mathbf{R})\right]^* \\
&= \frac{1}{6} \sum_{m_i,m_f} \left[D^1_{1,m_i}(\mathbf{R}_i) + D^1_{-1,m_i}(\mathbf{R}_i)\right] \left[D^1_{1,m_f}(\mathbf{R}_f) + D^1_{-1,m_f}(\mathbf{R}_f)\right]^* \\
& \quad \times C^{1,\lambda,1}_{m_f,\mu,m_i} C^{1,\lambda,1}_{M,\nu,M} \qquad \text{(B.25)}
\end{aligned}
$$

In the last step, the formula for the integral over three rotation matrices was used again.

If we apply the formula B.11, then we get

$$
\begin{aligned}
\bar{P}^\lambda_{\mu\nu;\mathrm{nuc}}(M) &= \frac{1}{6} \sum_{m_i,m_f} C^{1,\lambda,1}_{m_f,\mu,m_i} C^{1,\lambda,1}_{M,\nu,M} [\delta_{1m_i} + (-1)^{n_i-1}\delta_{-1,m_i}] \\
& \times \left[D^1_{1m_f}(\frac{\pi}{2}, 2\theta, -\frac{\pi}{2}) + (-1)^{n_f-1} D^1_{-1m_f}(\frac{\pi}{2}, 2\theta, -\frac{\pi}{2})\right]^* \qquad \text{(B.26)}
\end{aligned}
$$

Follow the same way we deal with $\left[\bar{P}^2\right]^\lambda_{\mu;\mathrm{nuc}}(MM')$, we drop ν

$$
\begin{aligned}
\bar{P}^\lambda_{\mu;\mathrm{nuc}}(M) &= \frac{1}{6} \sum_{m_i,m_f} C^{1,\lambda,1}_{m_f,\mu,m_i} C^{1,\lambda,1}_{M,0,M} [\delta_{1m_i} + (-1)^{n_i-1}\delta_{-1,m_i}] \\
& \times \left[D^1_{1m_f}(\frac{\pi}{2}, 2\theta, -\frac{\pi}{2}) + (-1)^{n_f-1} D^1_{-1m_f}(\frac{\pi}{2}, 2\theta, -\frac{\pi}{2})\right]^* \qquad \text{(B.27)}
\end{aligned}
$$

and define

$$
\overline{P}^{n_i n_f M}_{\lambda\mu;\mathrm{nuc}} = \sqrt{\frac{2\lambda+1}{4\pi}} \bar{P}^\lambda_{\mu;\mathrm{nuc}}(M) \qquad \text{(B.28)}
$$

Then for the interference part of scattering cross section, we have

$$\left[\frac{d\sigma}{d\Omega}\right]_{\text{int}}^{n_i n_f} = 2\text{Re}\left[\sum_{m,M}\left(f_{\text{ele}}^{0}\right)^{*} P_{\text{ele}}^{*} f_{\text{nuc}}^{0} \overline{P}_{\text{nuc}}^{n_i n_f M}\right] \tag{B.29}$$

where

$$\overline{P}_{\text{nuc}}^{n_i n_f M} = \sum_{\lambda\mu} a^{\lambda\mu} \overline{P}_{\lambda\mu;\text{nuc}}^{n_i n_f M} \tag{B.30}$$

B.3.1 Spherical Distribution of HMF

Obviously, $\lambda = 0$ for this isotropic case. So we have

$$\begin{aligned}
\overline{P}_{00;\text{nuc}}^{n_i n_f M} &= \frac{1}{6}\{D_{1,1}^{1}(\mathbf{R}_f)^{*} + D_{-1,1}^{1}(\mathbf{R}_f)^{*} + D_{1,-1}^{1}(\mathbf{R}_f)^{*} + D_{-1,-1}^{1}(\mathbf{R}_f)^{*}\} \\
&= \frac{1}{3}\delta_{n_i,n_f}(\delta_{n_i,1}\cos(2\theta) + \delta_{n_i,2})
\end{aligned} \tag{B.31}$$

It is independent of M. We can make it a matrix

$$\overline{P}_{00;\text{nuc}}^{n_i n_f M} = \begin{pmatrix} \frac{\cos(2\theta)}{3} & 0 \\ 0 & \frac{1}{3} \end{pmatrix} \tag{B.32}$$

B.3.2 Nearly Planar Distribution of HMF

For this case as shown in Fig. B.2:

$$\begin{aligned}
\overline{P}_{\text{nuc}}^{n_i n_f M} &= \begin{pmatrix} \frac{1}{20}(7\cos(2\theta) + \cos(2\beta_i - 2\theta)) & 0 \\ 0 & \frac{3}{10} \end{pmatrix}, \text{ if } M = \pm 1 \\
&= \begin{pmatrix} \frac{1}{10}(3\cos(2\theta) - \cos(2\beta_i - 2\theta)) & 0 \\ 0 & \frac{2}{5} \end{pmatrix}, \text{ if } M = 0
\end{aligned} \tag{B.33}$$

B.4 Basic Formulas for the Representations of Rotation Group

$$D_{m_1',m_1}^{j_i}(\mathbf{R}) D_{m_2',m_2}^{j_2}(\mathbf{R}) = \sum_{j}\left[\begin{array}{c} \langle j_1 m_1' j_2 m_2' | j_1 j_2; j, m_1' + m_2'\rangle\, D_{m_1'+m_2',m_1+m_2}^{j}(\mathbf{R}) \\ \times \langle j_1 j_2; j, m_1 + m_2 | j_1 m_1 j_2 m_2\rangle \end{array}\right] \tag{B.34}$$

Orthogonality:

$$\int \left[D_{m_1',m_1}^{j_i}(\mathbf{R})\right]^{*} D_{m_2',m_2}^{j_2}(\mathbf{R})\, d\mathbf{R} = \frac{1}{2j_1+1}\delta_{j_1,j_2}\delta_{m_1,m_2}\delta_{m_1',m_2'} \tag{B.35}$$

Integral of three rotation matrices

$$\int \left[D^{j}_{m,M}(\mathbf{R})\right]^{*} D^{j_1}_{m_1,M_1}(\mathbf{R}) D^{j_2}_{m_2,M_2}(\mathbf{R}) d\mathbf{R} = \frac{1}{2j+1} C^{j_1,j_2,j}_{m_1,m_2,m} C^{j_1,j_2,j}_{M_1,M_2,M} \tag{B.36}$$

B.5 Mathematica Code to Calculate Averaged Polarization Factors

Clebsch-Gordan Coefficients

```
ExtendedClebschGordan[ {j1_, m1_}, {j2_, m2_}, {j_, m_}] := If[ m1 + m2 ?
m || j1 + j2 < j || j1 - j2 > j || j2 - j1 > j || j < Abs[m] || j1 < Abs[m1]
|| j2 < Abs[m2], 0, ClebschGordan[ {j1, m1}, {j2, m2}, {j, m}]];
```

$J^{\lambda}_{\mu}(m_i, m_f, m'_i, m'_f, M, M')$

```
J[ lumda_, mu_, mi_, mf_, mip_, mfp_, M_, M1_] := Sum[ 1/(2j + 1)
ExtendedClebschGordan[ {1, mi}, {1, mf}, {j, mi + mf} ]
ExtendedClebschGordan[ {1, mip}, {1, mfp}, {jp, mip + mfp} ]
ExtendedClebschGordan[ {1, M}, {1, M1}, {j, M + M1} ]
ExtendedClebschGordan[ {1, M1}, {1, M}, {jp, M + M1} ]
ExtendedClebschGordan[ {jp, mip + mfp}, {lumda, mu}, {j, mi + mf} ]
ExtendedClebschGordan[ {jp,M + M1}, {lumda, 0}, {j, M + M1} ], {j, 0, 2}, {jp, 0, 2}];
```

Rotation Matrices

```
d1[ i_, j_, beta_] := Which[ Abs[i] > 1 || Abs[j] > 1, 0, i*j == 1,
( 1 + Cos[beta])/2, i*j == -1, ( 1 - Cos[beta])/2,( i == 0 && j == 1)
|| ( i == -1 && j == 0), -Sin[ beta]/Sqrt[2],( i == 1 && j == 0) ||
( i == 0 && j == -1), Sin[beta]/Sqrt[2],i == 0 && j == 0, Cos[beta]];

D1[ i_, j_, alpha_, beta_, gamma_] := Exp[ I j alpha] Exp[ I i gamma]
d1[ i,j, beta];
```

$\overline{P^2}$

```
AveragedPNuclearSquare[ lumda_, mu_, M_, M1_, ni_, nf_, twotheta_] :=
1/4Sum[ J[ lumda, mu, mi, mf, mip, mfp, M, M1] (KroneckerDelta[ 1, mi]
+ (-1)^(ni - 1) KroneckerDelta[ -1, mi]) (KroneckerDelta[ 1, mip]
+ (-1)^(ni - 1) KroneckerDelta[ -1, mip]) (D1[ 1, mf, Pi/2, twotheta,
-Pi/2] + (-1)^(nf - 1)D1[ -1, mf, Pi/2, twotheta, -Pi/2])
Conjugate[ ( D1[ 1, mfp, Pi/2, twotheta, -Pi/2] + (-1)^(nf - 1)
D1[ -1, mfp, Pi/2, twotheta, -Pi/2])], {mi, -1, 1}, {mf, -1, 1},
{mip, -1, 1}, {mfp, -1, 1}];
```

$\overline{P}$

```
AveragedPNuclear[ lumda_, mu_, M_, ni_, nf_, twotheta_] := 1/6
Sum[ ExtendedClebschGordan[ {1, mf}, {lumda, mu}, {1, mi}]
ExtendedClebschGordan[ {1, M}, {lumda, 0}, {1, M}]
( KroneckerDelta[ 1, mi] + (-1)^(ni - 1)
KroneckerDelta[ -1, mi]) Conjugate[ ( D1[ 1, mf, Pi/2, twotheta, -Pi/2 ]
+ (-1)^( nf - 1) D1[ -1, mf, Pi/2, twotheta, -Pi/2])], { mi, -1, 1},
{ mf, -1, 1}];
```

An example:

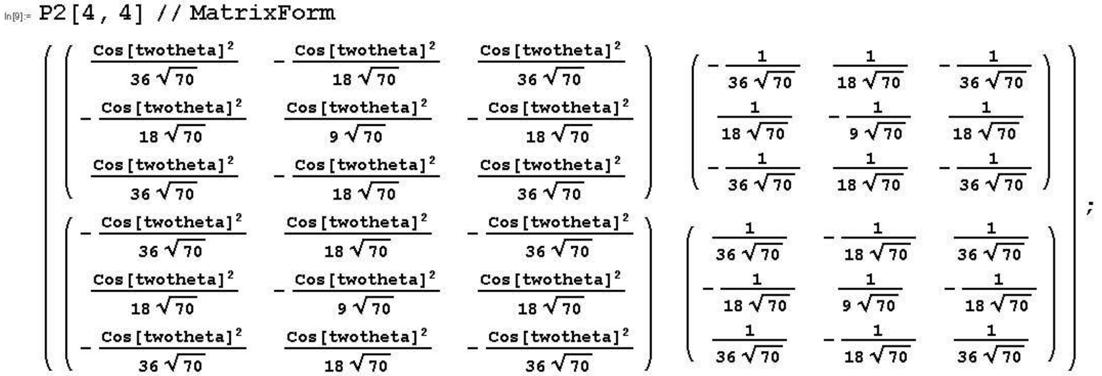

```
In[9]:= P2[4, 4] // MatrixForm
```

$$\begin{pmatrix} \begin{pmatrix} \frac{\mathrm{Cos[twotheta]}^2}{36\sqrt{70}} & -\frac{\mathrm{Cos[twotheta]}^2}{18\sqrt{70}} & \frac{\mathrm{Cos[twotheta]}^2}{36\sqrt{70}} \\ -\frac{\mathrm{Cos[twotheta]}^2}{18\sqrt{70}} & \frac{\mathrm{Cos[twotheta]}^2}{9\sqrt{70}} & -\frac{\mathrm{Cos[twotheta]}^2}{18\sqrt{70}} \\ \frac{\mathrm{Cos[twotheta]}^2}{36\sqrt{70}} & -\frac{\mathrm{Cos[twotheta]}^2}{18\sqrt{70}} & \frac{\mathrm{Cos[twotheta]}^2}{36\sqrt{70}} \end{pmatrix} & \begin{pmatrix} -\frac{1}{36\sqrt{70}} & \frac{1}{18\sqrt{70}} & -\frac{1}{36\sqrt{70}} \\ \frac{1}{18\sqrt{70}} & -\frac{1}{9\sqrt{70}} & \frac{1}{18\sqrt{70}} \\ -\frac{1}{36\sqrt{70}} & \frac{1}{18\sqrt{70}} & -\frac{1}{36\sqrt{70}} \end{pmatrix} \\ \begin{pmatrix} -\frac{\mathrm{Cos[twotheta]}^2}{36\sqrt{70}} & \frac{\mathrm{Cos[twotheta]}^2}{18\sqrt{70}} & -\frac{\mathrm{Cos[twotheta]}^2}{36\sqrt{70}} \\ \frac{\mathrm{Cos[twotheta]}^2}{18\sqrt{70}} & -\frac{\mathrm{Cos[twotheta]}^2}{9\sqrt{70}} & \frac{\mathrm{Cos[twotheta]}^2}{18\sqrt{70}} \\ -\frac{\mathrm{Cos[twotheta]}^2}{36\sqrt{70}} & \frac{\mathrm{Cos[twotheta]}^2}{18\sqrt{70}} & -\frac{\mathrm{Cos[twotheta]}^2}{36\sqrt{70}} \end{pmatrix} & \begin{pmatrix} \frac{1}{36\sqrt{70}} & -\frac{1}{18\sqrt{70}} & \frac{1}{36\sqrt{70}} \\ -\frac{1}{18\sqrt{70}} & \frac{1}{9\sqrt{70}} & -\frac{1}{18\sqrt{70}} \\ \frac{1}{36\sqrt{70}} & -\frac{1}{18\sqrt{70}} & \frac{1}{36\sqrt{70}} \end{pmatrix} \end{pmatrix};$$

Appendix C

Details about Data Reduction

C.1 Format of a “mds.in” File

Here is an example:

```
# input parameters for program mds
#
# lines started with # are comments
# words after // are also comments
#--------------------------------------------------------------------------
# experimental conditions
0.33 // magnitude of ext.  H field, Telsla
(0,1,0) // direction of the ext.  H field
(0.,0.,1.)  // reference vector
#
#material:  Fe3Al
#--------------------------------------------------------------------------
# a = 5.78A
# density = (1/5.78e-10)^3
0.0517e29 // density (# of unit cells in 1m^3)
7e-6 // thickness (unit:  m)
#--------------------------------------------------------------------------
# enrichment of 57Fe
0.90
#--------------------------------------------------------------------------
# the unit cell
24 // # of atoms in a unit cell.
#--------------------------------------------------------------------------
#*******************************************************************
# atom #0 -- Fe with 0Al 1nn
Fe // name
(0,0,0) // position
0.00195344 // weight
# HMF distribution height * exp( -(HMF -center)^2/width^2)
301.3 // center (unit:  kG)
-1.  // height ( -1 -- automatically calcualted to make sure the area of the gaussian distribution
= 1.
12.85 // width (unit:  kG)
0.06 // Isomer shift (unit:  mm/s)
-1 // dependency ( default -1)
```

```
   # atom #0 - done
   #********************************************************************
   # atom #1 -- Fe with 0Al 1nn
   Fe // name
   (0.5,0.5,1.5) // position
   0.234413 // weight
   # HMF distribution height * exp( -(HMF -center)^2/width^2)
   301.3 // center (unit:  kG)
   -1.  // height ( -1 -- automatically calcualted to make sure the area of the gaussian distribution
= 1.
   12.85 // width (unit:  kG)
   0.06 // Isomer shift (unit:  mm/s)
   0 // dependency ( default -1)
   # atom #1 - done
   #********************************************************************
   # atom #2 -- Fe with 0Al 1nn
   Fe // name
   (0.5,0.5,0.5) // position
   3.07277 // weight
   # HMF distribution height * exp( -(HMF -center)^2/width^2)
   301.3 // center (unit:  kG)
   -1.  // height ( -1 -- automatically calcualted to make sure the area of the gaussian distribution
= 1.
   12.85 // width (unit:  kG)
   0.06 // Isomer shift (unit:  mm/s)
   0 // dependency ( default -1)
   # atom #2 - done
   #********************************************************************
   ...
   ...
   #********************************************************************
   # atom #19 -- Fe with 5Al 1nn
   Fe // name
   (0,0,1) // position
   0.517662 // weight
   # HMF distribution height * exp( -(HMF -center)^2/width^2)
   167 // center (unit:  kG)
   -1.  // height ( -1 -- automatically calcualted to make sure the area of the gaussian distribution
= 1.
   13.9 // width (unit:  kG)
   0.23 // Isomer shift (unit:  mm/s)
   0 // dependency ( default -1)
   # atom #19 - done
   #********************************************************************
   # atom #20 -- Al
   Al // name
   (0,0,0) // position
   0.0859375 // weight
   -1 // dependency ( default -1)
   # atom #20 - done
   #********************************************************************
   ...
   ...
   #********************************************************************
   # atom #23 -- Al
   Al // name
   (0.5,0.5,0.5) // position
   0.320312 // weight
   -1 // dependency ( default -1)
   # atom #23 - done
```

```
   #******************************************************************#
   #
   #--------------------------------------------------------------------------
   # misc.  information
   #--------------------------------------------------------------------------
   # IS = a * HMF +b
   -0.002 // a (999 - this parameter will not be used.  instead, the IS in the input of each
atom will be used)
   0.66 // b (999 - this parameter will not be used.  instead, the IS in the input of each atom
will be used)
   #--------------------------------------------------------------------------
   # photons and geometries
   0.15 // line width of the source
   (1.,0.,0.)  // k vector of incident photon
   # 2theta = 42.70
   (0.7349,0.,0.6782) // k vector of outgoing photon
   21.  // the angle between k_i and the sample surface
   21.7 // the angle between k_o and the sample surface
   #--------------------------------------------------------------------------
   (2,1,1) // h k l
   #--------------------------------------------------------------------------
   # job type
   # 0 - diffracted intensity
   # 1 - absorption spectrum
   # 2 - hmf distribution function
   0 // job type
   #--------------------------------------------------------------------------
   #velocity bins
   -9.0 // vmin
   9.0 // vmax
   0.02 // vstep
```

C.2 Format of a Template "mds.in" File

To achieve high flexibility, the input files of MEF are in the form of one or more template "mds.in" file(s). Each template file corresponds to one diffraction order. A template "mds.in" file is just like a normal "mds.in" file, except that in a "mds.in" file all parameters are constants, whereas in a template "mds.in" file some parameters are variables for fitting. In a template "mds.in", one can define a set of variables, each of which has an initial value, a maximum and a minimum value.

For example, if the ^{57}Fe hyperfine magnetic field distribution of an iron atom were adjustable, we would define a variable $hmf0$ as follows:

```
!hmf0
~294
<304
>290
```

where `!`, `~`, `<`, and `>` indicate definition, approximate value, maximum value and minimum value, of the variable, respectively. Now we can use this variable to express the HMF parameter of the Fe atoms with (0) Al 1nn, for example,

```
   # atom #0 -- Fe with 0Al 1nn
   Fe .................species
   (0,0,0) ............position
   2.83 ...............weight
   1.000 ..............long range order
   =hmf0 ..............center of HMF distribution
   -1.  ...............height of HMF distribution.  -1 means automatically determined
by weight and width
   12.850 .............width of HMF distribution
```

The good thing about defining variables is that you can use an expression in the "= *something*" field for a parameter. For example, the normalization condition in our simulation of Fe_3Al required the weights of all atoms in a unit cell be

$$\sum_{i=1}^{7} c_i = 16$$

If $\{c_i\}$ are fitting parameters, one of them must be determined using the normalization condition. Therefore, for example, the weight of atom 7 in the template "mds.in" file could be:

```
=16.-c1-c2-c3-c4-c5-c6
```

Bibliography

[1] A. M. Afanas'ev and Y. Kagan. *Zh. Eksp. Teor. Fiz.*, 45:1660, 1963.

[2] G. A. P. Alcazar and E. Galvao Da Silva. *J. Phys. F: Met. Phys*, 17:2323, 1987.

[3] L. Anthony and B. Fultz. *J. Mater. Res.*, 4:1132, 1989.

[4] L. Anthony and B. Fultz. *J. Mater. Res.*, 9:348, 1994.

[5] J. J. Bara. *Phys. Stat. Solidi A*, 58:349, 1980.

[6] M. Becker and W. Schweika. *Scripta Materialia*, 35:1259, 1996.

[7] V. A. Belyakov. *Usp. Fiz. Nauk*, 115:553, English translation: Sov. Phys. Usp. 18 (1975) 267, 1975.

[8] V. A. Belyakov and R. Ch. Bokun. *Acta Cryst.*, A31:737, 1975.

[9] P. J. Black and I. P. Duerdoth. *Proc. Phys. Soc.*, 84:169, 1964.

[10] P. J. Black and P. B. Moon. *Nature*, 188:481, 1960.

[11] J. M. Blatt and V. F. Weisskopf. *Theoretical Nuclear Physics.* Dover Publications, New York, 1979.

[12] H. Chacham, E. Galvao Da Silva, D. Guenzburger, and D. E. Ellis. *Phys. Rev. B*, 35:1602, 1987.

[13] F. J. Dyson. *Phys. Rev.*, 75:486, 1949.

[14] F. J. Dyson. *Phys. Rev.*, 75:1736, 1949.

[15] R. P. Feynman. *Phys. Rev.*, 76:749, 1949.

[16] R. P. Feynman. *Phys. Rev.*, 76:769, 1949.

[17] R. P. Feynman. *Phys. Rev.*, 80:440, 1950.

[18] J. E. Frackowiak. *Phys. Stat. Sol.*, 87:109, 1985.

[19] B. Fultz and Z. Q. Gao. *Nucl. Instr. Meth. in Phys. Res. B*, 76:115, 1993.

[20] B. Fultz and J. M. Howe. *Transmission Electron Microscopy and Diffractometry of Materials*. Springer–Verlag, Heidelberg, 2000.

[21] B. Fultz and T. A. Stephens. *Hyperfine Interact.*, 113:199, 1998.

[22] Brent Fultz. *J. Chem. Phys.*, 87:1604, 1987.

[23] Brent Fultz. Chemical systematics of iron-57 hyperfine magnetic field distributions in iron alloys. In G. J. Long and Fernande Grandjean, editors, *Mössbauer Spectroscopy Applied to Magnetism and Materials Science*, volume 1, chapter 1, pages 1–31. Plenum Press, New York, 1993.

[24] Z. Q. Gao and B. Fultz. *Philos. Mag. B*, 67:787, 1993.

[25] Zheng-Qiang Gao. Ph.D. thesis, California Institute of Technology, 1994.

[26] E. Gerdau, R. Rüffer, H. Winkler, W. Tolksdorf, C. P. Klages, and J. P. Hannon. *Phys. Rev. Lett.*, 54:835, 1985.

[27] C. E. Guillaume. Recherches sur les aciers au nickel. dilations aux temperatures elevees; resistance electrique. *CR Acad. Sci.*, 125:235, 1897.

[28] J. P. Hannon and G. T. Trammel. *Phys. Rev.*, 169:315, 1968.

[29] J. P. Hannon and G. T. Trammel. *Phys. Rev.*, 186:306, 1969.

[30] J. P. Hannon and G. T. Trammel. *Hyperfine Interact.*, 123/124:127, 1999.

[31] Y. Kagan and A.M. Afanas'ev. *Zh. Eksp. Teor. Fiz.*, 47:1108, 1964.

[32] Yu. Kagan. *Hyperfine Interact.*, 123/124:83, 1999.

[33] Yu. Kagan, A. M. Afanas'ev, and I. P. Perstnev. *Ah. Eksp. Teor. Fiz*, 54:1530, 1968.

[34] U. Kriplani. Ph.D. thesis, California Institute of Technology, 2000.

[35] U. Kriplani, J. Y. Y. Lin, M. W. Regehr, and B. Fultz. *Phys. Rev. B*, 65:024405, 2002.

[36] G. Le Caër and J. M. Dubois. *J. Phys. E*, 12:1083, 1979.

[37] J. Y. Y. Lin and B. Fultz. *Phil. Mag.*, 83:2621, 2003.

[38] J. Y. Y. Lin, B. Fultz, and U. Kriplani. *Hyperfine Interact.*, 141:145, 2002.

[39] J. Y. Y. Lin, U. Kriplani, M. W. Regehr, and B. Fultz. *Hyperfine Interact.*, 136:663, 2001.

[40] Stephen W. Lovesey. *Theory of neutron scattering from condensed matter*, volume 1. Clarendon Press, 1984.

[41] M. J. Marcinkowski and N. Brown. *J. Appl. Phys.*, 33:537.

[42] Y. Nakai, Y. Ooi, and K. Kunitomi. *J. Phys. Soc. Jpn.*, 57:3172, 1988.

[43] D. A. O'Conner and P. J. Black. *Proc. Phys. Soc.*, 83:941, 1964.

[44] Hao Ouyang and Brent Fultz. *J. Appl. Phys.*, 66:4752, 1989.

[45] R. Rohlsberger. *Habilitationsshrift: Nuclear Condensed Matter Physics Using Synchrotron Radiation*. Universität Rostock, FRG, 2002.

[46] M. E. Rose. *Elementary Theory of Angular Momentum*. Dover, New York, 1995.

[47] S. L. Ruby. *J. Phys. (Paris)*, 35:C6–209, 1974.

[48] Hideo Saito, editor. *Physics and Applications of Invar Alloys*. Honda Memorial Series on Materials Science. Maruzen, Tokyo, 1978.

[49] Julian Schwinger. *Phys. Rev.*, 74:1439, 1948.

[50] Julian Schwinger. *Phys. Rev.*, 75:651, 1949.

[51] Julian Schwinger. *Phys. Rev.*, 76:790, 1949.

[52] Yu. V. Shvyd'ko and G. V. Smirnov. *J. Phys.: Condens. Matter*, 1:10563, 1989.

[53] G. V. Smirnov, V. V. Sklyareviskii, A. N. Artem'ev, and R. A. Voscanyan. *Phys. Lett.*, 32A:532, 1970.

[54] M. B. Stearns. *Phys. Rev.*, 147:439, 1966.

[55] M. B. Stearns. *Phys. Rev. B*, 6:3326, 1972.

[56] T. A. Stephens. Ph.D. thesis, California Institute of Technology, 1996.

[57] T. A. Stephens and B. Fultz. *Phys. Rev. Lett.*, 78:366, 1997.

[58] T. A. Stephens, W. Keune, and B. Fultz. *Hyperfine Interact.*, 92:1095, 1994.

[59] W. Sturhahn. *Hyperfine Interact.*, 125:149, 2000.

[60] W. Sturhahn and E. Gerdau. *Phys. Rev. B*, 49:9285, 1994.

[61] M. Tegze and G. Faigel. *Hyperfine Interact.*, 92:1137, 1994.

[62] U. van Bürck, G. V. Smirnov, R. L. Mössbauer, H. J. Marus, and N. A. Semioschkina. *J. Phys. C: Solid State Phys.*, 13:4511, 1980.

[63] U. van Bürck, G. V. Smirnov, R. L. Mössbauer, F. Parak, and N. A. Semioschkina. *J. Phys. C: Solid State Phys.*, 11:2305, 1978.

[64] Mark van Schilfgaarde, I. A. Abrikosov, and B. Johansson. Origin of the invar effect in iron-nickel alloys. *nature*, 400:46, 1999.

[65] R. J. Weiss. *Proc. Phys. Soc.*, 82:281, 1963.